ISTANBUL TECHNICAL UNIVERSITY ★ GRADUATE SCHOOL

ONLINE IMPEDANCE MEASUREMENT OF BATTERIES USING CROSS-CORRELATION TECHNIQUE

Ph.D. THESIS

Taha Nurettin GÜCİN

Department of Electrical Engineering

Electrical Engineering Programme

FEBRUARY 2022

ISTANBUL TECHNICAL UNIVERSITY ★ GRADUATE SCHOOL

ONLINE IMPEDANCE MEASUREMENT OF BATTERIES USING CROSS-CORRELATION TECHNIQUE

Ph.D. THESIS

Taha Nurettin GÜCİN
(504132004)

Department of Electrical Engineering

Electrical Engineering Programme

Thesis Advisor: Asst. Prof. Dr. Levent OVACIK

FEBRUARY 2022

İSTANBUL TEKNİK ÜNİVERSİTESİ ★ LİSANSÜSTÜ EĞİTİM ENSTİTÜSÜ

ÇAPRAZ-KORELASYON TEKNİĞİNİ KULLANARAK ÇEVRİMİÇİ BATARYA EMPEDANSI ÖLÇÜMÜ

DOKTORA TEZİ

Taha Nurettin GÜCİN
(504132004)

Elektrik Mühendisliği Anabilim Dalı

Elektrik Mühendisliği Programı

Tez Danışmanı: Asst. Prof. Dr. Levent OVACIK

ŞUBAT 2022

Taha Nurettin GÜCİN, a Ph.D. student of ITU Graduate School 504132004 successfully defended the thesis entitled "ONLINE IMPEDANCE MEASUREMENT OF BATTERIES USING CROSS-CORRELATION TECHNIQUE", which he prepared after fulfilling the requirements specified in the associated legislations, before the jury whose signatures are below.

Thesis Advisor :	**Asst. Prof. Dr. Levent OVACIK** Istanbul Technical University	....
Jury Members :	**Prof. Dr. Canbolat UÇAK** Yeditepe University	....
	Assoc. Prof. Dr. Murat YILMAZ Istanbul Technical University	....
	Assoc. Prof. Dr. Ömer Cihan KIVANÇ Istanbul Okan University	....
	Asst. Prof. Dr. Burak BARUTÇU Istanbul Technical University	....

Date of Submission : **26 November 2021**
Date of Defense : **2 February 2022**

To my lovely family,

FOREWORD

First of all, I would like to send my deepest gratitude to my supervisor, Dr. Levent OVACIK, who has been always patiently supporting me with his wisdom throughout this long journey. Even at times when I was feeling overwhelmed by the intensity of all the work that had to be done, his patient approach motivated me to keep on going.

I would also like to express my gratitude to Prof.Dr. Altuğ ŞİŞMAN and Dr. Can AKSAKAL for their advices and for giving me the opportunity to use their laboratory. Furthermore, I would like to extend my appreciation to Asst.Prof.Dr. Deniz YILDIRIM for supporting me over the course of this study.

I would also like to express my sincere thanks Res.Asst. Muhammet BİBEROĞLU and Bekir FİNCAN for their support, academic collaboration and most importantly for their heart-warming friendship over long years. I consider myself to be lucky for being surrounded by friends like you.

I would also like to extend my appreciation to my committee members, Prof.Dr. Canbolat UÇAK and Assoc.Prof.Dr. Murat YILMAZ for their valuable inputs and support throughout the study.

I would also like to acknowledge the support of Istanbul Technical University by providing funding under the Scientific Research Programme.

And finally, I would like to express my deepest and most sincere thanks to my dear wife Nuray my lovely daughter Aylin and my sweet parents, who always have been my backbone that kept me motivated.

February 2022

Taha Nurettin GÜCİN
(Electrical Engineer)

TABLE OF CONTENTS

Page

ABBREVIATIONS

AC	: Alternative Current
ADC	: Analog-to-Digital Converter
BIS	: Broadband Impedance Spectroscopy
BMS	: Battery Management System
BN	: Blue Noise
BTS	: Bisquert Short
CCM	: Continuous Conduction Mode
CPE	: Constant Phase Element
IC	: Integrated Circuit
DC	: Direct Current
DCM	: Discontinuous Conduction Mode
DFT	: Discrete Fourier Transform
DUT	: Device Under Test
EIS	: Electrochemical Impedance Spectroscopy
EMC	: Electromagnetic Compatibility
EMI	: Electromagnetic Interference
EV	: Electric Vehicles
FPGA	: Field Programmable Gate Array
FT	: Fourier Transform
HEV	: Hybrid Electric Vehicles
KK	: Kramers-Kronig
LFP	: Lithium-iron-phospate
LTI	: Linear Time Invariant
MLCC	: Multi Layer Ceramic Capacitor
MMC	: Multilevel Converter
NiMH	: Nickel-metal-hydrate
NMC	: Nickel-manganese-cobalt oxide
OCV	: Open Circuit Voltage
PRBS	: Pseudo Random Binary Signal
PSD	: Power Spectral Density
PWM	: Pulse Width Modulation
RES	: Renewable Energy Sources
RN	: Red Noise
SLA	: Sealed Lead-acid
SOC	: State of Charge
SOH	: State of Health
VHDL	: Very High Speed Integrated Circuit Hardware Description Language
WN	: White Noise

SYMBOLS

x[n]	: Input Sequence
y[n]	: Output Sequence
h[n]	: System Impulse Response
FT[]	: Fourier Transform
X[k]	: Discrete Fourier Transform of Input Sequence
Y[k]	: Discrete Fourier Transform of Output Sequence
H[k]	: Discrete Fourier Transform of System Impulse Response
σ_x	: Standard Deviation of Input Sequence
σ_y	: Standard Deviation of Output Sequence
e_m^2	: Sum of Squares of Differences Between Input & Output Signals
$r_{xy}(m)$	: Normalized Cross-Correlation of Input & Output Signals
$r_{xy}(\tau)$	: Normalized Cross-Correlation of Continuous Input & Output Signals
$R_{xy}(k)$	: DFT of Normalized Cross-Correlation of Continuous Signals
$R_{xy}(f)$	: FT of Normalized Cross-Correlation of Continuous Signals
$r_{xx}(m)$	: Normalized Auto-Correlation of Input Signal
$r_{xx}(\tau)$	: Normalized Auto-Correlation of Input Signal
$R_{xx}(k)$	: DFT of Normalized Auto-Correlation of Input Signal
$R_{xx}(f)$	: FT of Normalized Auto-Correlation of Input Signal
$w_{xy}(m)$	: Cross-Correlation (Not Normalized) of Input & Output Signals
$w_{xx}(m)$	: Auto-Correlation (Not Normalized) of Input Signal
$W_{xy}(f)$	: FT of Cross-Correlation (Not Normalized) of Input & Output Signals
$W_{xx}(f)$	: FT of Auto-Correlation (Not Normalized) of Input Signal
$G_{vd}(s)$	: Control to Output Voltage Transfer Function of Converter
$G_{id}(s)$	: Control to Output Current Transfer Function of Converter
W_{xv}	: FT of Cross-Correlation of Control Input & Output Voltage Signals
W_{xi}	: FT of Cross-Correlation of Control Input & Output Current Signals
$D_{cnt}]$	: Steady State Duty Cycle
$\hat{d}_{per}$	: Perturbation Signal on Duty Cycle
$I_{out}]$	: Steady State Output Current
$\hat{i}_{out}$	: Perturbation Based Output Current
$\hat{v}_{out}$	: Perturbation Based Output Voltage
N	: Data Length of Perturbation Signal
Z[f]	: Impedance
f_s	: Sampling Frequency
f_{sw}	: Switching Frequency
f_{start}	: Lower Limit of Obtained Frequency Spectrum
f_{stop}	: Upper Limit of Obtained Frequency Spectrum
Δf	: Resolution of Obtained Frequency Spectrum
T_{test}	: Testing Time
f_{co}	: Cut-off Frequency of Moving Average Filter
MA_L	: Moving Average with a Window Size of L
MA_0	: Zero Lag Moving Average

Z_{BTS}	**:** Impedance of Bisquert Short Element
Z_{CPE}	**:** Impedance of Constant Phase Element
L_{BTS}	**:** Depth of the Pore within a Porous Electrode
χ	**:** Impedance of the Electrolyte within the Pore
ζ	**:** Impedance at the Active Interface Region on the Surface of the Electrode

LIST OF TABLES

Page

LIST OF FIGURES

Page

ONLINE IMPEDANCE MEASUREMENT OF BATTERIES USING CROSS-CORRELATION TECHNIQUE

SUMMARY

Although the foundation of battery technologies had been laid out quite a long time ago, the recent increase of the interest for technologies such as renewable energies, portable devices, electric vehicles urged the battery technology to emerge as a major research topic.

Moreover, for such applications, the batteries generally considered to be one of, if not the most crucial component of the system. This can be attributed to the fact that the energy stored within the batteries ensures the continuity of system operations. Additionally, the lifetime of such systems is generally directly correlated with the lifetime of batteries utilized thereof.

Consequently, the assessment of battery condition is a crucial aspect for the durability and stability of a very wide range of applications. However, as most of the parameters regarding the status of the batteries are not directly measurable, the battery status generally has to be estimated. This task is generally undertaken by a battery management system (BMS), which often runs some tests on the battery to predict certain parameters such as state of health (SOH) and state of charge (SOC).

Electrochemical Impedance Spectroscopy (EIS) principally presents the complex impedance values of a battery over a frequency range of interest and it is widely accepted as the most advanced testing technique for batteries as it allows a foundation for the estimation of various battery parameters such as battery temperature, SOC and SOH. However, very often, these measurements have to be accompanied with advanced estimation algorithms for ensuring reliable and accurate estimation of parameters.

This thesis aims to provide a practical implementation of EIS measurements. For this purpose, the study presented in this thesis implements the suggested method into the DC-DC converters, which are almost always present in the systems deploying batteries. The implemented method is based on cross-correlation calculations.

In the first part of the thesis the motivation and the objectives of the study is elaborated and a literature overview of the state of the art is provided for representing the current approaches and for emphasizing the need for improvements.

The first part is followed by a theoretical background section, where the principles of the cross-correlation calculations and it's adaptation to battery EIS measurements are explained in detail. Several improvements for the method, especially aimed for battery applications, are also provided.

In the subsequent part, the theoretical findings are supported by simulations, which are created in MATLAB by using the Simulink graphical programming environment.

In this part, the theory is preliminarily tested by simulations regarding impedance measurements of a passive RLC circuit.

In the latter part, a test bench is designed for performing experiments to serve as proof of concept for the suggested approach. The test bench comprises a digitally controlled boost converter that is configured for charging a 12-V, 7-Ah sealed lead-acid (SLA) battery. The boost converter is controlled by an FPGA based platform, namely the Nexsys 4 DDR of Xilinx. The digital controller also comprises subprogram for injecting the necessary signals to the battery. The waveforms that occur during the tests are then recorded by a data acquisition system based on NI cDAQ platform so that the saved data can be processed in MATLAB environment for calculating the EIS diagrams.

During the experiments, firstly, the battery is tested via the proposed method at 50% SOC. It is shown that the results of the present approach coincide with those obtained by a commercially-available, laboratory-type, high-precision instrument. Finally, the tests were also repeated for 25% and 75% SOC values. Additionally, further results are also presented to prove the validity of the approach even when the DC-DC converter is configured to provide a constant current under closed feedback loop. In conclusion, it is shown that the proposed approach can be reliably used to analyse the impedance of batteries over a wide frequency range during battery charging process.

ÇAPRAZ-KORELASYON TEKNİĞİNİ KULLANARAK ÇEVRİMİÇİ BATARYA EMPEDANSI ÖLÇÜMÜ

ÖZET

Batarya teknolojilerinin temelleri uzun yıllar atılmış olsa da, yakın tarihte yenilenebilir enerji teknolojileri, taşınabilir cihazlar ve elektrikli araçlar ve benzeri alanlara olan ilginin büyük bir ivme ile artması, batarya teknolojilerinin günümüzde ana akım araştırma alanlarından biri olarak gündeme gelmesine neden olmuştur.

Yukarıda bahsedilmiş olan uygulama alanları kapsamında bakıldığında, sisteme sağlanan elektrik enerjisinin genellikle temel kaynağı olan bataryalar, içerisinde bulunduğu sistemin en önemli bileşenlerinden biri olarak düşünülmektedir. Buna ek olarak, bu gibi sistemlerin ömrü genelde içerisinde kullanılmış olan bataryanın ömrü ile direkt bir ilişki içerisindedir.

Yukarıda verişmiş olan nedenlerden ötürü batarya ile ilgili ölçümler, hem bataryanın hem de bataryanın içerisinde bulunduğu sistemin sağlığı ve devamlılığının ön görülebilmesi açısından büyük önem arz etmektedir. Ne var ki, bataryaların durumu ile bağıntılı olan değişkenlerin çoğu maalesef doğrudan ölçülebilir büyüklükler değillerdir. Bu nedenden dolayı, bataryanın durum bilgileri genellikle yapılan ölçümler üzerinden kestirim yapmak vasıtası ile elde edilmektedirler.

Batarya durum kestirim işlemleri genellikle sistem içerisinde bulunan bir batarya yönetim sistemi tarafından üstlenilmektedir. Batarya yönetim sistemleri batarya üzerinde çeşitli testler yapmak vasıtasıyla bataryanın şarj durumu, sağlık durumu ve benzeri değerlerin kestirimi amacı ile kullanılabilecek bazı değişkenleri ölçmeye çalışırlar.

Bu gibi testlerden biri olan Elektrokimyasal Empedans Spektroskopisi, ilgilenilen bir frekans aralığı boyunca, bataryanın karmaşık empedans değerinin elde edildiği bir ölçüm yöntemidir. Elektrokimyasal Empedans Spektroskopisi genel anlamda bir batarya üzerinde uygulanabilecek olan en kapsamlı test olarak kabul edilmektedir. Bu bağlamda yapılan ölçümler batarya durumu kestirimi için kullanılacak olan bir temeli teşkil etmektedirler. Fakat, elektrokimyasal sistemlerin karmaşıklığı nedeni ile, batarya durum kestirimlerinin güvenilir ve hassas bir şekilde gerçekleştirilebilmesi için Elektrokimyasal Empedans Spektroskopisi Ölçümlerinin gelişmiş kestirim algoritmaları tarafından yorumlanması gerekmektedir.

Bu tez kapsamından sürdürülen çalışmalar ile Elektrokimyasal Empedans Spektroskopisinin batarya uygulamalarına elverişli bir yöntem olarak önerilmesi amaçlanmıştır. Bu bağlamda, Elektrokimyasal Empedans Spektroskopisi ölçümlerinin, içerisinde batarya bulunan sistemlerde büyük oranda kullanılmakta olan DC-DC dönüştürücülere entegre edilmesi hedeflenmiştir. Böylelikle, tez kapsamında önerilen bu yöntemin, sistem yapısı açısından büyük değişiklikler yapılmasına gerek olmadan, hali hazırdaki sistemlere kolayca entegre edilebilir bir yaklaşım olarak literatüre

katılması amaçlanmıştır. Önerilen bu yöntem literatürde bilinen çapraz-korelasyon hesaplarının temellerine dayanmaktadır.

Çapraz korelasyon hesaplarının sistem transfer fonksiyonlarının tespit edilmesi amacı ile kullanılması fikri temel sinyal işleme kitaplarında ele alınmıştır. Hatta, yakın zamanda yapılan bazı çalışmalar, bu yöntemin DC-DC çeviricilerin transfer fonksiyonlarının bulunması amacı ile kullanılabileceğini ortaya koymuştur. Fakat, bu tezin çalışma konusunun önerildiği tarihte bu yöntemi batarya empedans ölçümlerinin çevrimiçi tespiti amacı ile kullanımına dair bir çalışmaya rastlanmamıştır. Bu tez kapsamında, çapraz-korelasyon tekniği batarya uygulamaları kapsamında iyileştirilerek kolay uygulanabilen ve yüksek doğrulukta bir batarya empedans ölçümü yaklaşımı ortaya koyulmuştur.

Tezin ilk kısmında, tezin motivasyonları ve hedefleri açıklanmış ve tezin konusu ile alakalı bir literatür özeti sunulmuştur. Literatür özeti kapsamında, hem batarya empedans ölçümlerinin önemini vurgulayan çalışmalara yer verilmiş olup hem de DC-DC çeviriciler vasıtası ile bataryarların empedans ölçümlerini çevrimiçi olarak yapmayı hedefleyen yakın tarihli çalışmalar okuyucunun dikkatine sunulmuştur. Bu şekilde derlenmiş olan literatür özeti tez konusunun hem önemine hem de güncelliğine ışık tutmaktadır.

Takip eden bölümde ise tezde sunulan yaklaşımın temelini teşkil eden çapraz-korelasyon yönteminin temellerine ve bu yöntemin empedans ölçümleri için kullanımına dair teorik bilgiler detaylı bir biçimde verilmiştir. Bunlara ek olarak, tez kapsamında önerilen yöntemin batarya uygulamarında kullanımının iyileştirilmeini hedefleyen önerilere de aynı bölüm içerisinde yer verilmiştir.

Bir sonraki bölümde, teorik kısımda işlenmiş olan yaklaşımlar simulasyon çalışmaları ile desteklenmiştir. Bu kapsamda Matlab - Simulink yazılımında pasif bir RLC devresinin karmaşık empedans değerlerini geniş bir frekans aralığında ölçümü amacı ile bir dc-dc çevirici simüle edilmiş olup, bu çeviricinin kontrol kısmına çapraz-korelasyon tekniğine dayalı olan empedans ölçüm algoritması entegre edilmiştir. Bu simülasyon devresinin gerçek dünyadaki uygulamasına yakın olması için ölçüm sisteminde meydana gelebilecek bazı hatalar da simülasyon kapsamında hesaba katılmıştır. Sonuç olarak, RLC devresi üzerinde yapılan simülasyonların RLC devresinin analitik olarak hesaplanmış empedans değerlerine çok yakın sonuçlar verdiği gözlemlenmiştir.

Takip eden bölümde ise testlerin gerçekleştirilmesi için gereken bir test ortamınının nasıl tasarlandığı gösterilmiştir. Tasarlanan test ortamı 7 Ah - 12 Volt bir kurşun-asit bataryayı (Yuasa NP7-12) sarj etmek için programlanmış, dijital olarak kontrol edilen bir boost dönüştürücü devresi içermektedir. Boost dönüştürücü bir Xilinx firmasının Nexsys 4 DDR isimli bir FPGA platformu tarafından kontrol edilmektedirç Bu FPGA platformu Elektrokimyasal Empedans Spektroskopisi ölçümleri amacı ile bataryaya zerk edilecek olan sinyalleri uygulayan bir alt programı da içermektedir. Bu sinyallerin uygulanması sonucu bataryada oluşacak olan dalga formları ise NI firmasının cDaQ platformu temeline dayanan bir veri toplama sistemi tarafından kayıt altına alınmaktadır. Kayıt edilen veriler ise MATLAB ortamında işlenilerek empedans ölçümleri elde edilmektedir.

Yapılan deneyler kapsamında, ilk olarak bir önceki bölümde simulasyonlar ile ölçümü yapılmış olan RLC devresi bu sefer deneysel olarak test edilmiştir. Bu testlerin sonuçları IET Labs firmasının yüksek hassaslıktaki IET-1920 laboratuar tipi empedans ölçüm cihazı ile referans teşkil etmesi amacıyla alınan ölçümler ile karşılaştırılmıştır. Bu karşılaştırma sonucunda gözlemlenen yüksek uyum neticesinde, önerilen yöntemin pasif yükler üzerinde başarılı bir biçimde çalıştığı sonucu çıkarılmıştır. Yapılan bu ilk deney kapsamında elde edilen sonuçlar bir akademik konferans çalışması olarak yayınlanmıştır.

Pasif yük üzerindeki başırılı ölçümler neticesinde batarya üzerinde yapılacak testlere başlanmıştır. Bu bağlamda, öncelikle bataryaya yapılacak olan perturbasyonun değerinin nasıl belirleneceği deneysel olarak gösterilmiştir. Çeşitli genliklerde yapılan perturbasyonların sonuçları empedans ölçümlerinin tutarlılığına bir ölçek olarak kullanılan Kramers-Kronig yöntemi ile yorumlanmıştır.

Batarya deneyleri üzerinde yapılan deneyler kapsamında ilk olarak tez kapsamında önerilen yöntemin doğruluğunu onaylaması açısından bir referans ölçüm alınmasına karar verilmiştir. Bu referans ölçümler için piyasada bulunan yüksek hassaslıktaki bir empedans spektroskopisi cihazı (Gamry Reference 3000) kullanılmıştır. Bu bağlamda referans ölçümler için kullanılan batarya EN 50342-1 CENELEC standartlarına uyularak % 50 doluluk oranına getirilerek ölçümler alınmıştır. Sonrasında, aynı doluluk oranındaki batarya tez kapsamında önerilen yöntem ile test edilerek alınan ölçümler söz konusu referans ölçümler ile karşılaştırılmıştır. Bunun neticesinde, çapraz-korelasyon tekniğine dayanan ölçümlerin referans ölçümler ile yüksek oranda uyuştuğu gösterilerek, tez kapsamında önerilen bu çapraz-korelasyon tekniğine dayalı tekniğin geçerliliği ispatlanmıştır.

% 50 şarj durumunda yapılan ölçümlere mütakip olarak % 25 ve % 75 sarj durumları için deneyler tekrar edilmiştir. Sonuç olarak, bu tez kapsamında önerilen yöntemin güvenilir bir biçimde batarya empedans ölçümleri için kullanılabileceği gösterilmiştir. Ek olarak, önerilen yöntemin DC-DC çeviricinin kapalı çevrim olarak çalıştığı durumlarda da geçerli olduğunu gösteren ölçümler de bu bölüm kapsamında sunulmuştur.

Elde edilen sonuçlar hem Bode Diyagramları hem de Nyquist Diyagramları şeklinde sunulmuştur. Son olarak, farklı şarj durumları için elde edilen sonuçlar tek bir grafik üzerinde karşılaştırılarak diyagramda gözlemlenen değişikliklerin literatürde benzer bataryalar için yayınlanan sonuçlar ile benzer olduğu gösterilmiştir. Ek olarak, ölçümler literatürde yakın zamanda yayınlanmış olan bir elektrik eş değer devre modeline uygulanarak, bu modeldeki temsili elemanların büyüklükleri için çıkarım yapılmıştır.

1. INTRODUCTION

1.1 Motivation

In recent years, the increase of interest in environment friendly and efficiency oriented technologies has urged the researchers to examine the battery technology extensively. Technologies such as renewable energy sources (RES), electric vehicles (EVs), hybrid electric vehicles (HEVs) may be considered as the main driving force behind this recent push in the battery technology. Additionally, the recent popularity of portable devices, which have been deeply penetrated into the market now, has further contributed to the tendency towards the interest in the battery technologies.

Batteries can be comprised of various chemical substances such as nickel metal hydride, lithium-ion, nickel cadmium and lead acid. The chemistry preference depends on the performance demands and costs concerning the application. Users generally expect short charging durations, long life cycle, long operating times and low costs from these devices. Additionally, the issues related with battery technology and infrastructure, such as the energy density influencing the range of EVs, are generally the limiting factors on applications and commercialization of these technologies. Thus, high-precision estimation techniques for battery-specific parameters are of major importance for eliminating these factors.

Energy systems employing battery capabilities contain battery cells in series-parallel combinations in order to supply electrical power at a desired level. The complexity of battery cell network may require various monitoring and controlling techniques to maintain the health, reliability and efficient operation of the battery. All these necessities can be provided by a suitably designed battery management system (BMS).

One of the major tasks of the BMS is to provide an accurate information on the state of charge (SOC) of the battery that is the measure of available charge left in the battery for further operation. However, it is not a quantity that is available for direct measurement. Depending on the application, accurate estimation of this value might be of crucial importance since it provides protection by avoiding overcharging and deep discharging to ensure the health of the battery. It also ensures the abilities for dynamic power management, charging and discharging control.

One other important task of the BMS is to predict and to monitor the state of health (SOH) of the battery. Although there are various SOH definitions, it is briefly the measure of remaining energy storage capacity of a used battery compared to a new one. Depending on the application and requirements the evaluation of SOH may vary.

Batteries are electrochemical devices with highly complex nature. Since these devices are employed in electrical systems, expressing their complex nature from electrical engineering point of view is crucial. Accurate state estimation of batteries enables making right decisions concerning the power management of the battery and this helps keeping the battery and consequently the system in good condition.

There are various methods adapted for testing the state of the batteries, where certain methods may be battery specific. The electrochemical impedance spectroscopy (EIS) is generally accepted as the most advanced method that could be applied for diagnosing a battery. EIS is the process of obtaining complex valued impedance diagrams of electrochemical devices, such as the batteries, over a frequency range of interest.

The EIS is generally accompanied by a parameter extraction stage, where the results are fit to a electrical battery model in order to find the values of the model, where these values are then associated to the battery state information. There are various studies on the modelling of the batteries by using equivalent electrical circuits. By many researchers it has been proven that the equivalent circuit elements of the batteries change with varying battery states, such as SOC, SOH, temperature etc., and that certain parameters derived from the electrical battery models may be directly or indirectly related to these states.

However, it should be also noted that the EIS results are generally quite complex and it requires extensive testing in advance as to be able to perform good associations between battery states and the electrical battery model parameters. Furthermore, conventionally the devices capable of performing EIS require the battery to be disconnected from the system and tested separately.

1.2 Research Objective

For the reasons given above, one objective of the thesis is to provide a method that is capable of performing reliable online EIS tests without the need for disconnecting the battery system to be tested from the power system. Therefore, it is intended to propose a testing method that can be performed even without needing to disconnect the control loops that are governing the power system. This would enable the battery to keep performing it's provisioned tasks within the system so that the overall system reliability would be improved.

However, one challenge with online EIS applications is that the state of the battery, such as the SOC value, may change during the testing period, since the estimation process is performed in course of the normal system operation. Abrupt changes of system sates may cause significant variations in battery parameters and may influence the testing process. Thus, the testing time for EIS should be kept as short as possible.

Furthermore, it is intended to implement the EIS method into the DC-DC converter that is regulating the battery, considering that almost all power systems comprising a battery would also comprise a DC-DC converter.

Traditionally, the devices that are capable of EIS measurements, besides not being able to be implemented in the power system, are quite expensive and therefore their use is generally limited to the laboratory use. Thus, another objective of the thesis is to offer a method that could be implemented into the existing DC-DC converters so that the proposed method should be reasonable in terms of costs and applicability. More specifically, this thesis aims to implement EIS method into the digitally controlled DC-DC converters.

A further objective of the thesis is to provide a method that can reliably operate considering the nature of digital DC-DC converters, which may rise issues, such as noise caused by switching or noise caused by quantization process due to analog-to-digital conversion of measurement devices. In this thesis, it is planned to overcome these challenges by using signal processing techniques.

Finally, given the complexity of the batteries, many testing methods and other prognostic tools generally are specific for a battery type [2]. However, this thesis intends to provide a method that is applicable for various battery types, as it is already known that EIS can be performed for many battery types. It is pointed out that extensive testing in advance and prior information on the battery is necessary to perform logical state estimation procedures based on EIS.

1.3 State of the Art

1.3.1 EIS applications

There are various studies focusing on the analysis of battery complex impedances. The earliest trials for battery impedance measurements are reported to be conducted in 1941 by E. Willihnganz, where an electrochemical battery cell was excited with a 5 mV amplitude AC signal [3]. Such tests allow the scientists to evaluate and extract some critical information concerning the battery dynamics and kinetics. Usually different set of information can be obtained by measurements at various frequencies. The process of obtaining the complex impedance for batteries are sometimes called the Electrochemical Impedance Spectroscopy.

The measurements are performed in either galvanostatic or potentiostatic mode. While the galvanostatic mode represents the case where a certain current is injected to the battery as the voltage is observed, vice versa, in the potentiostatic mode a certain voltage is injected to the battery and the current is observed. The galvanostatic mode is usually preferred due to very low resistance values of the battery packs, so that the current is limited in this measurement mode.

An electrochemical cell may be modelled by using electrical equivalent circuits for mimicking their electrical qualities. These circuits generally comprise some resistive, inductive and capacitive components, wherein the resistive components are generally representative of the electrodes, current-collectors, electrolytes and transfer reactions of electrons. On the other hand, the capacitive components are representative of double-layer capacitance. Finally, the inductive components are utilized for modelling the reactions due to porous nature of electrodes. Consequently, the total impedance of such a cell comprises resistive and reactive components [3], as shown in Fig. 1.1. The first circuit represents both positive and negative electrodes separately. In the second circuit the components of both electrodes are united. The last circuit can be used to express the battery impedance at lower frequencies, where the effect of the inductance diminishes. The component denoted by "W" is Warburg Impedance.

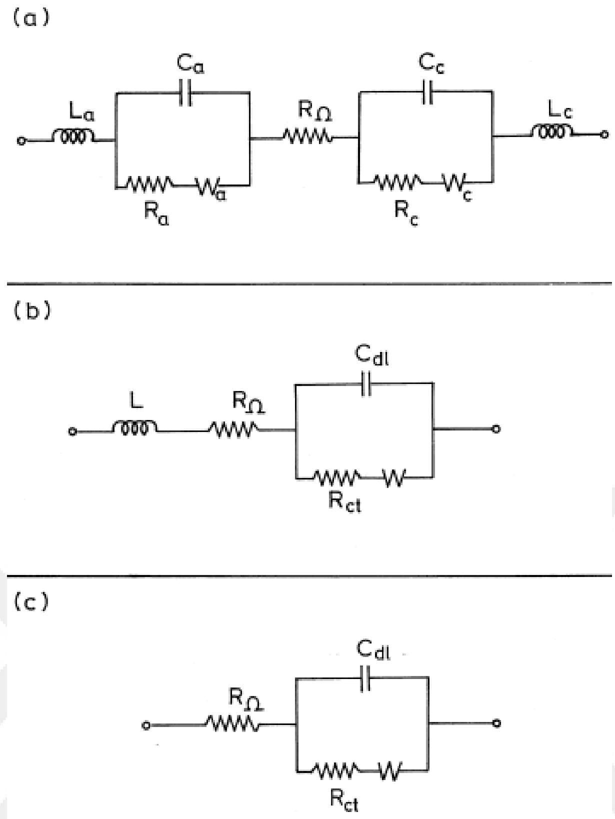

Figure 1.1 : Lead Acid Battery equivalent circuit model [3].

A sample Nyquist Diagram of a lead-acid battery [4] is given in Fig. 1.2. As it can be seen, the diagram consists of a vertical line at the beginning, followed by two semicircles. Corresponding frequency values are expressed in the figure. As it can be seen, in high frequency region, the inductance is dominant. The first semicircle usually corresponds to a frequency range of several hundred Hz to 10^{-1} Hz. The second semicircle occurs in very low frequency region, which is between μHz and mHz.

The Warburg Impedance, which corresponds to the second semicircle at Fig. 1.2, occurs due to diffusion mechanism in the battery and it is dominant in very low frequency region. This low-frequency-dominant impedance can be one of three types [5], shown in Fig. 1.3.

Fig. 1.4 illustrates a Nyquist Diagram of a Li-ion battery pack and equivalent battery model. It also shows the relationship between the model and the Nyquist Diagram.

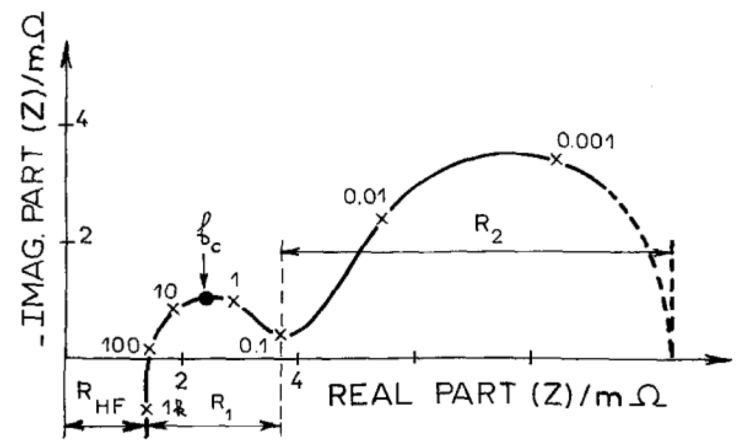

Figure 1.2 : Nyquist diagram of the impedance of a lead-acid battery [4].

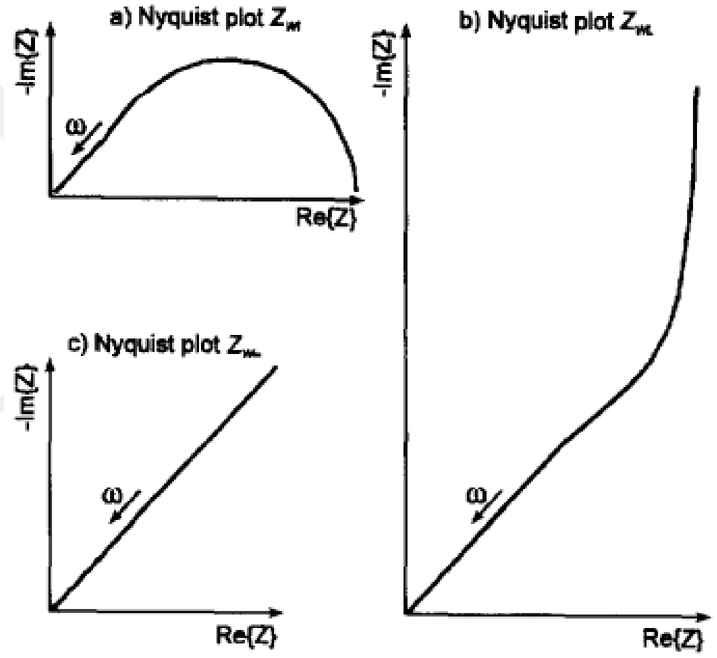

Figure 1.3 : Three different types of Warburg Impedance [5].

In the recent literature, there are numerous studies reporting that essential information, such as the state of charge (SOC), the state of heath (SOH) and even internal temperature of various type of batteries can be estimated by careful interpretation of these diagrams. These studies investigate the complex impedance of the batteries generally try to correlate a parameter of the battery model derived by EIS measurements to the states tha are desired to be estimated. Generally, either change in the Nyquist Diagrams of battery impedance, or a variation in single parameter are attempted to be correlated to SOC.

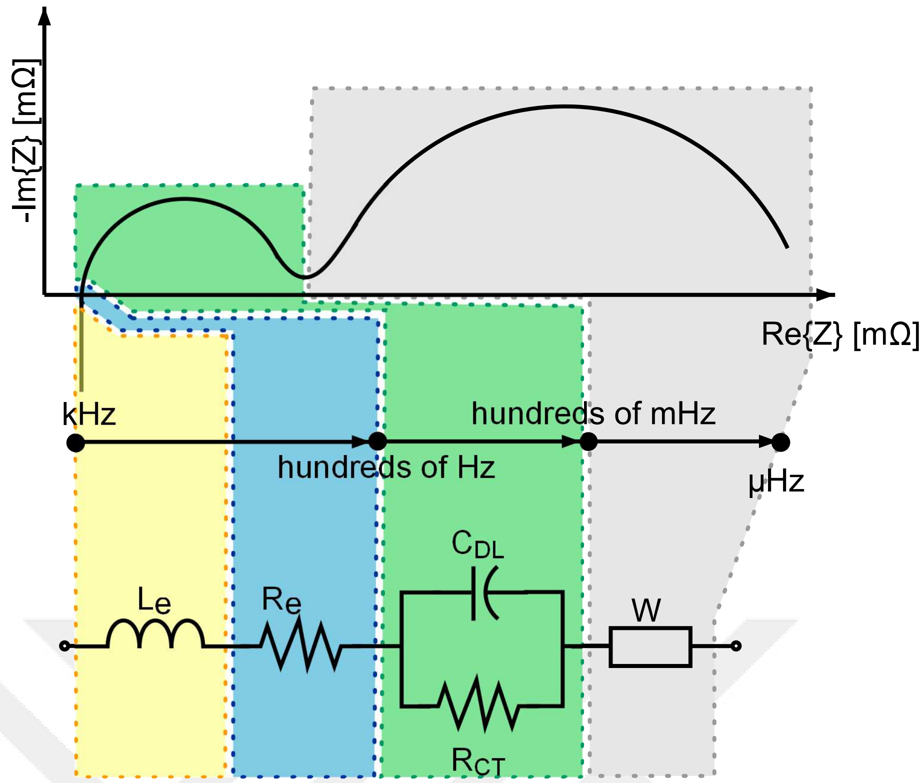

Figure 1.4 : The relationship of the battery equivalent circuit and the Nyquist diagrams for a Li-ion battery.

In one of the earlier studies [5] EIS measurements are utilized for deriving a battery model based on Randle's theory for a lead-acid battery. The EIS measurements are performed with superimposed DC bias. The validity of the derived model is then proven by comparing the experimental voltage waveforms with simulation results on the derived model. Hereby, it is shown that EIS is a powerful tool for modelling the battery behaviour.

In another earlier study [4] it is shown that impedance of lead-acid and nickel-cadmium batteries are highly dependent on SOC and SOH values. It is also pointed out that the temperature is also another factor affecting the impedance of these batteries. The tests in high frequency exhibited correlation with SOC, while tests in low frequency region revealed better correlated parameters. However, the low frequency region is found to be highly dependent on the temperature, so that these tests are recommended to be in a controlled environment. Otherwise, the study suggested to use relatively higher frequencies (between 10 Hz and 100 Hz) for SOC and SOH testing in uncontrolled temperature environments. Impedance diagram of a Lead-Acid battery for various

SOC values is shown in Fig. 1.5. As it can be seen SOC completely affects the complex impedance of the battery.

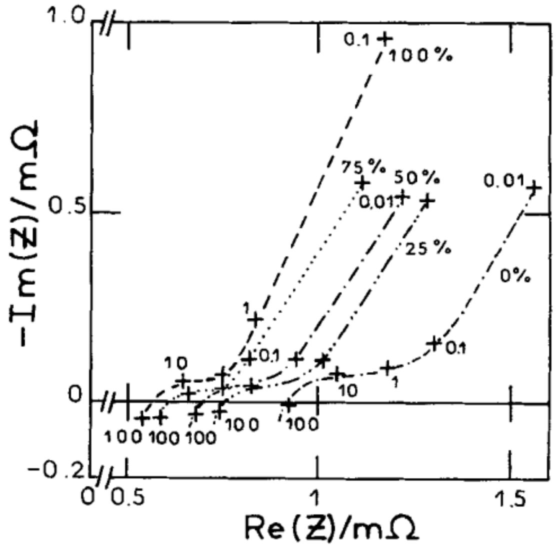

Figure 1.5 : Impedance diagrams of 2 V, 390 Ah lead-acid battery at various SOC values [4].

Later, another study [3] elaborated the use of EIS measurements further with respect to SOC estimation of several types of batteries, namely the lead-acid, nickel-cadmium nickel-metal hydride and lithium batteries. The battery model used in their study is illustrated in Fig. 1.1. Throughout the study, they demonstrated that different parameters of the battery model can be related to SOC for various battery types. Finally, they concluded that , although impedance parameters and their relation to SOC variation is not unique for each battery system, EIS measurements are useful for SOC estimation of the batteries. Fig. 1.6 illustrates the changing behavior of complex impedance of a Li-ion battery for varying SOC values. However it should be noted that, both studies [4], [3] referred to some controversial studies claiming that it was hard to find some clear and environment-insensitive correlation between SOC and any impedance parameter.

In a following study, [6], an attempt to correlate SOC variation to different parameters of the battery models derived by EIS measurements is demonstrated. For various parameters, the study came to the conclusion that no clear cut dependency of SOC and a battery model parameter can be found, with the exception of the series resonance frequency, $f_{\pm}$, which is defined as the frequency where the impedance of the battery is purely resistive.

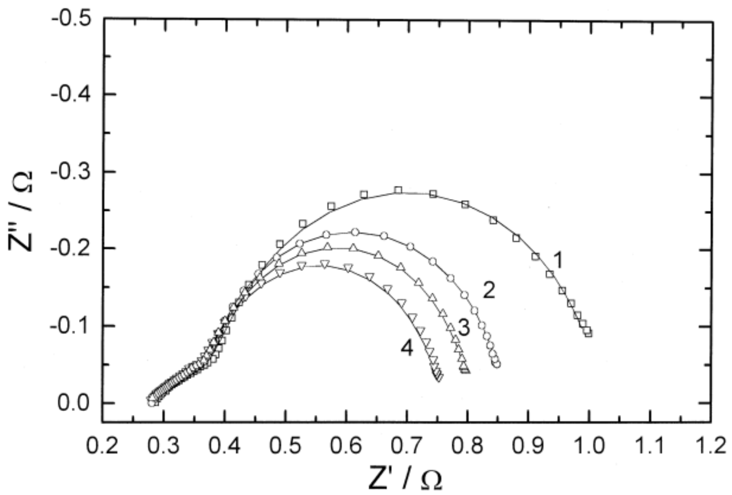

Figure 1.6 : Impedance spectra of lithium-ion battery at SoC = 0 (1) , 0.14 (2) , 0.28 (3) , 0.42 (4) as frequency swept between 25 mHz and 100 kHz [3].

Later on, the same research group demonstrated the further uses of the EIS measurements for diagnosing the batteries [7]. They concluded that that EIS measurement is a powerful tool which can be used for estimation of various battery states such as dynamic modelling, cranking capability, SOC and ageing affects. They also determine the series resonance frequency, $f_{\pm}$, to be a good indicator for SOC. The relationship of $f_{\pm}$ and SOC is shown in Fig. 1.7. Though, they also pointed out that interpretation of EIS results needs comprehensive testing to achieve reliable results. For this reason, they suggest to combine the impedance spectroscopy method with other methods, such as self-learning algorithms, since the $f_{\pm}$ test is also dependent on the temperature.

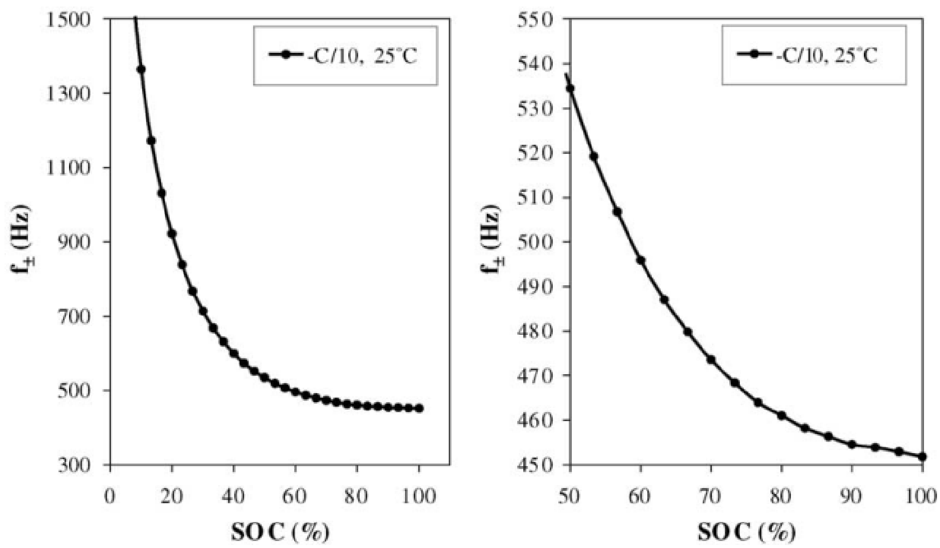

Figure 1.7 : Relationship of $f_{\pm}$ and SOC for a Lead-Acid battery [7].

In [8] Lithium-ion batteries are interpreted in relationship with the EIS measurements. Similar to previous studies, this study also confirmed that SOC estimation can be performed by EIS measurements with the expense of conducting comprehensive tests in advance for gaining substantial knowledge about the battery that is intended to be diagnosed.

As the lithium-ion batteries gained popularity, there has been numerous studies evaluating the possibilities offered by EIS measurements. In such as study in [9], the possibility of online EIS measurements for lithium-ion batteries are investigated. The study compares the EIS results of static, meaning that the battery was rested before EIS testing, and active batteries, implying the lack of a resting period, are compared. It is then concluded that EIS can be used for both active and static batteries as a mean for SOC estimation for lithium-ion batteries.

In a more recent study, [1], the relationship of EIS measurements with SOC and temperature of lithium-ion batteries under various conditions, such as charging/discharging rate and various aging states, are presented for a commercial battery. They revealed that there was a correlation between the parameter SOC and r_d, which was defined as The real part of the battery impedance at the point where the negative imaginary part has its local minimum. This relationship depending on the battery age and SOC was exhibited in Fig. 1.8.

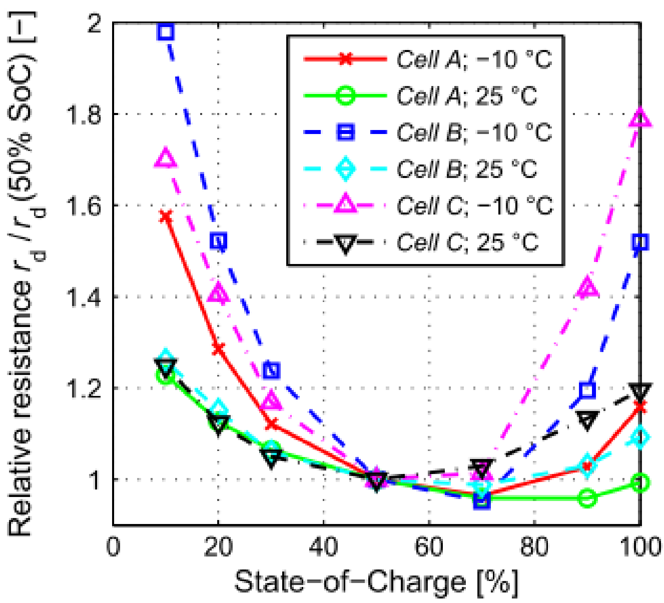

Figure 1.8 : Dependency of the resistance r d on the SoC (relative to its value at 50% SoC) for Cell A (aged by 200 cycles), Cell B and Cell C (aged by 1900 cycles) [1].

In [10], the researches were able to derive linear relationship between the SOC and some extracted battery parameters via EIS measurements. They also interpreted the aging effects and demonstrated that the linear relationship is not distorted by the aging effects. They concluded that EIS is suitable for SOH measurements.

A later study, [11], also demonstrated that internal temperature measurements can also done reliably by online EIS measurements.

Finally, the paper [12] presents how online EIS measurements can be utilized for battery status monitoring. Using the obtained EIS results and extreme learning machine (ELM), they present how SOC of batteries during constant current and constant voltage charging operation can be measured [12].

Briefly summarizing, the literature demonstrates that EIS measurements are the most powerful technique for diagnosing various types of batteries. Though, the interpretation of the results are not always straightforward and most of the time it needs a comprehensive testing of the specific battery to be diagnosed in advance, so that certain parameters of the battery can be related to specific state values of the battery that are desired to be estimated. It is consistently shown that, once a clear relationship between a certain parameter and a state value is established, these tests can be reliably used for the diagnosis of the battery.

1.3.2 DC-DC converter system identification

As explained in the previous chapters, one aim of this thesis is to implement the EIS measurement capabilities into the digitally controlled DC-DC converters. This objective will be achieved based on system identification techniques directed to the identification of DC-DC converter systems. The underlying principles of these techniques are elaborated in the following chapter. For this reason, the literature on the topic of DC-DC converter system identification is examined here.

One of the earlier studies directed to identify the power converters, [13], proposes the cross-correlation method for identifying the transfer functions of the power converters, which is intended to be used for automatic tuning of their control loops. The study discusses the practical aspects for implementing the cross-correlation based calculations into the digital controller of the power converters.

Soon after, the same study group published a more detailed study [14], where some requirements with respect to the system identifaction of DC-DC converters are discussed. This study identifies some key requirements such as continuation of system operation, immunity to switching and quantization noises and a low level need of processing requirements. For this purpose, the cross-correlation based analysis method is suggested again. Furthermore, the basic principles of the technique are given and a practical example is presented, wherein a pseudo random binary signal (PRBS) is injected to the duty cycle command of an digitally controlled forward converter. Some key features of the applied PRBS signal is discussed and a good correlation of the results with analytical models is illustrated.

Later on, the cross-correlation based system identification techniques are demonstrated for a buck converter, where loop gain of the converter is derived under closed loop control [15]. The study also discusses the applicability of the method into a field-programmable gate array (FPGA).

In a later study, [16], the design of the injection signal that is used for converter identification purposes is discussed in detail. The study presents design techniques for the injection signal with respect tosome key characteristics, such as duration of the signal, bandwidth, resolution and time-aliasing.

In another study, [17], some improvements for improving the identification accuracy is proposed. These improvements are the delaying of output voltage sampling, windowing the measured cross-correlation and correction of non-ideal input spectrum. The improvements are proven by both simulation and experimental results of a digital buck converter.

Another interesting study, [18], demonstrates that some known techniques from audio engineering may be adapted for improving the accuracy of cross-correlation based converter identification techniques. The study eloborates the improvements achieved by pre-emphasis/de-emphasis stages for correcting the signal-to-noise ratio of the injected signal, smoothing techniques for measured results and selection of PRBS magnitude. Experimental results are presented for DCM and CCM modes of converters.

A futher study in the same domain, [19], discusses the identification of open-loop and closed-loop transfer functions of the converter based on cross-correlation method. Furthermore, it is demonstrated that the transfer function of the compensator can also be derived.

A more recent study, [20], addresses the importance of the proper selection of perturbation signal and proposes an automated technique for selecting a suitable duty cycle perturbation amplitude in order to minimize the additional efforts for pre-processing of the perturbation signals.

As seen from the above literature overview, there are various studies aimed at identifying converter transfer functions based on the cross-correlation method. This method was found to be quite powerful for the analysis of the converter. Generally, these studies are directed to automated compensator tuning of the power converters. Various techniques have been suggested for improving the identification accuracy.

1.3.3 Online EIS applications

While interpreting the EIS measurements, it has been found out that most of the valuable information about the characteristics of batteries generally reside in the low-frequency region. Depending on the battery type, the frequency of range of interest generally resides in between a few mHz to a few hundred Hz. Furthermore, since the impedance values at low-frequency region are generally in a few milliohm values, very accurate measurements are needed.

There are commercially available EIS devices on the market that are capable of providing very accurate measurements ranging from μHz to MHz frequency range. However, these devices are generally very expensive. For example the EIS device that is used for getting reference measurements for this study, Gamry Reference 3000, costs nearly 20.000$, only for the base device. Moreover, generally such devices are not suitable for online applications. Thus, there is an interest to propose different methods that are in compliance with the research objectives expressed earlier. In this section, a summary of current state of the art online EIS applications for batteries are presented.

There are several studies in literature offering online EIS measurements of batteries. One of the preferred approaches is to excite the battery current with the help of an programmable electronic load and perform EIS with the resulting voltage and current waveforms. Such an approach has been presented in [21], where broadband impedance spectroscopy (BIS) that utilizes a signal comprised of multiple sine waves and EIS, which is based on single frequency excitation, have been compared. The authors have also discussed the optimization of the multi-sine excitation signal and gives a brief summary to conventional battery tests. The proposed multi-sine signal is applied to the battery via an electronic load.

A study, [22], investigates a method for online battery impedance measurement for batteries. The study presents the measurement process by two different noise excitation sources. In the former case, the battery is excited by an electronic load, which is controlled by an external signal. In the latter case, the battery is excited by a motor controller and a brushless permanent magnet motor operating in current control mode. The complex impedance of the batteries are obtained by cross correlation technique. The method was applied to two battery types, Lithium-iron-phosphate (LFP) and nickel–manganese–cobalt oxide (NMC) batteries. Estimation of SOC for LFP batteries found to be challenging, while it is stated that estimation is possible for NMC batteries.

There are more studies on the utilization of electronic loads for EIS analysis. One such study, [23], presents how such an electronic load may be designed.

The study in [24] presents a measurement circuit and EIS calculation unit wherein a battery charger is controlled to charge a battery with a sinusoidal current injected DC current. The circuits extracts the AC parts of the battery current and voltage waveforms There are also further peak detection and zero-crossing sensing circuits for detecting the magnitude and the phase shift of the signals to calculate the impedance of a battery at each single frequency.

A recent trend is to develop integrated circuits (ICs) that can equip power systems with EIS capabilities by enabling sinusoidal current injections to the batteries. One such study is demonstrated in [25], where each cell of a battery pack is accompanied by a corresponding IC.

An alternative approach for online EIS systems is to integrate the EIS functionality into the power converter, which regulates the energy transfer within the battery system. One such study [26] intends to perform an online impedance spectroscopy for a sealed lead-acid (SLA) battery with the purpose of battery characterization. The impedance spectroscopy is achieved by altering the controller reference of the DC-DC converter to inject ac currents into battery charging current at varying frequencies. This procedure is repeated separately for each frequency. In this case values are between 0.32 Hz and 1024 Hz. The test at 0.32 Hz approximately takes 15 seconds. The study successfully obtains the complex impedance at different SOCs of the battery [26].

Another study, [27], presents a three level DC-DC converter that has a built-in EIS functionality. The study also utilizes single frequency sinusoidal signal injection technique to the duty cycle command of the converter in order to obtain the impedance of the tested lithium ion battery for the frequencies of interest between 0.1 Hz to 2 kHz. The applied perturbated duty cycle signal is chosen to be 20% of the steady state duty cycle to maintain the stability and the linearity of the system.

A further sinusoidal signal injection based online EIS approach is presented in [28]. In this study, the reference current signal of a DC-DC converter is perturbed with a sinusoidal reference signal. Since the perturbation is applied to the reference command, the study emphasizes the importance of the stability of the controller. The study proposes a PI controller and a feed-forward compensation scheme and addresses how an stable controller can be designed.

Huang and Qahouq [29] obtains the impedance magnitude of a Lithium-Ion (Li-Ion) battery by injecting an ac duty cycle perturbation and measuring the current and voltage waveforms. The method uses the obtained information (the value of the charging current and DC-DC converter output voltage) to estimate the open circuit voltage (OCV) so that the SOC can be predicted. The study claims that the method can be applied to various battery types such as Li-Ion, SLA and nickel–metal-hydride (NiMH) batteries.

In [30], a sinusoidal signal excitation based online EIS approach for a phase shifted full bridge converter, wherein the sinusoidal perturbation signal swept over the range of interest, is presented. Experimental results for a lead-acid battery between 0.1 Hz to 1 kHz are presented.

Another online EIS application for a synchronous buck converter by sinusoidal current injection to the output of the converter is presented in [31]. Similar to [30], the perpetuated signal is swept over the frequency range of interest. For demonstrating a practical example, a lithium-ion battery is tested for a frequency range of 0.1 Hz to 5 kHz. The results are compared with respect to offline measurements, which shows a deviation from the online results in higher frequencies.

Another swept sinusoidal signal perturbation based approach is presented in [32]. Similarly, the perturbation is applied at the reference command of the controller. Experimental results from 0.1 Hz to 1 kHz for a lead-acid battery are presented, which shows a good correlation to the results obtained by a commercially available EIS device.

Lee *et al.* [33] integrated an online impedance measurement system into a high power battery charger by injecting an ac current ripple on a DC charging current. The frequency of the injected ac current ripple is swept from 0.1 Hz to 100 Hz. The impedance data are obtained by transferring the current and voltage signals into a stationary rotating coordinate system.

Reference [34] presents the results of an online EIS capable boost converter operating at open loop, wherein the EIS is performed by injecting single sinusoidal perturbations to the duty cycle, at the frequencies of interest. The study discusses the effects of signal perturbations to the duty cycle.

A further study utilizing sinusoidal current injection is also demonstrated in [35]. This study focuses on a linear battery charger, which is also used to amplify the desired AC current signals for being injected onto the battery. As traditionally, the study again proposes to inject sinusoidal AC currents for each frequency of interest.

Application of multi-sine signal injection is also a popular concept in the field. One such study, [36], demonstrates that a perturbation signal, which is comprised of a sum of multiple sinusoidal signals, can be injected to duty cycle command of a bidirectional DC-DC converter in order to obtain EIS measurements for a lithium-ion battery. The results are then compared with EIS results obtained by excitation of the battery with an electronic load, wherein a good correlation is observed.

Another interesting study presents a design methodology for DC-DC converters specifically aimed at performing online EIS measurements [37] by taking into account some factors such as minimum switching ripple need, end of charge conditions and proposes an optimization process for possible suitable design parameter sets.

In addition to the sinusoidal current/voltage injection techniques, some non-sinusoidal signal injection techniques has been also discussed in the literature with respect to online battery impedance measurement appplications. In one such study [38], the authors explore the possibility performing EIS measurements on batteries via the help of an additional circuit comprising a mosfet and a resistor, wherein the resistor is basically switched on/off for drawing a square wave current from the battery. The same research group later on compares the method with square waves injected via duty cycle perturbation to the duty cycle of the converters [39].

The study [40] compares non-sinusoidal excitation of the battery currents with regards to the suitability to the EIS. Moreover, a practical online EIS system consisting of commercial components, such as battery charger/discharger, power controller and data acquisition system, has been set up for performing EIS measurements on a kilowatt-class battery system. In this study, periodic square, triangular and sawtooth waveforms are investigated. It is concluded that the square wave current injection on battery is the most convenient option.

A further EIS measurement application implemented for an bidirectional battery charger based on the half-bridge topology is presented in [41]. The study aims to provide a guideline for designing a precise controller that is able to excite the battery with a triangular current waveform, so that it is be possible to identify the battery impedance by making use of fourier transforms.

Another popular method is to implement a functionality into DC-DC converters that would enable injecting a square wave voltage signal at the output of the converter. One such study, [42], demonstrates the application of square wave voltage injection implemented into a power DC-DC converter operated at closed loop. The study points out that instead of single sinusoidal signal injection, the method offers to obtain results for a plurality of frequencies in a single test. The study also shows that a square wave voltage injection is easier to implement.

Another study, [43], proposes to inject a square wave signal to the duty cycle command. The proposed approach is demonstrated for a boost converter. They also point out that the testing time is significantly shorter than applying single frequency sinusoidal perturbations.

Similar to the square wave signal injection approach, [44] demonstrates that the pulse waves which already occur during cell balancing process in a multi-level converter (MMC) may be used for deriving the complex impedance of the battery. The study further demonstrates the possibility of reconfiguring a part of the MMC to inject sinusoidal currents to the battery over the inductances of the motor windings.

In [45], again the square-wave-like waveforms occurring during cell equalization among battery cells are used for performing EIS calculation. In the study, it is proposed to deploy a simple flying capacitor circuit in addition to the existing switch-matrix flying capacitor equalizer circuits, so that EIS can be performed on each individual battery cells. Similarly, [46] demonstrates that EIS measurements may be integrated into the existing battery cell equalizaiton circuits for performing EIS on each cell.

In [47] the researches apply a ternary sequence signal and a PRBS signal to the reference current command of a bidirectional power supply. They conclude that the results obtained by ternary sequence are better, especially in the low frequency region, while being able to maintain a lower current injection amplitude at the output of the converter. They validate their results by performing Kronig-Kramers compliance tests.

A further study, [48], proposes not to inject any signal and to perform EIS calculations based on ripple signals that naturally exist in a DC-DC converter system. The study points out that, this approach is only suitable for high frequency impedance measurements.

1.3.4 Concluding remarks

The literature survey presented above reveals that the general approach of online battery impedance identification studies utilizing DC-DC converters is based on injecting a sinusoidal AC current or an AC perturbation signal in the control loop with a specific frequency on the battery charging current and to identify the phase shift and impedance magnitude from the voltage and current waveforms. However, this method requires the applied ac current to be repeated for all frequencies of interest.

Although there are several studies aimed at overcoming the shortcomings of sinusoidal signal injection approaches by using square-wave or multi-sine signals, there is still room to improve the EIS methods in online applications.

In the light of the literature survey given above, this thesis intends to implement the EIS capabilities to digitally controlled DC-DC converters for eliminating the need for extra circuits. Since DC-DC converters are very often utilized for charging/discharging purposes in power systems containing batteries, the study is directed to a very wide range of applications covering both mobile or stationary systems.

With this purpose in mind, it is proposed to benefit from the capabilities of the cross-correlation method, which has been already mentioned to be a viable solution for converter transfer function identification applications by the literature.

The cross-correlation-based identification procedure enables gathering information over a wide frequency range via single test, since all frequencies can be injected at the same time. The data range and resolution of the obtained results depend on sampling parameters and testing time [49]. Although cross-correlation-based converter identification techniques has been already acknowledged in the literature, there are only few studies aimed at implementing the technique on for identification of network impedances [50] and passive impedance networks [49]. The study presented herein is an improved application of cross-correlation technique for identification of battery impedances. The technique proposed here has been published in [51].

2. CROSS-CORRELATION BASED SYSTEM IDENTIFICATION

This section aims to explain the basic principles on which the proposed EIS measurement system will be based.

2.1 Convolution Theorem

As it will be clearer in the succeeding chapters, system identification methods are highly related to the convolution theorem, which is used to define the system transfer functions. Thus, a brief overview of the convolution theorem is included in this chapter.

2.1.1 Convolution

The impulse response is may be described as the response of a linear system to an unit impulse. Let's consider a system having an input port and an output port, as illustrated in Fig. 2.1. The output of a system corresponding to any given signal may be calculated, given that the impulse response is known. This calculation process of the output response of a system is called convolution.

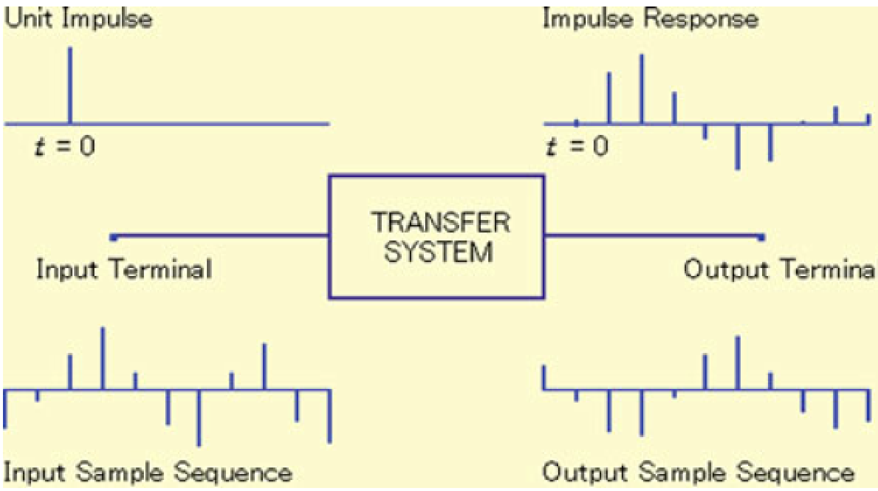

Figure 2.1 : Illustration of convolution theorem [52].

The output response of the system to a single impulse can be calculated by multiplying the unit response of the system by the magnitude of that said single impulse. In real life, systems do not generate an output before the start of an input signal entry. Such systems are called causal systems, where the impulse response is always zero for $t < 0$, $t = 0$ being the start of the input signal.

When a signal with more than one impulse is applied to the system, the system output is calculated as follows: each output sequence caused by each single impulse equals to the impulse response that is scaled by the magnitude of each corresponding impulse signal. Furthermore, each individual output sequence is also shifted by the lag of each corresponding input impulse. Finally, each calculated output sequence is superimposed, given that the system is linear. This operation is illustrated in Fig. 2.2.

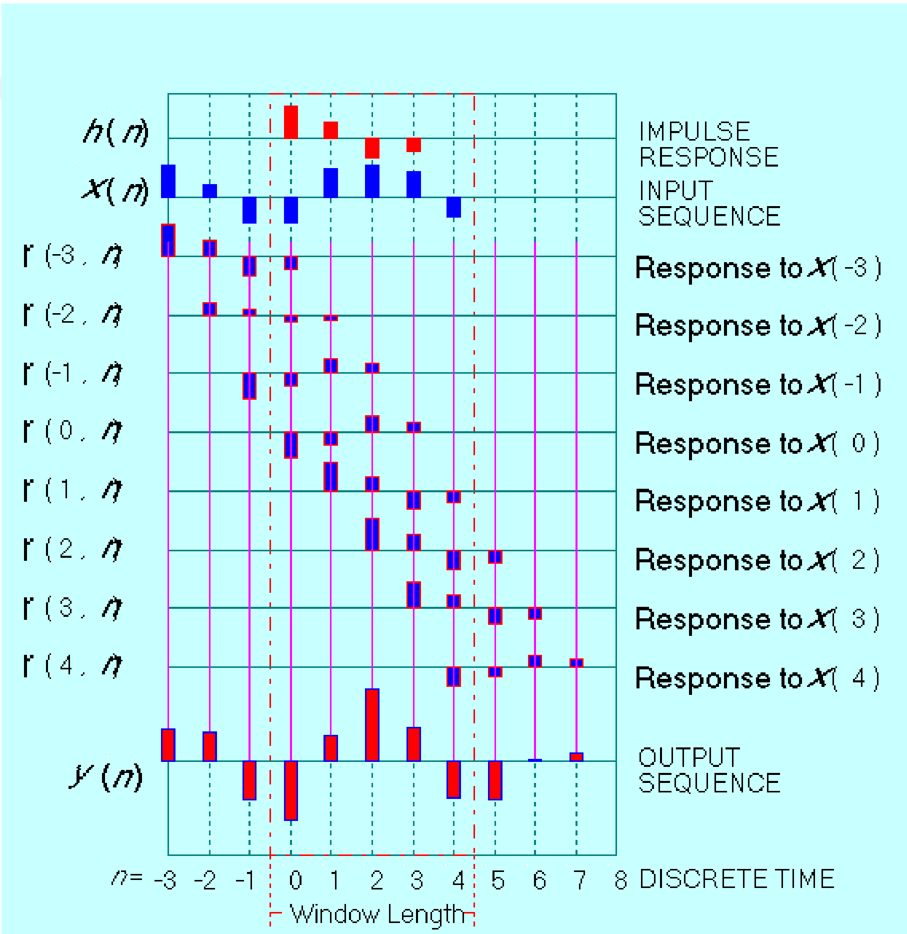

Figure 2.2 : Illustration of convolution theorem [52].

Mathematically, this calculation process can be expressed as:

$$y(n) = \sum_{p=0}^{m-1} x(n-p)h(p) \tag{2.1}$$

where $x(n)$ corresponds to the input sequence, $y(n)$ corresponds to output sequence, $h(n)$ is the impulse response of the system and m is the signal length. The convolution operation is often expressed as:

$$y(n) = x(n) * h(n) = h(n) * x(n) \tag{2.2}$$

The above given equations relate to digital systems. The corresponding representation of the convolution operation is as follows:

$$y(t) = \int_0^T x(t-\tau)h(\tau)d\tau \tag{2.3}$$

The above given formula corresponds to causal systems, however it may be also rewritten in a more general formula for any system of $h(t)$ as follows:

$$y(t) = \int_{-\infty}^{+\infty} x(t-\tau)h(\tau)d\tau \tag{2.4}$$

2.1.2 Fourier transform of the convolution

The FFT of the convolution is a powerful tool for reducing the computational load by performing the major part of the calculations in the frequency domain. Thus, here the FFT of the convolution operation will be studied.

The FFT of a convolution of $x(t)$ and $h(t)$ is given by:

$$FT[x(t) * h(t)] = \int_{-\infty}^{+\infty} \int_{-\infty}^{+\infty} x(t-\tau)h(\tau)d\tau \; e^{-j2\pi ft}dt \tag{2.5}$$

The above given equation may be rewritten as follows by using the transformation of $u = t - \tau$:

$$FT[x(t) * h(t)] = \int_{-\infty}^{+\infty} \int_{-\infty}^{+\infty} x(u)h(\tau)d\tau \; e^{-j2\pi f(u+\tau)}dt \tag{2.6}$$

$$= \int_{-\infty}^{+\infty} \int_{-\infty}^{+\infty} x(u)e^{-j2\pi f(u)}h(\tau) \; e^{-j2\pi f(\tau)}dud\tau \tag{2.7}$$

$$= \int_{-\infty}^{+\infty} x(u)e^{-j2\pi fu}du \int_{-\infty}^{+\infty} h(\tau) \; e^{-j2\pi f\tau}d\tau \tag{2.8}$$

$$= \int_{-\infty}^{+\infty} x(u)[x(t) * h(t)]e^{-j2\pi ft}dt = X(f)H(f) \tag{2.9}$$

Here $H(f)$ represents the transfer function of the system $h(t)$ in the frequency domain. By applying the inverse Fourier transform the following equation is then derived:

$$x(t) * h(t) = \int_{-\infty}^{+\infty} [X(f)H(f)]e^{j2\pi ft}dt = IFT[X(f)H(f)] \tag{2.10}$$

Moreover, by taking into account that the Fourier transform is symmetrical, the following equations can be derived:

$$x(t)h(t) = \int_{-\infty}^{+\infty} [X(f) * H(f)] e^{j2\pi ft} dt = IFT[X(f) * H(f)] \tag{2.11}$$

$$FT[x(t)h(t)] = \int_{-\infty}^{+\infty} x(t)h(t)e^{-j2\pi ft} dt = X(f) * H(f) \tag{2.12}$$

While the above equations are derived for continuous functions, they are also valid for discrete sampled sequences as well.

For the discrete systems, the convolution operation was already defined as:

$$y(n) = \sum_{p=0}^{m-1} x(n-p)h(p) \tag{2.13}$$

The DFT of discrete time convolution is:

$$Y(k) = \sum_{p=0}^{m-1} \sum_{p=0}^{m-1} x(n-p)h(p)e^{-jkn/N} \tag{2.14}$$

By introducing the parameter $q = n - p$, the above equation is rewritten as:

$$Y(k) = \sum_{p=0}^{m-1} \sum_{p=0}^{m-1} x(q)h(p)e^{-jk(q+p)/N} \tag{2.15}$$

$$= \sum_{p=0}^{m-1} x(q)e^{-jkq/N} \sum_{p=0}^{m-1} h(p)e^{-jkp/N} \tag{2.16}$$

This equation is expressed simply as:

$$Y(k) = DFT[x(n) * h(n)] = X(k)H(k) \tag{2.17}$$

The inverse Fourier transform operation trivially results in:

$$y(n) = x(n) * h(n) = IDFT[X(k)H(k)] \tag{2.18}$$

Similar to the continuous case:

$$x(n)h(n) = \frac{1}{N^2} \sum_{k=0}^{N-1} X(k)e^{j2\pi kn/N} \sum_{p=0}^{N-1} H(p)e^{j2\pi pn/N} \tag{2.19}$$

$$= \frac{1}{N^2} \sum_{k=0}^{N-1} \sum_{p=0}^{N-1} X(k)H(p)e^{j2\pi(k+p)n/N} \tag{2.20}$$

Now, by defining another parameter, $r = k + p$, the following equations are derived:

$$x(n)h(n) = \frac{1}{N^2}\sum_{r=0}^{N-1}\sum_{k=0}^{N-1} X(k)H(r-k)e^{j2\pi rn/N} \tag{2.21}$$

$$= \frac{1}{N^2}\sum_{r=0}^{N-1}[X(r)*H(r)]e^{j2\pi rn/N} \tag{2.22}$$

$$= \frac{1}{N^2}IDFT[X(k)*H(k)] \tag{2.23}$$

The difference between the time domain and frequency domain versions of the above given equations is that the number of calculations are reduced by the FFT version, especially for the longer data lengths.

2.2 Correlation

2.2.1 Similarity of two signals

In principle, correlation is a function for representing the relationship between two functions, such as $x(n)$ and $y(n)$. Although, these two signals does not necessarily need to be time signals, since the primary interest generally lies in them, it will be assumed that $x(n)$ and $y(n)$ are considered to be samples of time signals. It is evident that the case of two signals being identical represents the highest similarity situation. This degree of similarity may be assessed by calculating the squares of differences between these two signals with respect to the corresponding times, and by adding up these differences.

However, when the case of two signals being same with the exception of being different in magnitude would be considered, it would be trivially concluded that there would be differences in the signals at corresponding times, this may inaccurately cause the analysis to indicate a low correlation between the signals, even though in reality they would be only different in the magnitude. Thus, a need for normalization process arises, so that the analysis focuses more on the similarity between waveforms of the signals rather than their magnitudes.

With this respect, the normalization process comprises the division of signals by their respective standard deviations, which may be seen as the effective amplitude of a signal. In this way, the influence of the magnitude difference between the signals may be eliminated. Furthermore, it is also possible to remove the DC components of the signals, if the interest lies in the changes of the waveforms.

The standard deviations of the signals may be calculated as:

$$\sigma_x = \sqrt{\frac{1}{L}\sum_{n=0}^{L-1}(x(n)-\bar{x})^2} \tag{2.24}$$

$$\sigma_y = \sqrt{\frac{1}{L}\sum_{n=0}^{L-1}(y(n)-\bar{y})^2} \tag{2.25}$$

where $\bar{x}$ and $\bar{y}$ are mean values and L is the length of the signals. In the sake of simplicity, it is now assumed that the mean values are zero for both signals.

Consequently, the following formula can be derived for expressing the sum of squares of the differences between two signals, x(n) and m-time shifted signal y(m+n).

$$e_m{}^2 = \frac{1}{L}\sum_{n=0}^{L-1}\{\frac{x(n)}{\sigma_x} - \frac{y(m+n)}{\sigma_y}\}^2 \tag{2.26}$$

$$e_m{}^2 = 2\{1 - \frac{1}{L\sigma_x\sigma_y}\sum_{n=0}^{L-1}(x(n)y(m+n))\} \tag{2.27}$$

When the two signals, x(n) and y(m+n), are identical this equation equals to 0, therefore giving an indication of the similarity between them.

2.2.2 Cross-correlation

As it can be understood trivially from the Equation (2.27), only a part of the equation can be used for the evaluation of the degree of similarity:

$$r_{xy}(m) = \frac{1}{L\sigma_x\sigma_y}\sum_{n=0}^{L-1}(x(n)y(m+n)) \tag{2.28}$$

$$= \frac{\sum_{n=0}^{L-1}(x(n)y(m+n))}{\sqrt{\sum_{n=0}^{N-1}x^2(n)}\sqrt{\sum_{n=0}^{N-1}y^2(n)}} \tag{2.29}$$

The above given equations are defined as the cross-correlation function, $r_{xy}(m)$, where the m is defined as the lag.

Furthermore, it can also be seen that this function is quite similar to the convolution function. Both functions are illustrated in Fig. 2.3 for comparison purposes.

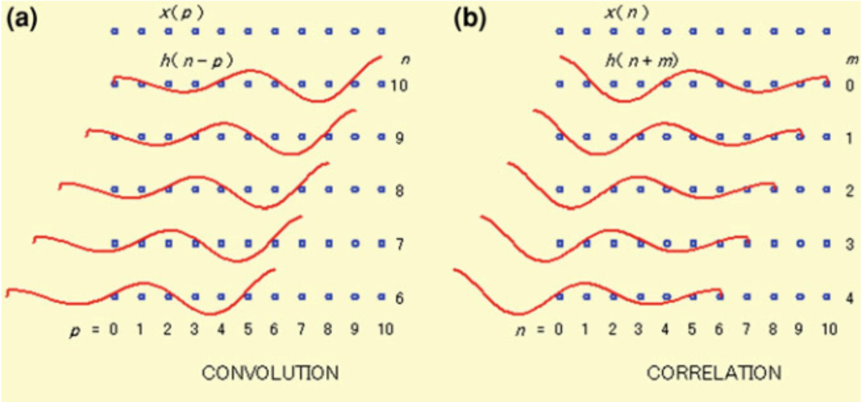

Figure 2.3 : Illustration of convolution and cross-correlation operations in a comparative context [52].

As it can be seen from the figure, the cross-correlation operation of $x(n)$ and $y(n)$ requires that each $x(n)$ is multiplied by its corresponding $h(n)$ that is shifted by m samples to forward, and all the product terms are then added.

On the other hand, the convolution operation requires that each $x(p)$ and its corresponding $h(n-p)$ is multiplied.

When we consider the cross-correlation of two sequences, which are identical except the lag m, meaning that $y(n) = x(n-m)$, the cross-correlation of these signals will be equal to 1 for the lag m.

This is illustrated on a random number sequence in Fig. 2.4 for different lengths of random sequence.

As it can be seen from the figure, a large number of averaging is quite necessary for obtaining reliable results by cross-correlation, as low values of averaging number, L, cannot detect the correlation of two signals.

2.2.3 Auto-correlation

The auto correlation of a signal means that the correlation operation is performed on the same signal, which can be expressed as follows:

$$r_{xx}(m) = \frac{1}{L{\sigma_x}^2} \sum_{n=0}^{L-1} x(n)x(m+n) \tag{2.30}$$

Obviously the result of auto-correlation is a sequence that is equal to 1 at $m = 0$. Furthermore, if the sequence is random the auto-correlation must be zero except for $m = 0$. Fig. 2.5 illustrates auto-correlation of different functions.

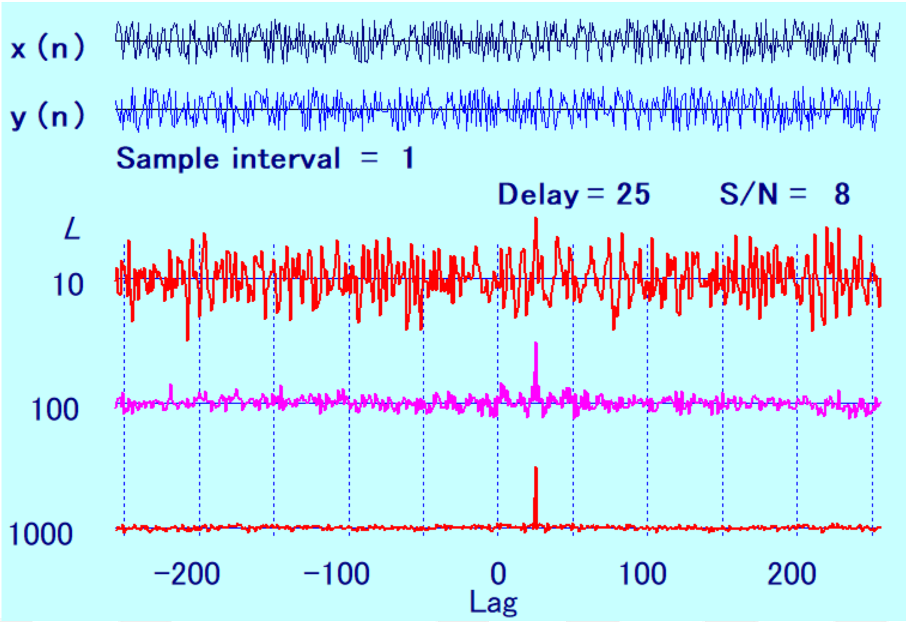

Figure 2.4 : Cross-correlation of a random sequence and the sequence shifted by 25-samples, illustrated for various averaging numbers L [52].

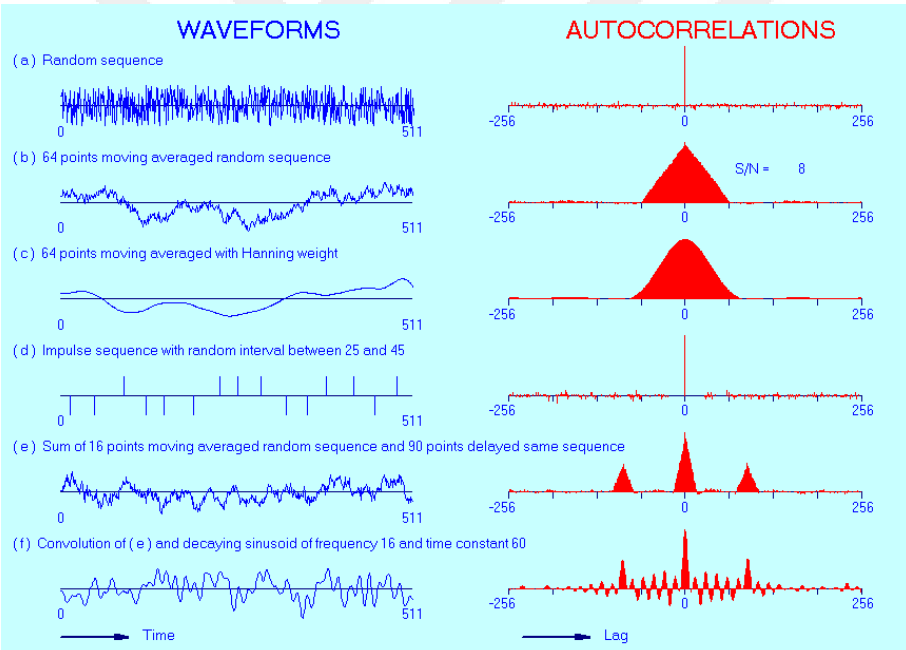

Figure 2.5 : Auto-correlation of different functions [52].

2.2.4 Cross-correlation between input and output signals

Now, for a system having a transfer function of $h(n)$, an input signal of $x(n)$ and an output signal of $y(n)$, while calculating the cross-correlation of the input and output signals, we should take into consideration that $y(n)$ can be expressed in terms of $x(n)$

and $h(n)$:

$$y(n) = \sum_{p=0}^{K-1} x(n-p)h(p) \tag{2.31}$$

$$r_{xy}(m) = \frac{1}{L\sigma_x\sigma_y}\sum_{n=0}^{L-1}(x(n)y(m+n)) \tag{2.32}$$

By combining the both equations above, we can derive the cross-correlation between and input and output signal of a system as follows:

$$r_{xy}(m) = \frac{1}{L\sigma_x\sigma_y}\sum_{n=0}^{L-1}x(n)\sum_{p=0}^{K-1}x(n+m-p)h(p) \tag{2.33}$$

$$r_{xy}(m) = \frac{1}{L\sigma_x\sigma_y}\sum_{p=0}^{K-1}h(p)\sum_{n=0}^{L-1}x(n)x(n+m-p) \tag{2.34}$$

2.2.5 Fourier transform of auto-correlation

Up to this point, all the equations are derived considering that the sequences have been formed by real numbers. However, for future uses, it is also quite useful the consider the case where these sequences may be formed by complex numbers.

However, in the case where the sequences of the functions include complex numbers, the resulting auto-correlation function will also be bound to include such numbers. A trick to avoid that is to the conjugate of the sequence. Thus, the Eq. 2.30 may be rewritten as follows:

$$r_{xx}(m) = \frac{1}{L{\sigma_x}^2}\sum_{n=0}^{L-1}x^*(n)x(m+n) \tag{2.35}$$

where $x^*(n)$ represents the conjugate of $x(n)$.

Furthermore, for a continuous function the auto-correlation may be expressed as:

$$r_{xx}(\tau) = \frac{1}{T{\sigma_x}^2}\int_0^T x^*(t)x(t+\tau)dt \tag{2.36}$$

where T corresponds to the range of the waveform. Additionally, if the signal is indefinite, the limits of the integration may be defined to be between $-\infty$ to $+\infty$. Furthermore, the above given standard deviation, σ_x may be expressed as:

$$\sigma_x = \sqrt{\frac{1}{T}\int_0^T x^2(t)dt} \tag{2.37}$$

Once we have a formulation for the auto-correlation of a continuous signal, we can also derive a formulation for the Fourier transform for that formulation:

$$FT[r_{xx}] = \frac{1}{{\sigma_x}^2}\int_{-\infty}^{+\infty}\int_{-\infty}^{+\infty} x^*(t)x(t+\tau)dte^{-j2\pi f\tau}d\tau \tag{2.38}$$

This equation may be manipulated by replacing $t+\tau$ by u:

$$FT[r_{xx}] = \frac{1}{{\sigma_x}^2}\int_{-\infty}^{+\infty}\int_{-\infty}^{+\infty} x^*(t)x(u)dte^{-j2\pi f(u-t)}du \tag{2.39}$$

$$= \frac{1}{{\sigma_x}^2}\int_{-\infty}^{+\infty}\int_{-\infty}^{+\infty} x^*(t)x(u)e^{j2\pi ft}dte^{-j2\pi fu}du \tag{2.40}$$

The above equation would then correspond to:

$$FT[r_{xx}] = R_{xx}(f) = \frac{1}{{\sigma_x}^2}X^*(f)X(f) \tag{2.41}$$

which is basically calculated by the Fourier transforms of the $FT[x(t)] = X(f)$.

Furthermore, we can even take a step further to calculate the Discrete-Fourier transforms (DFT) of the auto-correlation, which may be very useful, as the discrete time sampled systems are quite often utilized.

So far, the term L has been used to represent the number of averages for calculating the auto-correlation. From this point on, the L is replaced by N, which corresponds to the data number of the DFT.

Consequently, the DFT of auto-correlation is defined as:

$$R_{xx}(k) = DFT[r_{xx}] = \frac{1}{N{\sigma_x}^2}\sum_{m=0}^{N-1}\sum_{m=0}^{N-1} x^*(n)x(n+m)e^{-j2\pi\frac{mk}{N}} \tag{2.42}$$

By using the conversion of $p = n+m$ and by replacing the $x(p)$ with $x(p-N)$:

$$R_{xx}(k) = \frac{1}{N{\sigma_x}^2}\sum_{p=0}^{N-1}\sum_{p=0}^{N-1} x^*(n)x(p)e^{-j2\pi\frac{pk}{N}}e^{j2\pi\frac{nk}{N}} \tag{2.43}$$

$$= \frac{1}{N{\sigma_x}^2}\sum_{p=0}^{N-1}\sum_{p=0}^{N-1} x^*(n)e^{j2\pi\frac{nk}{N}}x(p)e^{-j2\pi\frac{pk}{N}} \tag{2.44}$$

$$= \frac{1}{N{\sigma_x}^2}X^*(k)X(k) = \frac{1}{N{\sigma_x}^2}|X(k)|^2 \tag{2.45}$$

2.2.6 Fourier transform of cross-correlation

Similar to the auto-correlation case, the cross-correlation for complex numbers can be expressed as:

$$r_{xy}(m) = \frac{1}{L\sigma_x\sigma_y}\sum_{n=0}^{L-1} x^*(n)y(m+n) \quad (2.46)$$

Consequently, the cross-correlation of a continuous function may be written as:

$$r_{xy}(\tau) = \frac{1}{T\sigma_x\sigma_y}\int_0^T x^*(t)y(t+\tau)dt \quad (2.47)$$

Analogous to the auto-correlation case the Fourier transform of the cross-correlation can be expressed as:

$$FT[r_{xy}] = R_{xy}(f) = \frac{1}{\sigma_x\sigma_y}X^*(f)Y(f) \quad (2.48)$$

Now, going back to Eq. 2.9, which states that $FT[x(t)*h(t)] = FT[y(t)] = Y(f) = X(f)H(f)$, we can rewrite the above equation as:

$$R_{xy}(f) = \frac{1}{\sigma_x\sigma_y}X^*(f)X(f)H(f) \quad (2.49)$$

According to Eq. 2.41, $X^*(f)X(f) = R_{xx}(f)\sigma(x)^2$, so that the above equation may be rewritten as:

$$R_{xy}(f) = \frac{\sigma_x}{\sigma_y}R_{xx}(f)H(f) \quad (2.50)$$

Furthermore, the DFT of the cross-correlation is also expressed as:

$$R_{xy}(k) = \frac{1}{N\sigma_x\sigma_y}X^*(k)Y(k) \quad (2.51)$$

where $X(k)$ and $Y(k)$ correspond to DFT of $x(n)$ and $y(n)$.

Consequently, similar to the FT case, te above equation may be rearranged as by considering Eq. 2.17 and Eq. 2.45:

$$R_{xy}(k) = \frac{\sigma_x}{\sigma_y}R_{xx}(k)H(k) \quad (2.52)$$

2.3 Cross-Correlation Based Identification

As it is given in the previous chapter, a formulation can be derived representing a relationship between the transfer function of an LTI system and the correlation functions. Furthermore, this relationship may be also used for identifying the transfer functions of these systems [53], [54].

However, in real-life, all the systems are influenced by the some noise which may be modelled as disturbances. Lets now consider such a sampled LTI system with a transfer function of $h[n]$, having an output response $y[n]$, to the input signal $x[n]$:

$$y[n] = x[n]^{*}h[n] = \sum_{k=-\infty}^{\infty} h[n-k]x[k] + v[n] = \sum_{k=-\infty}^{\infty} h[k]x[n-k] + v[n] \tag{2.53}$$

The unwanted disturbances, such as the noise, are represented as $v[n]$. The cross correlation of input $x[n]$ and output $y[n]$ is defined as:

$$w_{xy}[m] = \sum_{n=1}^{\infty} x[n]y[n+m] = \sum_{n=1}^{\infty} h[n]w_{xx}[m-n] + w_{xv}[m] \tag{2.54}$$

Here, $w_{xx}[m]$ represents the auto-correlation of input signal, whereas the cross-correlation of input signal and disturbances are disturbances represented as $w_{xv}[m]$. Please also notice that the correlation functions defined above differ from the ones presented in the previous chapter in that they are not normalized. Thus, they are represented with a different symbol, w. These correlation terms are mathematically defined as:

$$w_{xx}[m] = \sum_{n=1}^{\infty} x[n]x[n+m] \tag{2.55}$$

$$w_{xv}[m] = \sum_{n=1}^{\infty} x[n]v[n+m] \tag{2.56}$$

As shown in the previous chapter, Equ. 2.54 can be represented in frequency domain by performing the Fourier transform:

$$W_{xy}(f) = H(f)W_{xx}(f) + W_{xv}(f) \tag{2.57}$$

$$H(f) = \frac{W_{xy}(f) - W_{xv}(f)}{W_{xx}(f)} \tag{2.58}$$

When the input signal is white noise, the auto-correlation and cross-correlation functions exhibit the following properties:

$$w_{xv}[m] = 0 \tag{2.59}$$

$$w_{xx}[m] = \sigma^2 \delta[m] \tag{2.60}$$

where σ is the standard deviation of the input signal. Considering the mentioned properties, the Eq. 2.58 can be expressed as:

$$H(f) = \frac{W_{xy}(f)}{W_{xx}(f)} = \frac{W_{xy}(f)}{\sigma^2} \quad (2.61)$$

As shown above, the system transfer function is now represented in frequency domain as $H(f)$.

2.4 Identification of DC-DC Converter Transfer Functions

As shown in previous section, the transfer functions of systems can be derived by stimulating the system with white noise at the input and calculating the cross-correlation of the output signal.

A DC-DC converter operating in steady state may be regarded as an LTI system. By applying small-magnitude signals, a small-signal transfer function of the DC-DC converter may be derived using the cross-correlation technique.

In this context, for the purpose of analysing the converter transfer functions, the input signal is considered to be the duty cycle command of the converter while the output signals may be regarded as the disturbances of the output voltage and output current waveforms.

Therefore, by applying a noise-like perturbation signal, $\hat{d}_{per}$, to the duty cycle command of a converter, D_{cnt}, which results in a total duty cycle of D, the control to output voltage transfer function of the converter, $G_{vd}(s) = \frac{\hat{v}(s)}{\hat{d}(s)}$, and control to output current transfer function, $G_{id}(s) = \frac{\hat{i}(s)}{\hat{d}(s)}$, can be derived.

Consequently, the converter duty cycle to output transfer functions can be formulated as:

$$G_{vd}(s) = \frac{\hat{v}(s)}{\hat{d}(s)} = \frac{W_{xv}}{W_{xx}} = \frac{W_{xv}}{\sigma^2} \quad (2.62)$$

$$G_{id}(s) = \frac{\hat{i}(s)}{\hat{d}(s)} = \frac{W_{xi}}{W_{xx}} = \frac{W_{xi}}{\sigma^2} \quad (2.63)$$

where W_{xv}, W_{xi} and W_{xx} are the Fourier transforms of the output cross-correlation of the output voltage signal with duty cycle signal (w_{xv}), cross-correlation of the output current signal with duty cycle signal (w_{xi}) and the auto-correlation of the duty cycle signal (w_{xx}), respectively.

2.5 Impedance Measurement

As mentioned previously, the cross-correlation technique is based on applying a white-noise (WN) signal at the input of a system and observing the output of the system. For the intended use in this study, applying a WN as current/voltage to a battery and observing the voltage/current waveforms would be required. However, it may not be practical to build a circuit that could directly inject a white-noise-like current/voltage.

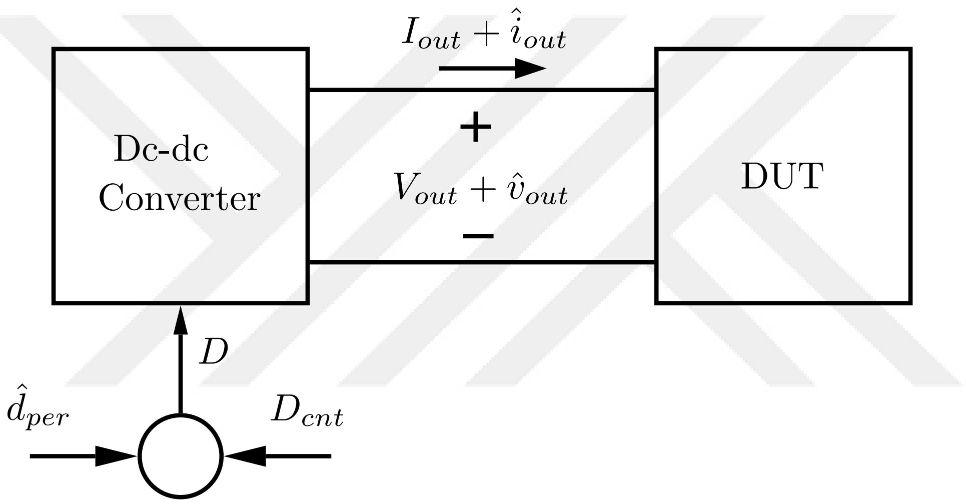

Figure 2.6 : Impedance measurement utilizing cross-correlation technique.

Thus, the impedance of a device under test (DUT) that is connected at the output of a DC-DC converter can be calculated by finding the both control to output voltage $G_{vd}(s)$ and control to output current $G_{id}(s)$ transfer functions of the converter and dividing the first one by the second.

As formulated below, the impedance of the load at the output of the DC-DC converter can be calculating by the division of these control transfer functions.

$$Z(f) = \frac{G_{vd}}{G_{id}} \tag{2.64}$$

$$G_{vd}(s) = \frac{W_{xv}}{W_{xx}} \tag{2.65}$$

$$G_{id}(s) = \frac{W_{xi}}{W_{xx}} \tag{2.66}$$

$$Z(f) = \frac{G_{vd}}{G_{id}} = \frac{W_{xv}}{W_{xi}} \tag{2.67}$$

the Fourier Transforms of the cross-correlation functions W_{xv} and W_{xv} can be expressed as;

$$W_{xv} = FT[x(n)]\, FT[v(n)] \tag{2.68}$$

$$W_{xi} = FT[x(n)]\, FT[i(n)] \tag{2.69}$$

Consequently, the Equation 2.67 can be simplified as:

$$Z(f) = \frac{FT[x(n)]}{FT[x(n)]} . \frac{FT[v(n)]}{FT[i(n)]} \tag{2.70}$$

$$Z(f) = \frac{FT[v(n)]}{FT[i(n)]} = \frac{\hat{v}(f)}{\hat{i}(f)} \tag{2.71}$$

In the ideal case, the input perturbation to duty cycle command is a WN signal, which exhibits previously mentioned properties. On the other hand, an ideal WN signal is impossible to derive. Many studies utilize pseudo-random-binary-sequence (PRBS) or other approximations. In this study, a random integer number WN approximation, which is added to the steady state duty cycle, is utilized for the intended application.

As mentioned previously, the cross-correlation technique excites all the frequencies in a single test, rather than testing the battery separately for each frequency. The upper limit, f_{stop}, lower limit, f_{start} and resolution Δf of the obtained frequency spectrum depend on the sampling frequency, f_s and number of acquired data points, K. Same quantities may also be expressed in terms of perturbation frequency, f_{per} and length of perturbation signal, N, as follows:

$$f_{start} = \frac{f_{per}}{N} = \frac{f_s}{K} \tag{2.72}$$

$$f_{stop} = \frac{f_s}{2} \tag{2.73}$$

$$\Delta f = \frac{f_{per}}{N} = \frac{f_s}{K} \tag{2.74}$$

One other critical parameter is the testing time of the DUT, which can be calculated as:

$$T_{test} = \frac{N}{f_0} = \frac{K}{f_s} = \frac{1}{f_{start}} \tag{2.75}$$

As it can be seen from equations above, the qualities of the EIS measurements by proposed approach depend on perturbation noise data length, perturbation frequency or sampling total number of recorded data points and sampling rate.

2.6 Pre- and Post-Processing Techniques for Improving the Battery Impedance Measurements

Within the scope of this thesis, some improvements for the cross-correlation method are proposed for the battery-specific impedance identification application. These suggestions aim to achieve better results considering the dynamic behaviour of the batteries.

2.6.1 Performing two separate tests with different noise colours

The literature survey reveals that, most important parameters for applications such as SOC and SOH estimation generally reside in the low-frequency region. Thus, it is of great interest for researchers to obtain impedance variation in the low-frequency region more precisely.

Consequently, it is proposed to perform two separate tests specifically aimed for low- and high-frequency impedance information as a further improvement. For this purpose, a red-noise (RN) signal, which has a higher power spectral density (PSD) in low-frequency, and a WN signal is injected separately into the duty cycle, D_{cnt}. The PSDs of produced RN and WN are illustrated in Fig. 2.7.

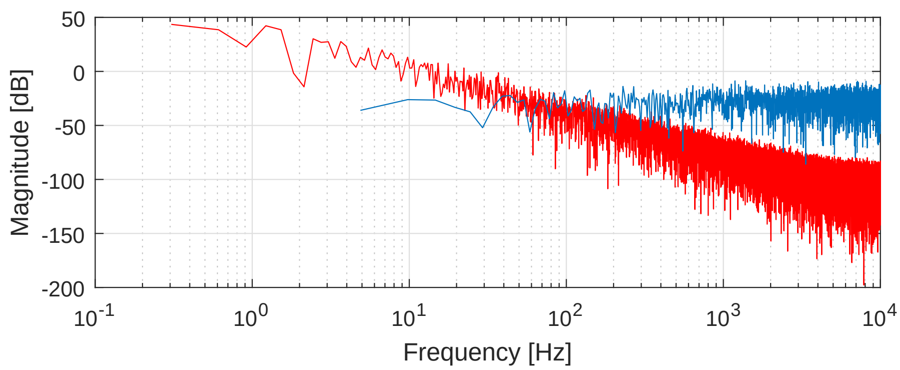

Figure 2.7 : Spectra comparison of applied perturbations for both tests.

It should also be noted that, since the power spectral density of the RN injection is very low in higher frequencies, the high-frequency impedance information during this test would be highly attenuated by the DC-DC converter, which would then result in an invalid data in this region. Therefore, the data from two tests are processed separately and then merged into one final dataset to have a clear representation of impedance information over a wide range of frequency.

The noise signals were prepared by using a set of random integers, which are added to the counter of the PWM generator during the testing procedure. The magnitude of the designed noise data are limited to be less than 10% of the maximum duty cycle, to enable stability and linearity [36].

For obtaining a RN dataset, the set of random integers is transferred to the frequency domain by taking the fourier transform. Afterwards, it is multiplied by a desired slope, which in this case is -20 dB/dec, so that the signal is more powerful in the low-frequency region. After taking the inverse fourier transform, the dataset for RN signal is achieved. As seen in Fig. 2.7, the intersection point of power spectral densities of two signals that are used in this study are around 100 Hz. Thus, the final data set is obtained by merging the RN injected test results up to 100 Hz and WN injected test results starting from 100 Hz.

2.6.2 Performing moving average on measured battery voltage and current waveforms

As mentioned previously, batteries are highly non-linear and dynamic devices. The first major issue in an on-line application is the fact that battery open circuit voltage continues to increase as the battery is being charged while it is under test.

For the impedance identification of the batteries, it is intended to utilize the perturbation-caused voltage and current waveforms during the test. Thus, other effects on the voltage and current waveforms, such as the increase in the open circuit voltage, should be somehow eliminated since they are not related to the impedance of the battery.

The cut-off frequency of the moving average filter is equal to $f_{co} = f_s/M$, where M is the window size of the filter. Using this equation, the correct window size can be chosen with regards to the frequency range of interest.

Although it is one of the most common filters, performing moving averages on the test data and subtracting it from the test data would be an effective way to obtain the voltage and current waveforms that are related to the perturbation of the duty cycle. $\hat{d}_{per}$. In Fig. 2.8 the battery voltage data during a test (blue curve) and the calculated moving average (red curve) is illustrated. The calculated moving average is then

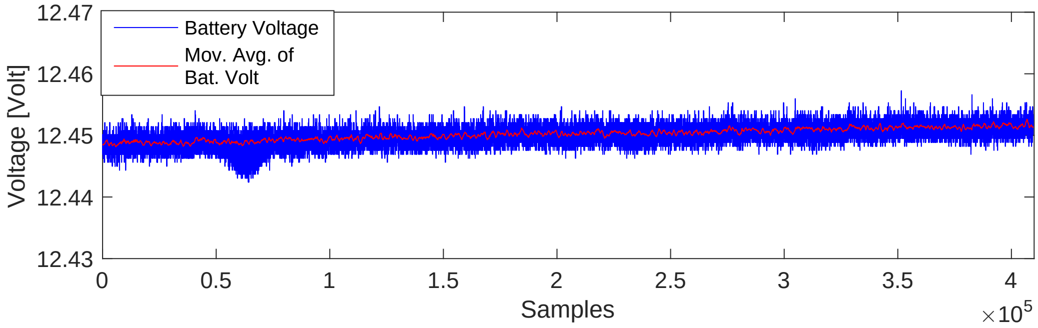

Figure 2.8 : Application of moving average on measured battery voltage.

subtracted from the original data, so that the result would be a good representative of the waveforms that are caused by the duty cycle perturbation for identification purpose, $\hat{d}_{per}$.

2.6.3 Post-processing the obtained frequency response data

In real-world applications, some mechanisms, such as noise from switching and EMI/EMC, ADC quantization process and measurement errors, might distort the obtained results. Therefore, some data processing techniques are generally required to smooth out the obtained results. The background work for some of these techniques have already been presented in [49].

2.6.3.1 Performing moving averages

Application of moving averages on the obtained results is a basic, simple way to smooth the obtained impedance diagrams. However, it is advised to care for choosing a suitable window size.

Moreover, for avoiding filter lag and consequently a shift in the frequency of the obtained results introduced by this filter, it is suggested to utilize the zero-lag moving average. A zero-lag moving average can be obtained by calculating the moving average, MA_L of desired window size, L, and a second moving average, $MA_{L/2}$, with a window size of $L/2$ [55]. Then the zero lag moving average, MA_0 is equal to:

$$MA_0 = MA_L - (MA_L - MA_{L/2}) \tag{2.76}$$

2.6.3.2 Median filter

Another useful technique is the median filter that principally checks each data point whether or not it is representative of its surrounding data points. The median filter replaces data that are not representative of its neighbors with the median value. Application of this technique ensures a further improvement in the processing of the obtained impedance data when a filter with a suitable window size is applied.

2.6.3.3 Fractional-decade processing

As mentioned in the explanations of previous techniques, choosing a reasonable window size is an important key to have affective results. To be able to smooth the obtained data, a reasonable window size should be determined concerning the number of data points and the frequency resolution. Clearly, a fixed window size over the complete frequency range should be avoided.

Consequently, it is suggested to choose different window sizes for each decade of the obtained impedance diagram which would assure better results. For the post-processing of the results obtained in the framework of this study, the total number of data points in each decade is calculated. Afterwards, for each decade one-hundredths and one-thousandths of these numbers are utilized as the window sizes for median filter and moving average filter, respectively.

2.6.3.4 Curve fitting based on an equivalent model

For further improvement, it is suggested to fit the obtained results also into an equivalent model. This way, it would be possible to clear the obtained results even further and enable more precise parameter estimation, on which a lot of EIS based applications rely on.

The equivalent battery model should be chosen carefully, depending on the battery type, so that a high correlation between the obtained results and fitted model could be achieved.

The equivalent battery model, which is chosen for fitting the obtained data, is given in Fig. 2.9. In a recent study, Aksakal and Sisman [56] reports that the electric equivalent circuit model comprised of inductance L_e, resistor R_e, Bisquert Short (BTS) elements Z_{BTS} and Constant Phase Elements CPE_1 in parallel with a resistor R_1 constituting

$Z_{CPE||R}$, exhibits the best correlation between the measurements and the models for enhanced flooded lead-acid batteries. For the test frequency range of this study, it has been seen that one CPE and one BTS element was enough to model the battery, whereas [56] suggests to use two CPEs and two BTSs for modeling a wider frequency range.

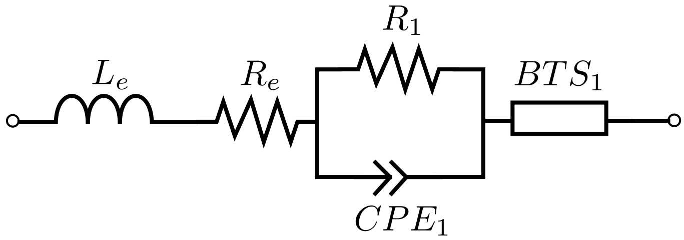

Figure 2.9 : The model used for curve fitting.

The BTS model utilized here is generally used for modeling transmission lines [57]. Bisquert showes that it can be used for modeling electrochemical devices [58]. On the other hand, the CPE models are used for imitating the non-ideal capacitor behavior, which appears as semi-circles on Nyquist plots [56]. The equations for CPE with a parallel resistor are given below:

$$Z_{CPE||R} = \frac{R}{1+(j\omega)^{\alpha}QR} \tag{2.77}$$

For the CPE models; the R and Q used for modeling the resistive and non-ideal capacitive behavior to the order α, respectively. On the other hand, the BTS component is formulated as:

$$Z_{BTS} = \sqrt{\zeta\chi}\, tanh(L_{BTS}\sqrt{\frac{\chi}{\zeta}}) \tag{2.78}$$

$$\zeta = \frac{r_{BTS}}{1+(j\omega)^{\alpha_{BTS}}q_{BTS}r_{BTS}} \tag{2.79}$$

where L_{BTS} is the depth of the pore within a porous electrode, χ is the impedance of the electrolyte within the pore, ζ describes the impedance at the active interface region on the surface of the electrode. Please note that ζ is actually a CPE element that is implemented into the BTS component. For avoiding any confusion, the parameters of ζ is denoted as; r_{BTS}, q_{BTS} and α_{BTS} instead of R, Q and α, respectively.

2.7 Concluding Remarks

The cross-correlation technique reviewed in this chapter has already been proven to be compatible for measuring the DC-DC converter transfer functions, which in turn can be used for measuring the impedance. Additionally, as shown in this chapter, the final equation for the impedance is simplified to the division of fourier transform of the output voltage disturbance by the fourier transform of the output current disturbance.

Moreover, this technique seems to be a promising concept for obtaining impedance diagrams of the devices under test. Specifically, it's ability scan a wide range of frequencies at one testing instance makes it a very good candidate for battery EIS measurements, as the dynamic behaviour of the batteries require the testing times to be relatively short.

As further shown in the chapter, with pre- and post-processing techniques, which are specifically aimed for improving the EIS results with of batteries of dynamic nature, a highly accurate and stable battery EIS measurement is envisaged.

3. VERIFICATION BY COMPUTER SIMULATIONS

This section aims to provide a first verification step by computer simulations for confirming the validity of the proposed approach. The simulation software used for this section is MATLAB Simulink.

3.1 Obtaining DC-DC Converter Transfer Functions

The principles of the proposed approach relies on identification of DC-DC converter transfer functions. Thus, this basic principle of the approach is demonstrated by a simulation designed for obtaining the control-to-output transfer functions of a DC-DC converter. For this purpose a boost converter model is built as shown in Figure 3.1.

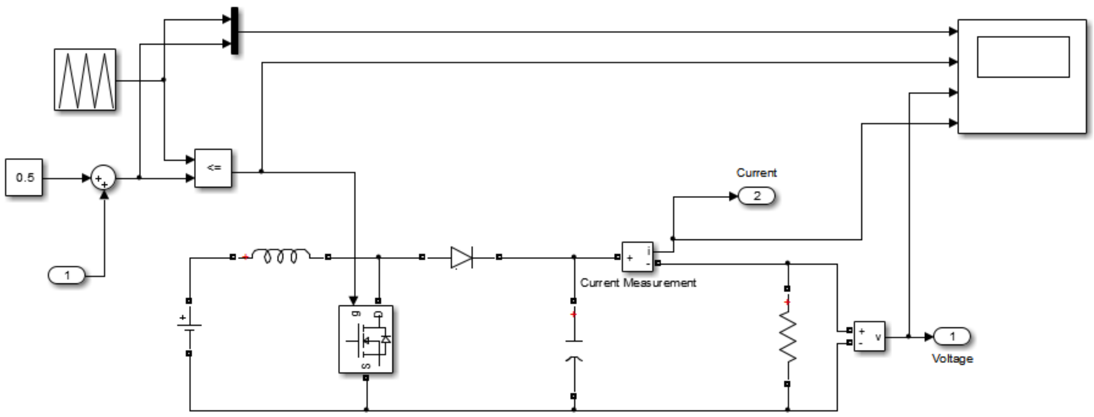

Figure 3.1 : The model of tested converter in the simulation.

The parameters of the boost converter are given in Table 3.1.

The control-to-voltage output transfer function of the converter is expressed as [59]:

$$G_{vd} = \frac{\hat{v}}{\hat{d}} = \frac{G_{d0}(1 - \frac{s}{\omega_z})}{\frac{s^2}{\omega_0^2} + \frac{s}{Q\omega_0} + 1} \tag{3.1}$$

Table 3.1 : Parameters of the simulated boost converter.

Parameter	Value [Unit]
Input Voltag,e V_g	15 Volts
Duty Cycle, D	0.5
Boost Inductor, L	100 μH
Output Capacitor, C	70 μF
Switching Frequency, f_s	100 kHz

where

$$G_{d0} = \frac{V}{(1-D)} \tag{3.2}$$

$$\omega_0 = \frac{(1-D)}{\sqrt{LC}} \tag{3.3}$$

$$\omega_z = \frac{(1-D)^2 R}{L} \tag{3.4}$$

$$Q = (1-D)R\sqrt{\frac{C}{L}} \tag{3.5}$$

The corresponding Bode Diagram of this transfer function is illustrated in Fig. 3.2.

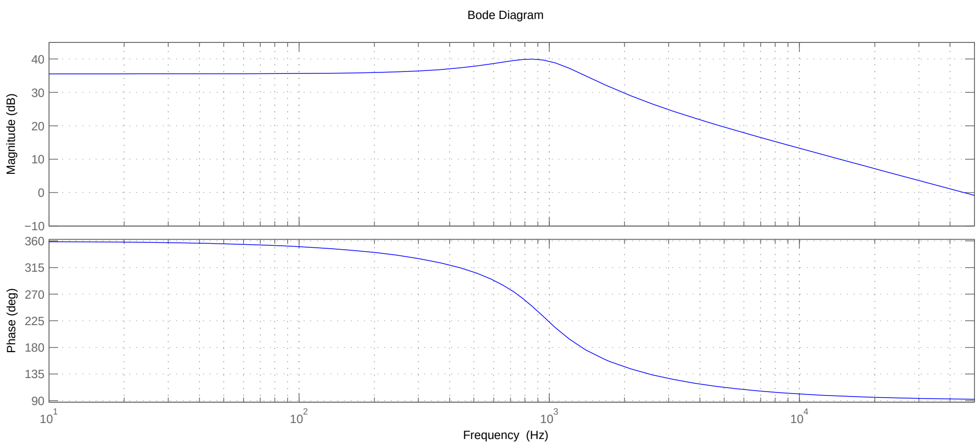

Figure 3.2 : Analytically calculated control to output transfer function of tested boost converter.

In order to test the cross correlation method, the model show in Fig. 3.3 is built MATLAB Simulink environment. As it is seen in the figure, a white noise signal is sampled and applied as a perturbation to the control signal of a converter. The perturbation signal is saved to workspace with variable "u".

At the output of the converter, the output voltage signal is run through a digitization block to simulate the behaviour of analog-to-digital converters (ADCs) and the digitized values are saved to workspace. Both duty cycle perturbation and converter voltage output signals are sampled using the same clock and sample and hold blocks. Moreover, the switching frequency of the converter and sampling rate are 100 kHz. The perturbation frequency is also 100 kHz, meaning that a perturbation to the duty cycle command is performed in each switching period.

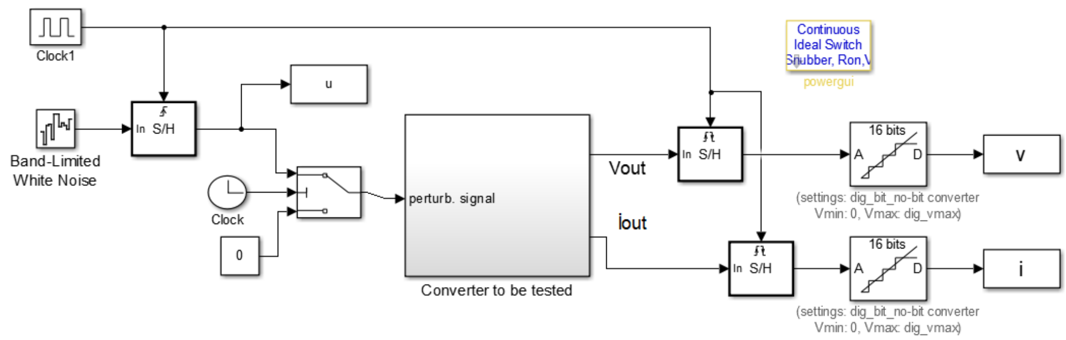

Figure 3.3 : The general overview of the Matlab-Simulink Model.

The auto-correlation of the input signal, which corresponds to the duty cycle perturbation signal, R_{uu}, and cross-correlation of input and output signal, which is the converter output voltage, R_{uv}, are illustrated in Fig. 3.4. In the ideal case the auto-correlation of the input signal should be a delta function, where the signal is equal to zero except the midpoint. However, it is impossible to generate a ideal white noise signal. Thus, R_{uu} is slightly different from the ideal case due to the non-zero values except the midpoint. This non-ideality causes the cross-correlation, R_{uv}, to be distorted, which alters the obtained transfer function.

In order to suppress the non-ideal parts of R_{uv}, it is determined to divide R_{uv} by R_{uu}, which would yield better results than dividing the cross-correlation with a constant, as mentioned in theoretical background section:

$$G_{vd}(j\omega) = \frac{FFT\{R_{uv}\}}{FFT\{R_{uu}\}} \tag{3.6}$$

The obtained transfer function is illustrated in Fig. 3.5. The result is very similar to the analytically calculated bode diagram. However, as it is seen in the figure, the obtained plot starts to diverge from the analytically calculated one at higher switching frequencies. This is due to fact that the pulse-width-modulation (PWM) block adds an extra transfer function since the PWM acts like a zero-order-hold.

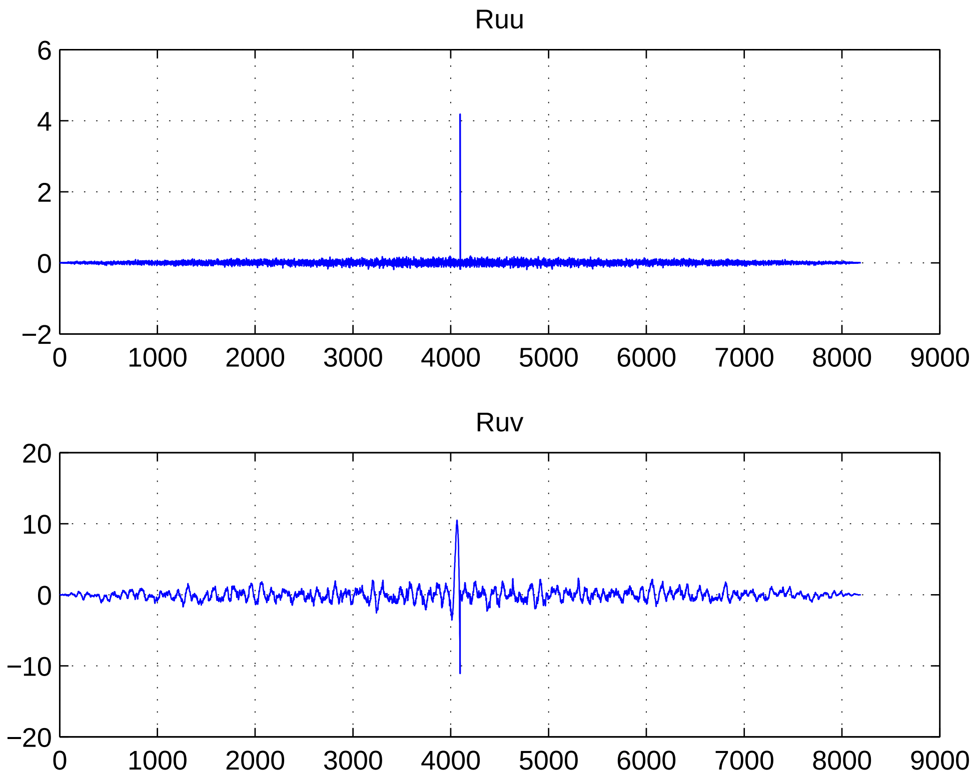

Figure 3.4 : Auto correlation of perturbation signal and cross-correlation of perturbation and output signal.

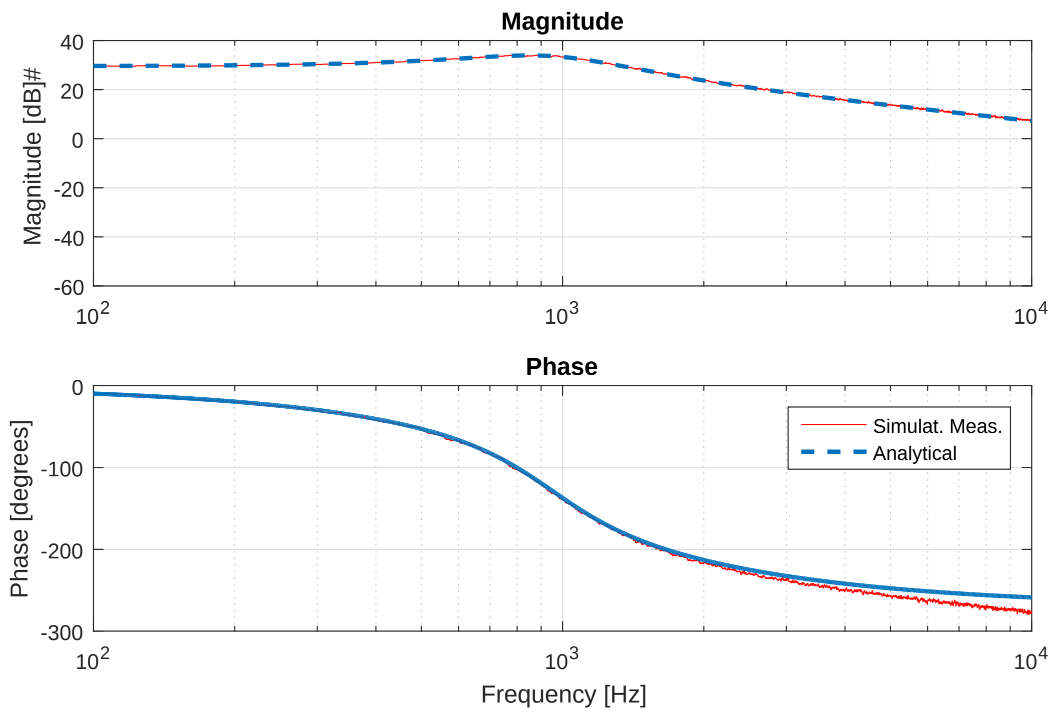

Figure 3.5 : Obtained bode diagram of boost converter by simulation.

3.2 Obtaining Circuit Impedance at Open-Loop Operation

For demonstrating the impedance identification capability of the approach, it is decided to perform the method to obtain the impedance of a basic passive filter network, as shown in Figure 3.6.

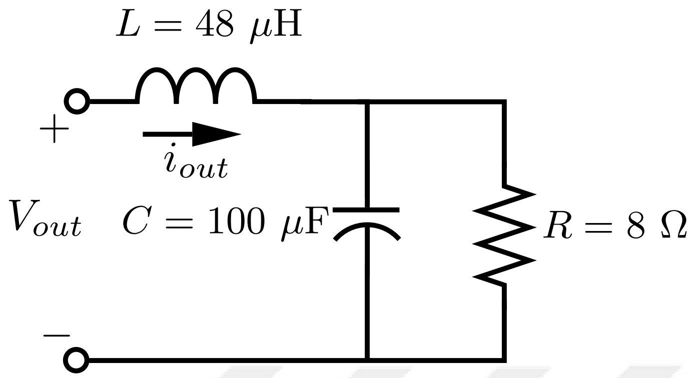

Figure 3.6 : The circuit to be tested.

The passive RLC network is connected at the output of the boost converter, and the simulation is run as shown in the previous section. However, this time both converter output voltage and current waveforms are recorded and they are used for identification of the impedance, as explained in the previous chapter. Similar to the previous case, where the converter cotrol to voltage output transfer function is identified, the switching frequency of the converter and sampling rate are 100 kHz.

The results of the simulation are illustrated in Fig. 3.7. As it can be seen, the simulation results are very similar to the analytically calculated transfer function of the passive RLC network. As observed in the previous simulation, the PWM caused some distortions at higher frequencies.

3.3 Obtaining Circuit Impedance at Closed-Loop Operation

The results demonstrated in the previous section are achieved under open loop operation of the converter. However, it is also of great interest whether similar results can be achieved under the closed loop operation of the converter, since it would mean that online impedance identification could be performed without interrupting the normal operation of the converter at all. Thus, it is decided to demonstrate the method with the addition of an feedback control in the simulation. The added feedback loop is illustrated in Figure 3.8.

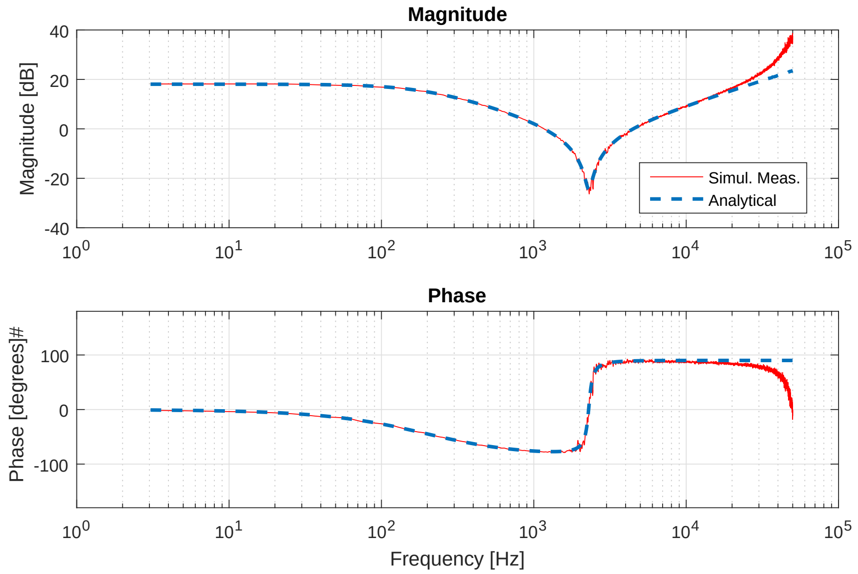

Figure 3.7 : Analytically calculated bode diagram of battery equivalent circuit.

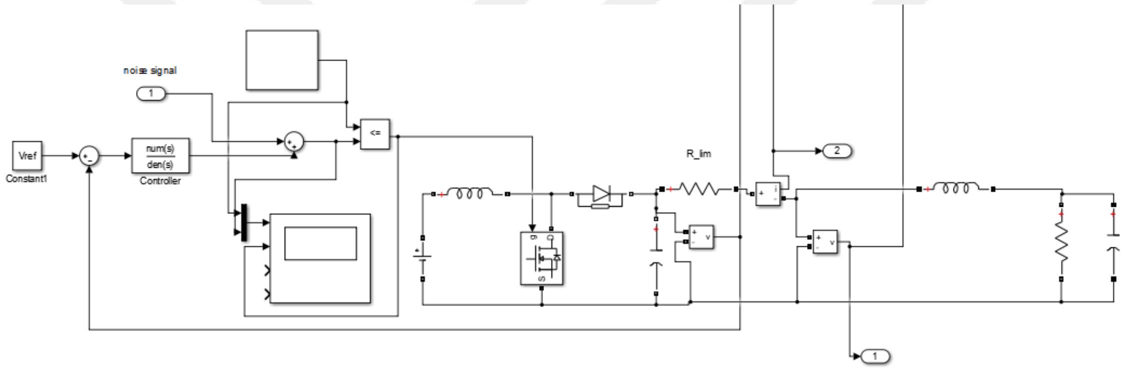

Figure 3.8 : Simulation model of the boost converter circuit with feedback control.

On the other hand, it should be noted that the closed loop controller has to be able to run the converter in a stable manner. Thus, a MATLAB script automatically designing a stable controller is written. The script calculates the control-to-output voltage transfer function, G_{vd} of the boost converter that has the RLC filter circuit at the output and designs a feedback controller according to the required phase margin.

The control to output transfer functions of the simulated converter and the designed controller are illustrated in Figure 3.9 and 3.10.

The said script also calculates the transfer function of the digitally controlled boost converter, G_{vdz}, since it would deviate from the ideal transfer function, which in return could result in poor performance of the controller if it is designed according to the continuous time model.

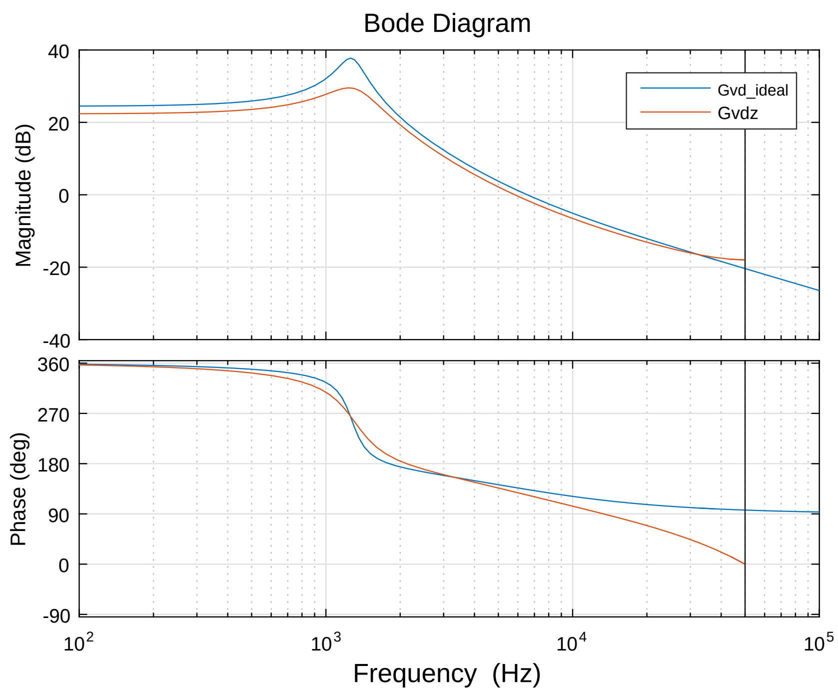

Figure 3.9 : Control-to-output voltage transfer function (Gvd) of the boost converter with ideal resistive load (blue line) and with RLC filter load (red line).

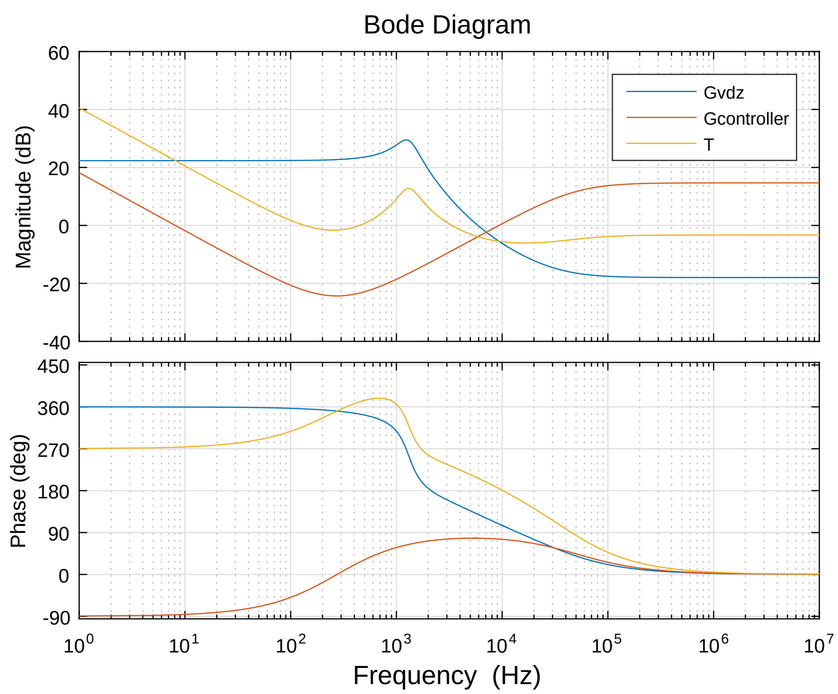

Figure 3.10 : Transfer function of the designed controller (yellow line) and the resulting forward loop gain (blue line).

Before running the test for identifying the impedance of the RLC network, the operation of the converter under closed loop is confirmed to be stable. The results of the identification process under closed loop operation are illustrated in Figure 3.11.

As it can be seen in the figure, the method was able to identify the transfer function of the RLC filter circuit at the output, even under closed-loop operation.

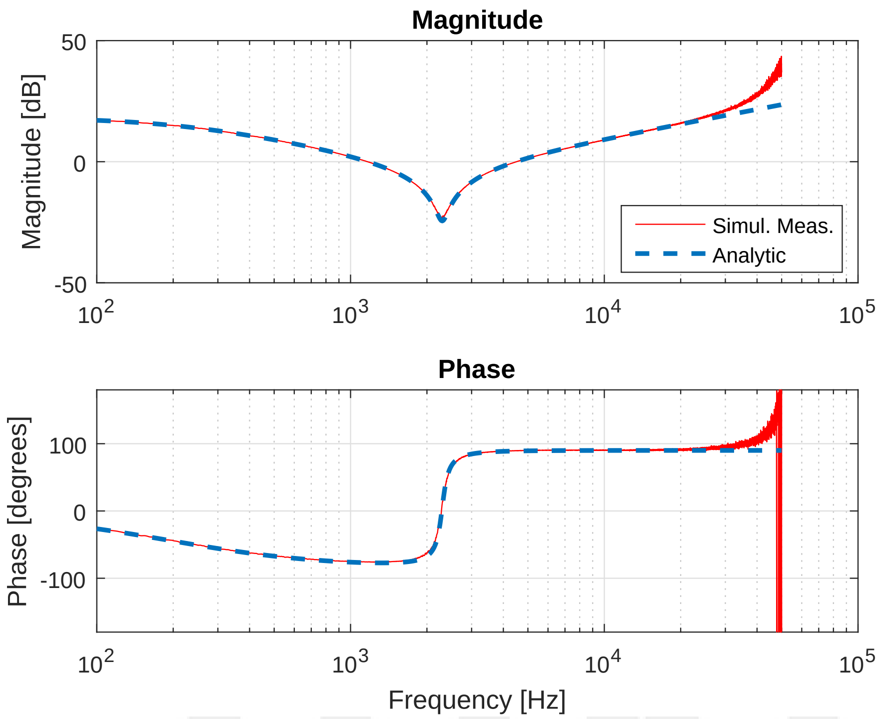

Figure 3.11 : Simulation results for the RLC filter at the input (red dashed line) compared to analytically calculated RLC circuit impedance (blue line).

3.4 Concluding Remarks

The operations principles of the proposed approach are successfully verified by the simulations studies that are presented in this chapter. As it can be seen from the results, the measurements by the proposed method substantially match the analytical calculations of the converter transfer functions and the tested passive RLC networks. Furthermore, some conditions regarding to the real experiments, such as the sampling rate and quantization of measured waveforms by the ADCs, that might expose challenges are implemented within the simulations so that their effects are already have been accounted for.

Additionally, it is also shown that the proposed approach is capable of having correct measurements even under the closed loop operation of the DC-DC converter. This, enables a true online impedance measurement capability since the feedback loop of the converter does not need to be broken and the converter is able to continue the operation.

However, the simulations did not cover the dynamic behavior of the batteries, which may effect the measurements in the experiments. Thus, some improvements for the method are provided in the "Pre- and Post-Processing" Section of the previous chapter. Moreover, controller implementation of the PWM perturbation will be given in the next chapter, which is also a crucial part of the proposed approach.

Another important part of the study is also correct capturing of the battery voltage and current waveforms. This issue is addressed in the next chapter, where the measurement setup and a specialized circuit for conditioning the waveforms are explained in detail.

4. TEST SYSTEM DEVELOPMENT

In this section, the test setup that is utilized for verifying the theoretical background and simulation studies is explained in detail. The tests are performed on a digitally controlled boost converter that operates as a battery charger The test waveforms are recorded with a data acquisition hardware stored in a computer and analyzed via MATLAB.

4.1 Test Bench

The general overview of the test bench where the experiments are conducted is shown in Figure 4.1. The test bench is comprised of an FPGA controlled boost converter that is charging a commercial lead acid battery, the Yuasa NP7-12, which is rated at 12 Volts and 7 Ampere Hours. The boost converter is supplied by a regular bench top DC power supply. The FPGA is utilized for precisely implementing the duty cycle perturbation into the PWM signal of the boost converter.

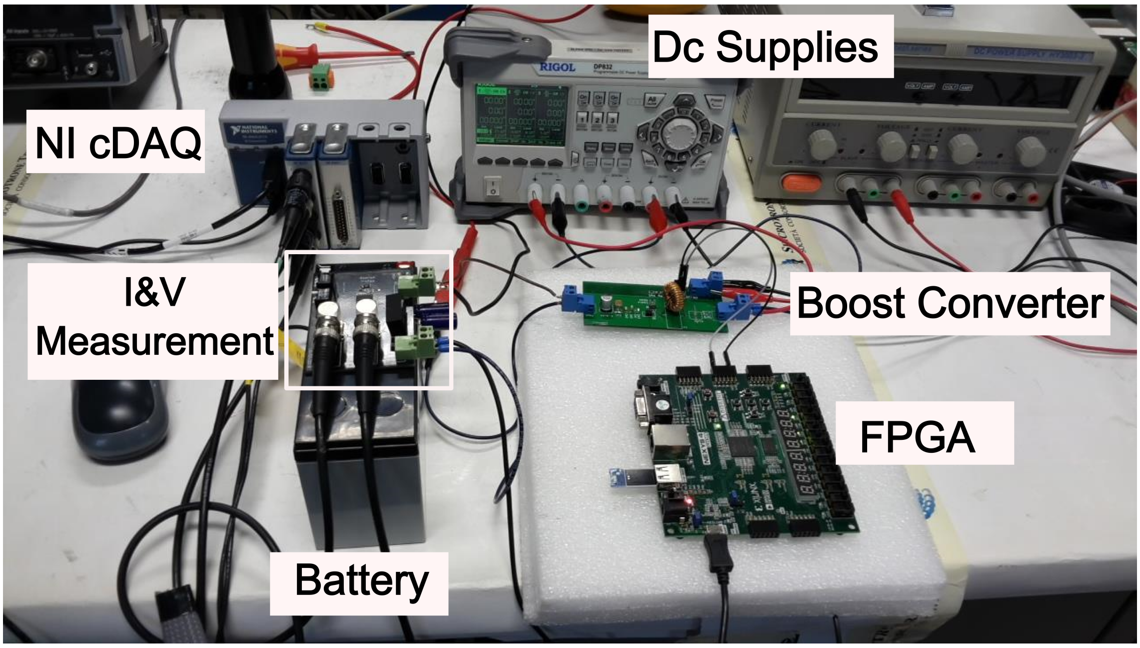

Figure 4.1 : Final test bench setup.

A battery voltage and current measurement circuit is also designed for conditioning the battery voltage and current waveforms for recording. The battery voltage and current waveforms during the testing of the battery are recorded with a data acquisition hardware. The recorded waveforms are transferred to a computer for analysis, where they are processed with MATLAB.

4.2 Data Acquisition Hardware

For recording the waveforms during the testing of the battery, it is decided the use one of the modular data acquisition systems of National Instruments (NI), namely the NI cDAQ. This system provides a modular platform, where different types of modules depending on the need can be installed on a chassis board, which handles all the communication between the computer and the data acquisition hardware.

For the purpose of this thesis, it is decided to utilize the NI cDAQ-9174 chassis, shown in Figure 4.2(a), which has four slots for mounting different types of modules such as analog input/output modules, digital input/output modules, communication modules and relay modules.

(a)

(b)

Figure 4.2 : (a) NI CDAQ-9174 chassis and (b) various NI CDAQ compatible modules.

This data acquisition system is used for recording four voltage waveforms; battery voltage, battery current, test start signal and PWM signal of the converter. Moreover, it is also recommended to sample the waveforms simultaneously so that no additional delay function is introduced to the results. Thus, it has been decided to utilize NI 9222 voltage input module, shown mounted in Figure 4.3.

Figure 4.3 : Mounted NI CDAQ modules.

NI 9222 module can be mounted on a single slot of the NI cDAQ-9174 chassis. It is capable of simultaneously sampling four analog inputs between +10 and -10 Volts. In contrast to more common data logging hardware, it can sample all four channels at the same time each with maximal 500 kSamples/second. Furthermore, the sampling frequency is independent of the channels being used. The resolution of each channel is 16 bits. The Matlab scripts for data acquisition and processing is given in Appendix C.1 - C.4.

4.3 Boost Converter Design

A 30 Watt boost converter that is capable to supply up to 15 Volts, 2 Amperes output is also designed to be utilized as a battery charger. The converter comprises a silicon MOSFET and an optocoupler at the gate driver for protecting the digital controller.

The converter is designed to operate at a switching frequency of 20 kHz. The assembled printed circuit board of the boost converter is shown in Figure 4.4. The layout of the circuit was designed carefully and capacitors, comprised of electrolytic capacitors and multi layer ceramic capactiors (MLCC) of high quality was used for correcting the waveforms.

Figure 4.4 : The produced PCB of the designed converter.

4.4 FPGA-Based Digital Controller Design

As explained in the theoretical background, the cross-correlation method utilized in this thesis relies on the perturbations into the duty cycle of the PWM signal, as shown in 4.5, applied to the boost converter. Although the method can be implemented in most of the common digital controllers, such as DSPs or PIC32 based platforms, these devices do not have a dedicated hardware for applying perturbations on the PWM signal.

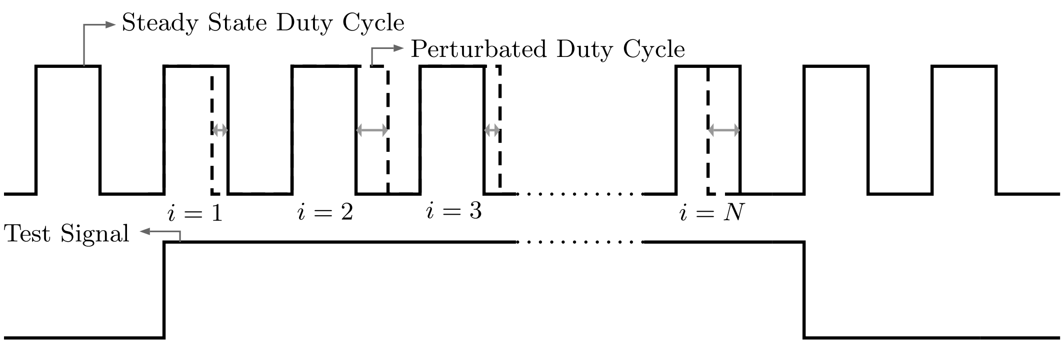

Figure 4.5 : The operation of duty cycle perturbation.

Consequently, although these controllers are quite fast in the sense that run at high clock rates, they may not be able to apply the duty cycle as precise as required. For example, during testing of the battery, the controller is required to change the duty cycle of the boost converter at the same rate with the switching frequency, 20 kHz in this case.

However, it takes some time for the controller to change the relevant registers regarding to the PWM signal. Moreover, since the program of the above mentioned controllers are generally written in high level languages, the commands are run in sequence. Therefore, the software may be doing another operation, whereas it may needed to perform the perturbation operation. Thus, the quality of the applied perturbation signal may deviate from the originally anticipated one, which in return could decrease the quality of the results.

For these reasons, it is decided to utilize an FPGA as the controller of the boost converter to be able to precisely control the perturbation signal. FPGAs consists of thousands of logic blocks that can be programmed to perform a specific task. So, a programmed FPGA is actually an integrated digital circuit that can be reconfigured. FPGAs offer a lot of flexibility with the compromise of programming complexity. In this context, it is decided to utilize a Digilent FPGA platform, the Nexys 4 DDR that is shown in Figure 4.6. The block diagram of the designed PWM module is shown in Fig. 4.9.

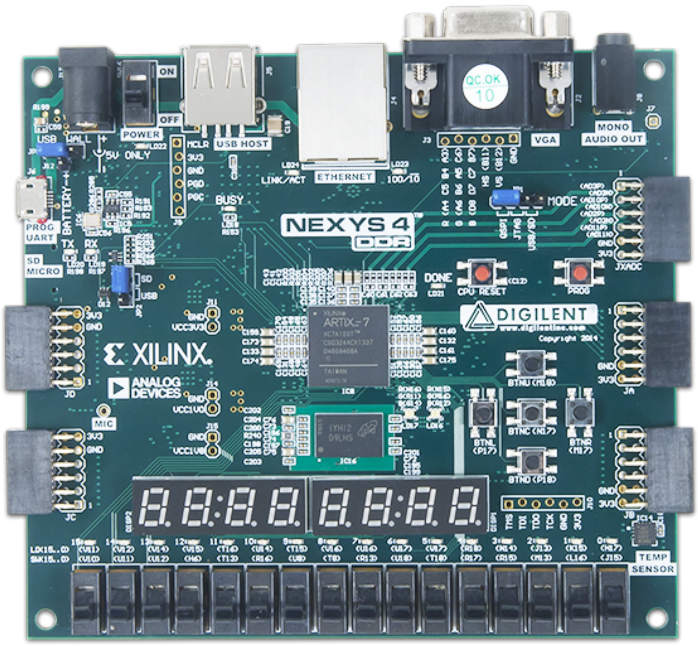

Figure 4.6 : NEXYS 4 DDR platform by Digilent Inc. utilizing an ARTIX-7 FPGA.

The FPGA platform is programmed using VHDL (Very high speed integrated circuit Hardware Description Language) programming language. A PWM module that is able to precisely apply the required perturbation signal is written in VHDL.

The PWM module comprised of two prescaler submodules, a counter submodule, a perturbation submodule and finally a PWM generator submodule. The prescaler submodules are clock dividers that are used to generate the base pulse signals at PWM frequency, f_{sw}, and the perturbation frequency, f_p, which is the rate at which the perturbation data is applied to the PWM signal. The implemented PWM module is represented as given by Fig. 4.7 in Vivado environment.

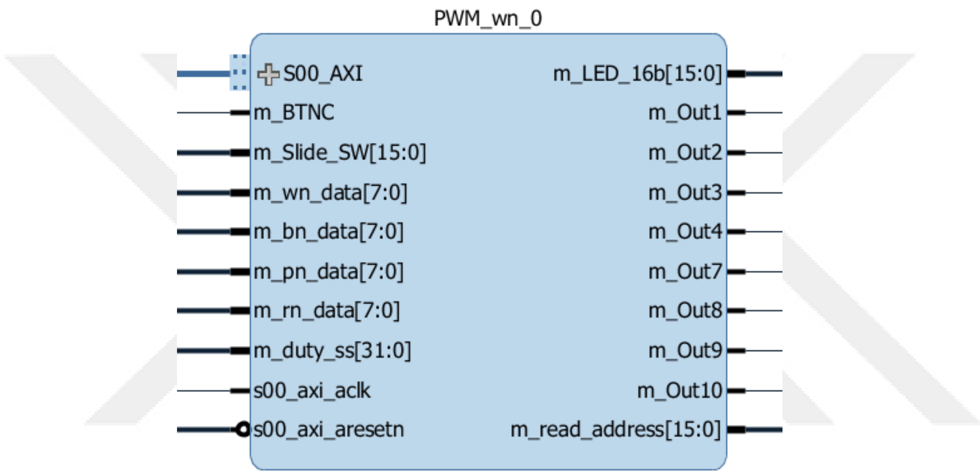

Figure 4.7 : The block design of the designed PWM module.

The process performed by the perturbation submodule of the PWM module is illustrated in 4.8. This submodule firstly checks the states of the switches on the Nexys 4 DDR platform for interfacing the PWM module with outside world, so that some properties of the applied signal can be changed by adjusting the position of switches provided on the board. Moreover, the start signal for performing the perturbation process is also received in this submodule. If it is detected that the start module on the FPGA platform is pressed, a debouncing procedure is performed in order to filtering out glitches. After that a test start signal is generated for starting the perturbation process, wherein at each PWM cycle the corresponding perturbation amount from the perturbation signal data is added to the duty cycle input of the PWM generator.

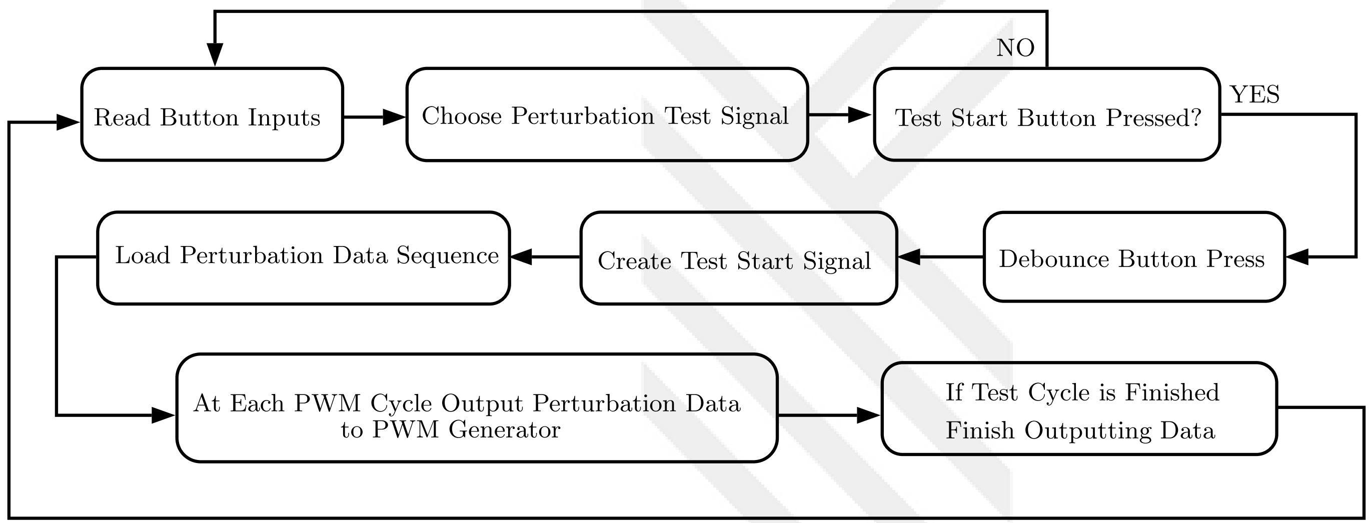

Figure 4.8 : Flow-chart of the perturbation submodule.

The PWM module also sets the start and stop numbers for the counter submodule, which counts each pulse of the main clock of the system that is set to 100 MHz. The counter submodule resets the count number after reaching the stop number that relates to the required switching frequency.

Furthermore, the counter submodule is also designed to produce different types of PWM modulations, such as trailing edge, leading edge and centered pulses. These different types of PWM modulation may be requested by changing the corresponding register.

Finally, the PWM generator submodule, creates the PWM signal depending on the defined duty cycle. The written VHDL codes are given in Appendix A.1 - A.5. The designed module is interfaced to the FPGA system, as illustrated by the simplified general overview of the final FPGA block design is illustrated in Fig. 4.10, whereas the complete overview of the final FPGA block design is given in Appendix B.1. The FPGA is programmed in Vivado 2016.4, which is the official development software offered for Xilinx FPGAs.

As it can be seen from the figure, the final design utilizes a Microblaze module and it's peripherals that is provided in the library of Vivado. The Microblaze module offers a lot of flexibility, since it is soft-core microprocessor, imitating the capabilities of a real processor. Moreover, an XADC module, which is also provided in Vivado library, is also used to be able to read the analogue inputs of the FPGA platform, enabling to create a feedback loop for the voltage or current control mode.

It is also worth mentioning that a PID module written in C++ was implemented by using Vivado HLS, which is a software offered by Xilinx to convert C++ programs into VHDL or Verilog programs that can be interfaced to the rest of the FPGA design. This way, the PID program will be included in as a hardware component of the FPGA.

As this concludes the hardware side design of the FPGA module, what further remains is to write a simple program that will be ran on the soft-core MicroBlaze CPU for calling some functions, such as initializing the XADC module, and setting up the registers.

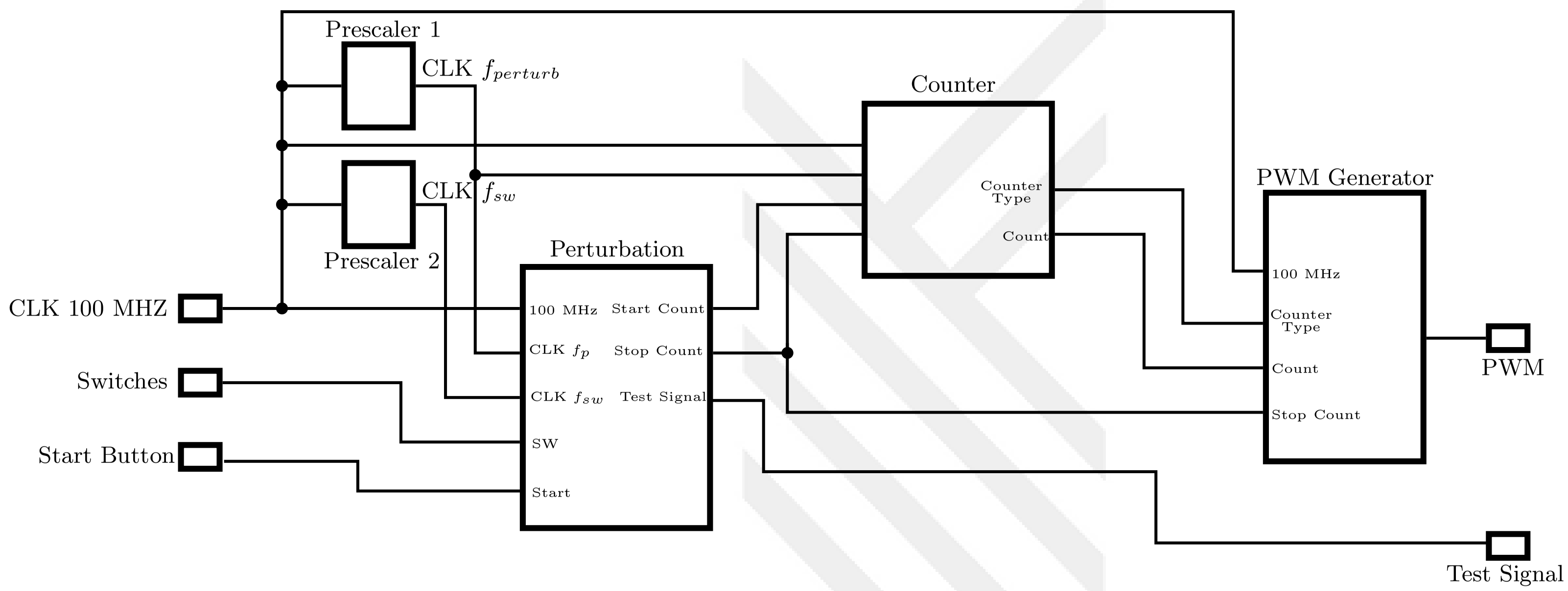

Figure 4.9 : Implementation of PWM generation and duty cycle perturbation.

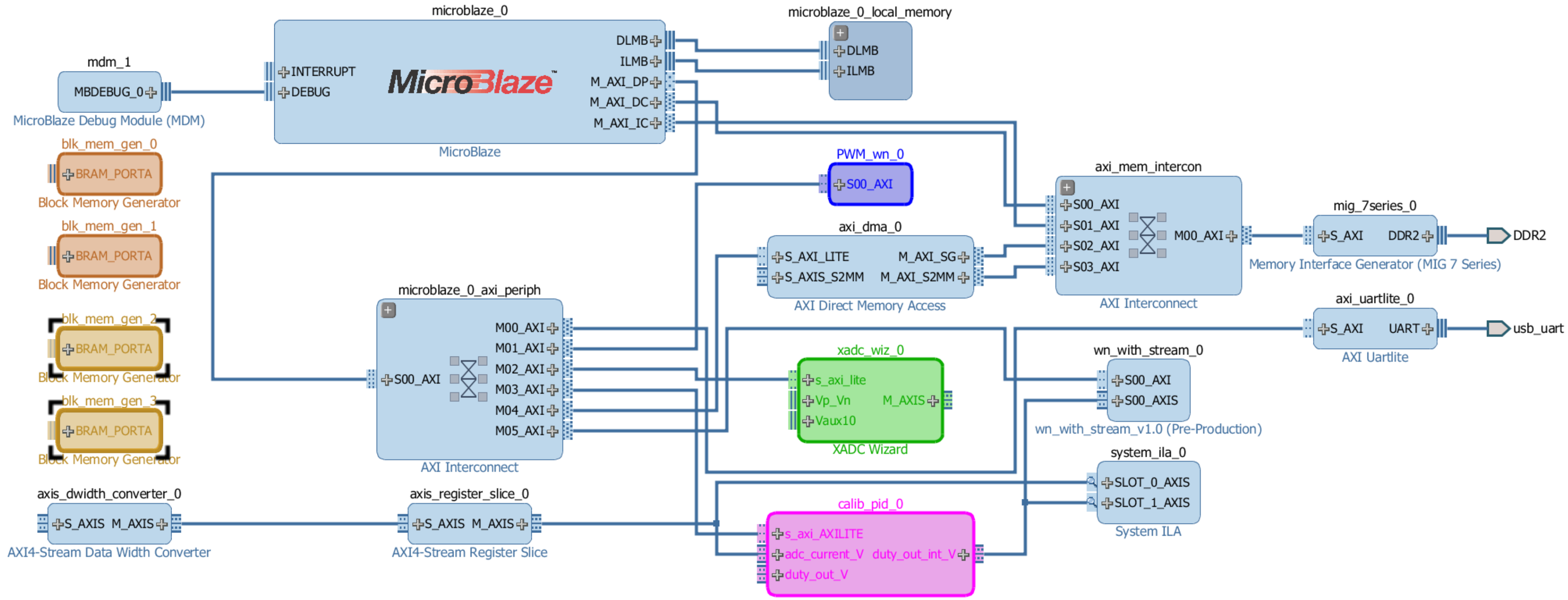

Figure 4.10 : Simplified overview of the implemented block design on the FPGA.

4.5 Current and Voltage Measurement Circuit Design

As mentioned earlier, the waveforms are recorded with a voltage input ADC of ±10 Volts. Thus it is required to convert the current waveforms into voltage waveforms. Moreover, since the tested battery is rated at 12 Volts, the battery voltage waveforms have to be scaled to fit within the acceptable voltage range of the data acquisition equipment. For this purpose, a current and voltage measurement circuit is designed. The designed circuit utilizes a two channel programmable-gain amplifier, namely the THS7002 of Texas Instruments (TI). The block diagram of this high bandwidth amplifier is given in Figure 4.11.

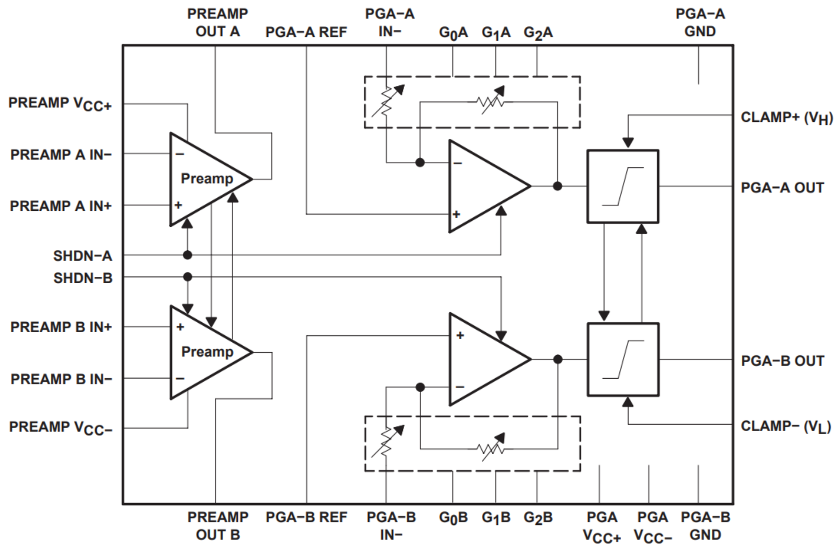

Figure 4.11 : Block diagram of THS7002.

For confirming the behaviour of the designed circuit, the circuit is simulated using circuit models offered by the manufacturer in the SPICE-based analogue simulation program of TI, TINA-TI. The schematic of the designed circuit is given in Figure 4.12. As illustrated in the figure, the channel for converting the current waveform into voltage waveform includes a low inductance shunt resistor of 100 $m\Omega$ for being able to correctly measure the waveform even at high frequencies. The voltage measurement points are connected in a differential manner to the pre-amplification stage of the amplifier. Moreover, two sets of three slide switches are provided on the board for being able to program the gain of the amplifier so that the designed circuit is quite flexible to be used with other component which may require lower or higher gains.

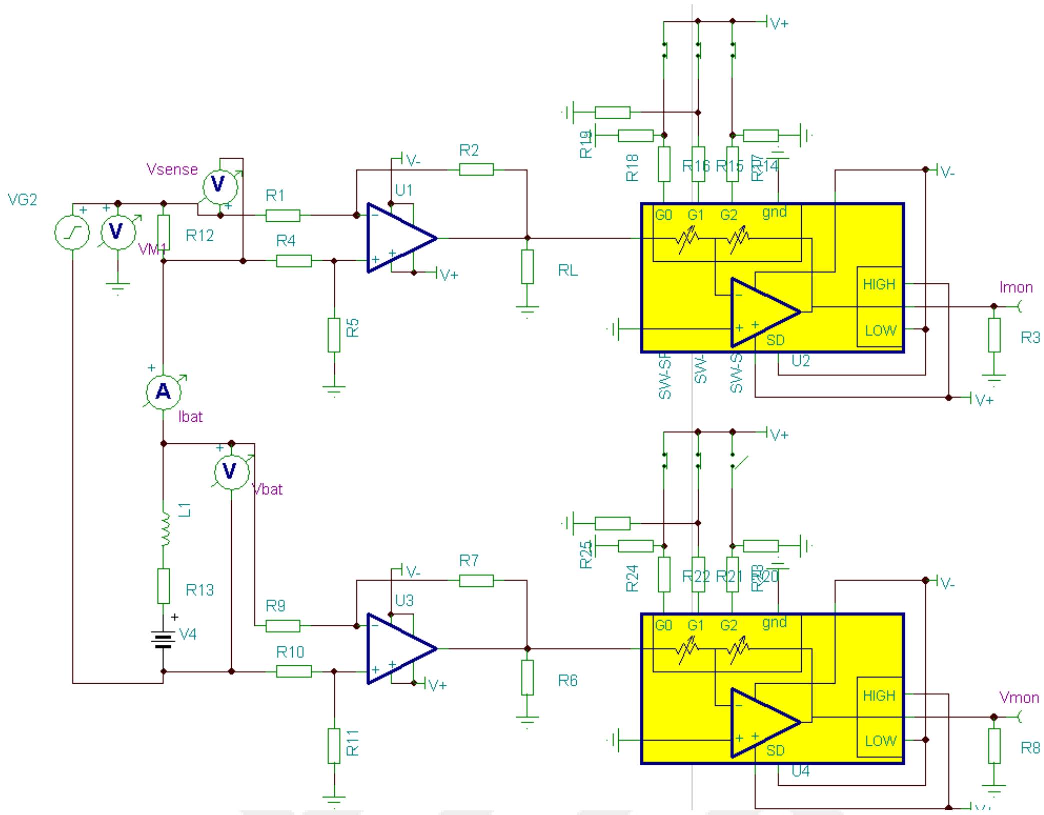

Figure 4.12 : Simulated circuit in TINA-TI.

The PCB layout of the designed measurement circuit is demonstrated in Figures 4.13 and 4.14. The PCB is designed to be fit directly to the battery terminals, so that the parasitic effects are minimized. Moreover, the outputs are designed as regular BNC connectors as to improve the connectivity. This way, the readings of the circuit can be directly interfaced to an oscilloscope or to the data acquisition unit.

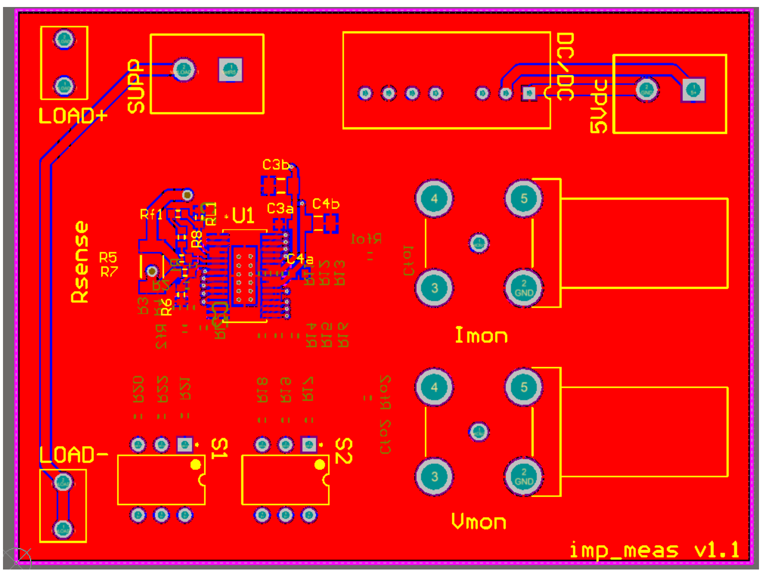

Figure 4.13 : The PCB layouts of the designed measurement circuit in 2D view.

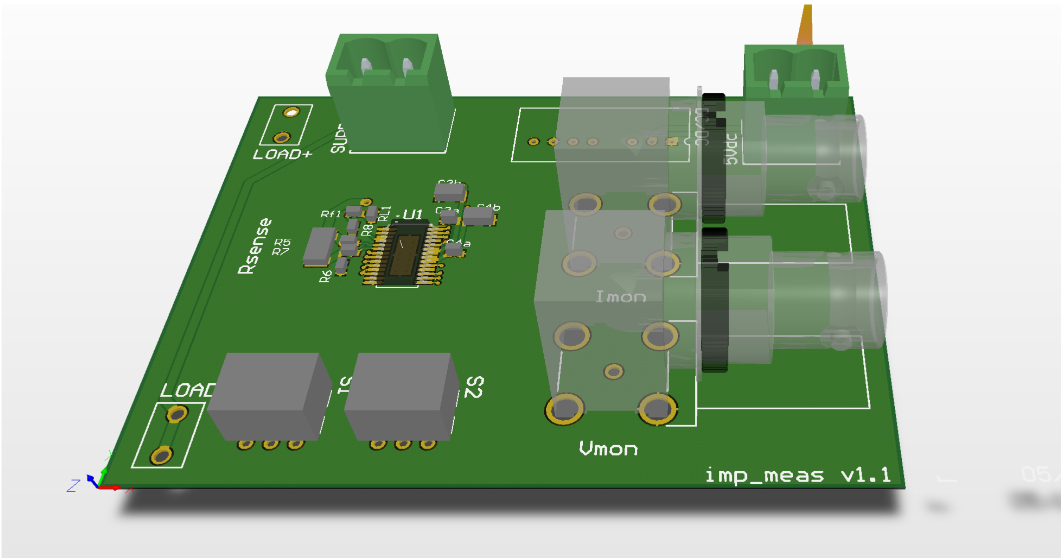

Figure 4.14 : The PCB layouts of the designed measurement circuit in 3D view

4.6 Testing Process

Here, a general overview of the testing process is also included in this section. As illustrated in Figure 4.15, first, a perturbation data is generated based on a white noise sequence in MATLAB environment. The generated perturbation data is then pre-processed for reconditioning of the data to be more suitable for battery tests, such as generating perturbation signals with other noise colours. This, pre-processed data is then saved to the FPGA controller, where the same perturbation data will be used for all the tests.

When a test request is received during normal operation of the boost converter, the FPGA applies perturbation to the duty cycle of the converter. The current and voltage waveforms during the test are then recorded via NI cDAQ module, and transferred to MATLAB for the impedance calculation. For improving the calculations, a post-processing is performed for smoothing out the impedance diagrams.

Lastly, this data is then used for fitting the measured battery impedance to a suitable battery equivalent electrical model, from which electrical parameters of the model can be extracted.

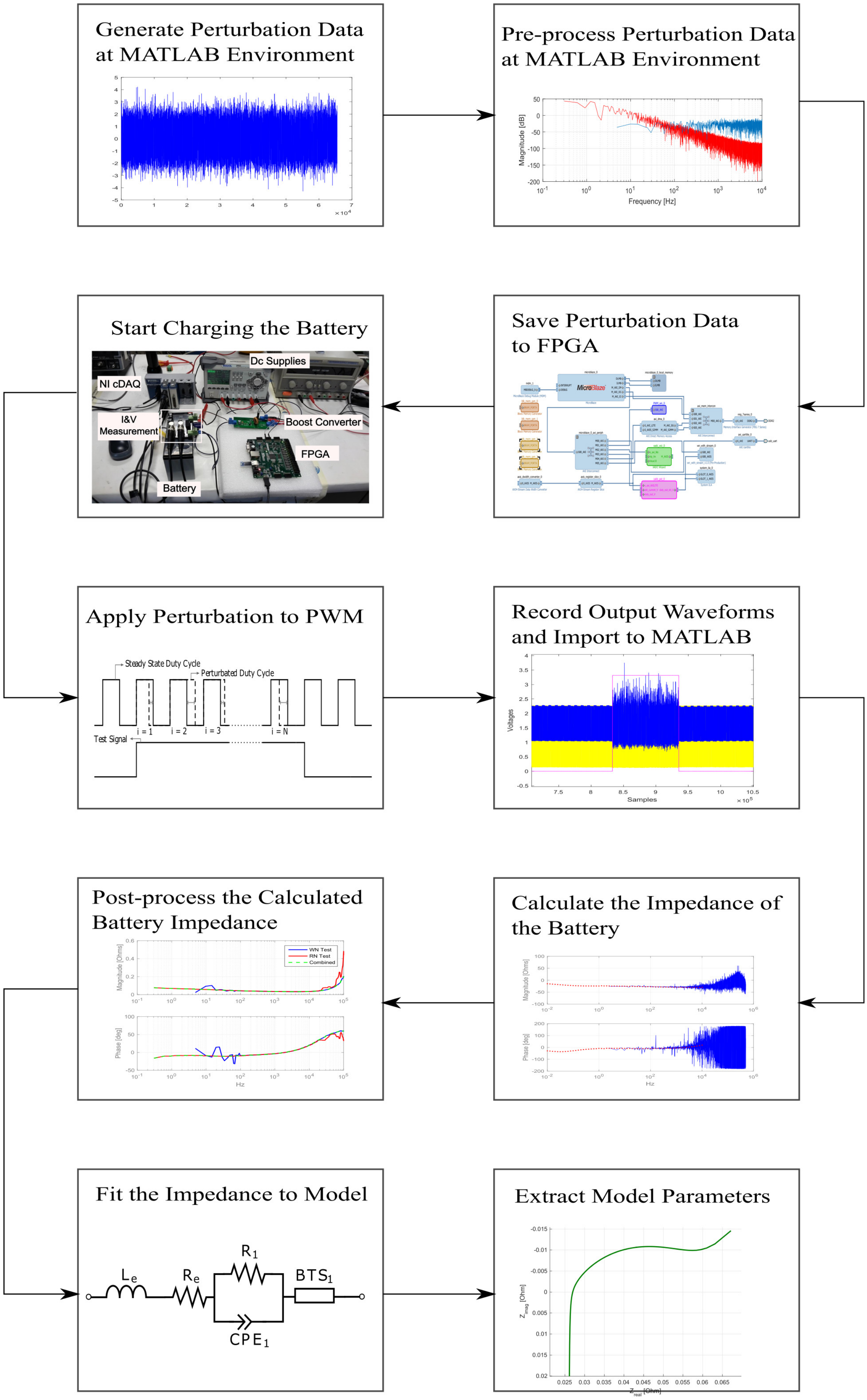

Figure 4.15 : General overview of the testing process.

4.7 Concluding Remarks

In this chapter, the underlying reasons for selecting an FPGA based platform for the implementation of the approach is explained. Additionally, a detailed view of the designed controller software, which is able to apply perturbations to the duty cycle command of a switch mode converter, is presented. Further explanations on the selection of a data acquisition system are also presented. The provided explanations on this topic may guide the designers in the process of selecting components for practical implementations of the presented method. Finally, an exemplary circuit for voltage and current measurements is also provided.

5. EXPERIMENTAL STUDIES

In this chapter, the validity of the proposed approach is confirmed via experimental results. First, the method is tested on the RLC filter that was utilized as the device under test in the simulation studies. After that, several tests on a lead-acid battery for various SOC values are performed.

With regards to the battery tests, firstly it is shown how the duty cycle perturbation magnitude can be selected. After that, the battery at 50% SOC is tested for both open-loop and closed-loop operations. The results are compared with the reference measurements that are gathered for the same SOC value by a high accuracy commercial EIS measurement device, Gamry Reference 3000. The similarity of the results that are fetched by the proposed method and the reference device are compared in order to confirm the validity of the method and test setup.

Once the method has been proven to be valid as mentioned above, further tests for different SOC values, 75% and 25%, are performed in order to demonstrate that the proposed method can also be applied for a wide range of SOC.

As it is common practice, the results are presented in both Bode and Nyquist Diagrams, giving the opportunity to evaluate them in view of different point of views. Additionally, the measurements are then fitted to the battery model mentioned previously. These results are also presented in comparison with the measurements.

5.1 Experiment with RLC Filter

The first experiment is set up for measuring the impedance of the RLC filter that was simulated in previous chapters. The experiment is arranged in the same manner as in the simulation environment, where the RLC filter is connected at the output of the designed boost converter.

For this test, the perturbation signal was a 2^{14} long white noise signal, which was applied to the duty cycle command at 20 kHz.

In order to be able to confirm the measurements, the impedance of the same circuit was also measured by a high precision LCR-meter as the reference. The results are presented in Fig. 5.1.

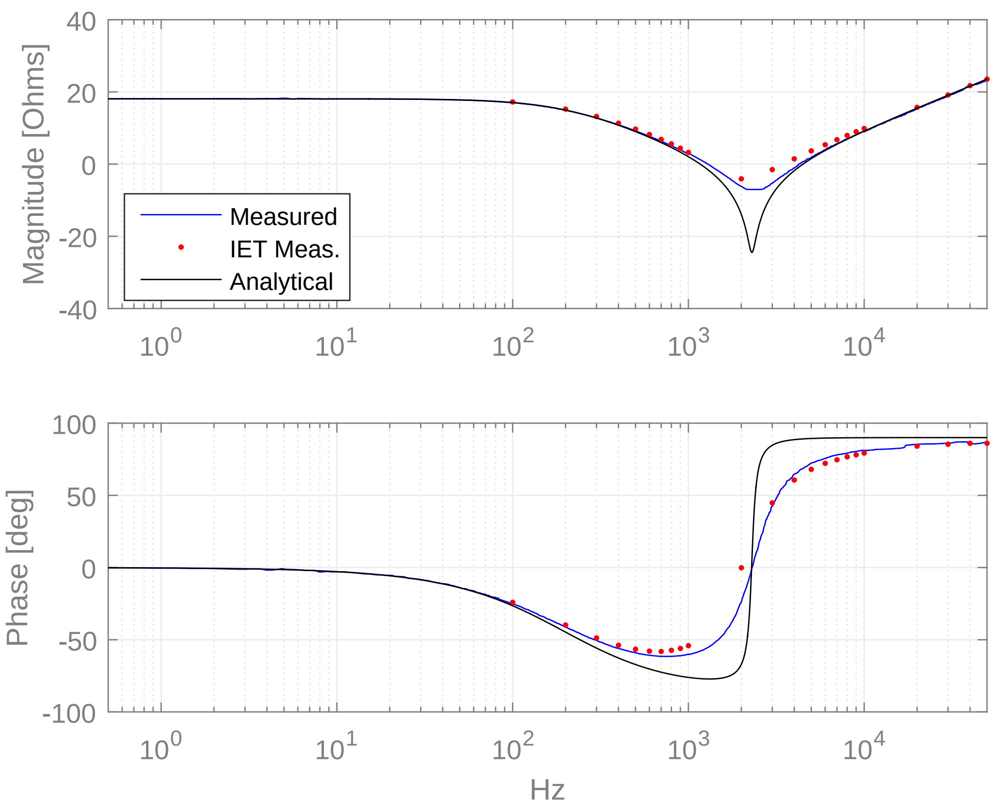

Figure 5.1 : Results for the RLC circuit impedance measurement by the proposed method (blue), by IET-1920 (red dots) and by analytical calculations (black).

As it can be seen from the figure, the results exhibit a good correlation between the reference measurements and the proposed method. Although, slight deviation between the reference measurement and the test results are observed around the resonance frequency of the filter, it is clear that both devices exhibit very similar results. The small deviation at resonance frequency may be attributed to different setups of the devices, wherein even the impedance of the connections may play a big role since the impedance of the filter is at it's lowest around this region. Thus, it may be concluded that the proposed approach is preforming as expected, similar to the simulations, for a passive load.

5.2 Experiments with Battery

The battery impedance measurement experiments are performed for various SOC. For each of the experiments, the battery under test is conditioned for measurement using the EN 50342-1 CENELEC standard: firstly, the battery is fully charged with a constant current of 1.75 Amperes up to 14.8 Volts and then it is discharged with a constant current of 0.7 Amperes for two and a half, five and seven and a half hours so that the SOC is determined to be 75%, 50% and 25%, respectively. Afterwards, the battery is left to a relaxation period until it the open circuit battery voltage is less than 1 mV/min before the measurements. Hereby it is pointed out that this procedure is strictly complied in order to create a routine for being able to repeat the tests under same conditions and for being able to make a fair comparison with the reference measurements.

For each experiment at a specific SOC, the impedance of the batteries are measured with two different tests, where the first test utilizes a white noise signal with a length of 2^{12} points applied to the duty cycle command and the second test utilizes a red noise signal with a length of 2^{16} points.

The boost converter is operated at switching frequency, f_{sw} of 20 kHz and the a perturbation is injected into the duty cycle command at each switching period, so that the perturbation frequency, f_p, is also 20 kHz.

For checking the validity of the results, a reference measurement was made by a commercially available high precision impedance analyzer, a Gamry Reference 3000 system, at 50% SOC, between 10 mHz and 10 kHz and this reference measurement is always compared with the measurement results at 50% SOC.

5.2.1 Determination of noise perturbation magnitude

One key parameter for the obtaining dataset of good quality is the magnitude of the perturbed noise data. If the perturbation magnitude is too small, then the data acquisition system might not be able to capture all the dynamics during the test, which in return would affect the measurements significantly. On the other hand, if the noise magnitude is too big, the linearity of the system might be compromised.

Thus, the choice of noise magnitude is a compromise between precision and system integrity. Consequently, it has been decided to perform tests with different noise magnitudes to find the better option.

Previously, it was mentioned that the literature suggests to limit the value of the applied noise data to be less than 10% of the maximum duty cycle, for enabling stability and linearity [36]. For this purpose, the magnitude of the designed noise data is set to be ± 4 % of the maximum duty cycle. Furthermore, a scaling coefficient for the perturbation data is also implemented in FPGA so that the proposed system can be tested under different perturbation magnitudes by multiplying the designed noise data by a the scale factor.

For this purpose, the battery was analysed by tests utilizing different WN magnitudes. As explained previously, a scaling factor that multiplies the WN signal was already implemented into the FPGA. In Fig. 5.2, the results for two WN tests with scaling factors of one and four, are presented.

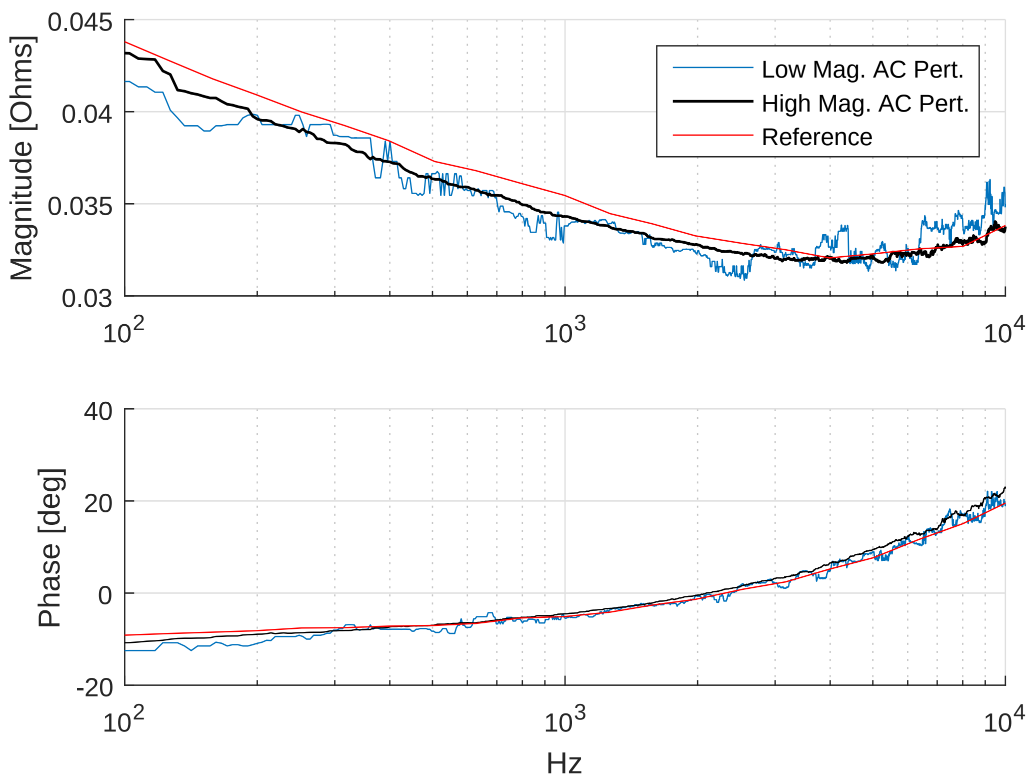

Figure 5.2 : Results of WN test for different noise excitation magnitude level, where blue and black curves have scaling factors of one and four, respectively.

For checking the measurement quality and displaying the difference of measurements with different perturbation magnitudes, it has been decided to perform Kramers-Kronig (KK) analysis, which is often used for EIS measurements. The KK-test provides a quick check for measurement quality and validity [60], [61]. It relies on the fact that the imaginary part of the impedance can be derived from real part and vice versa, given that the system is linear, time-invariant and causal. The derived results are then compared with the measurements and the difference is presented as residual plots. The residual plots for both tests are illustrated in Fig. 5.3.

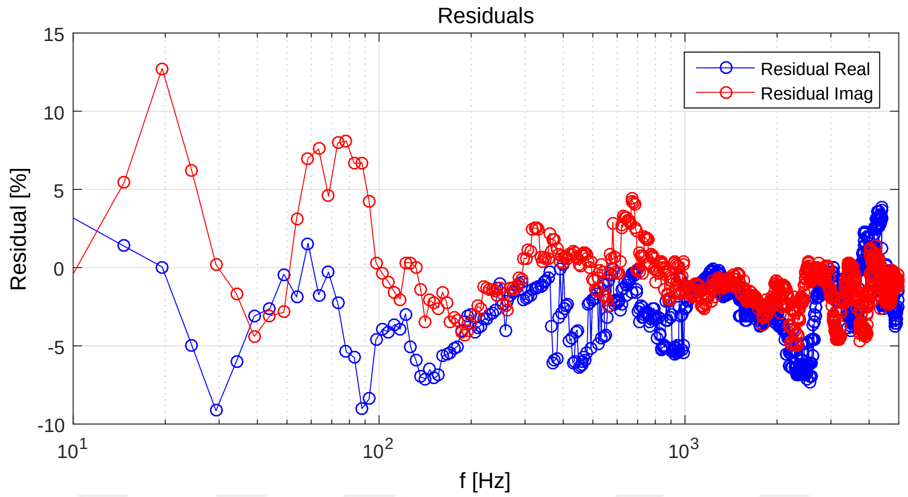

(a)

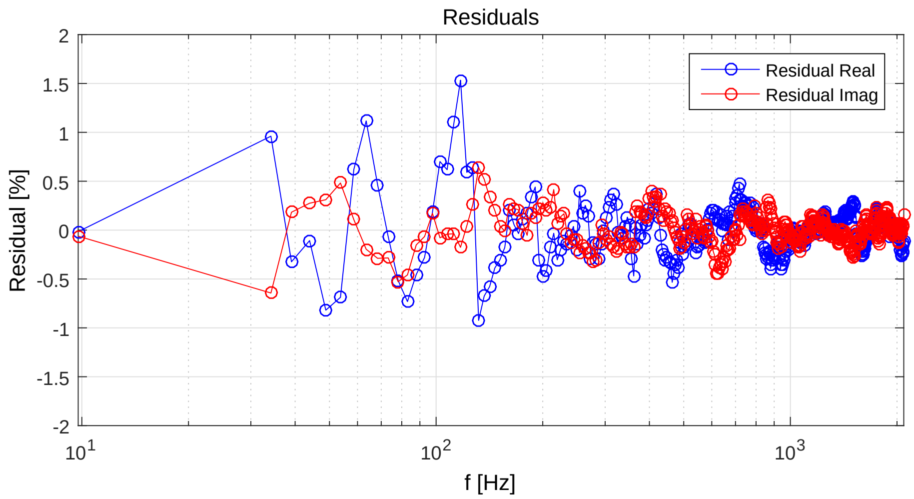

(b)

Figure 5.3 : Residual plots of Kramers-Kronig Analysis for the tests with the perturbation scale of (a) one (b) four.

As it can be seen both from Fig. 5.2 and Fig. 5.3(a) and Fig. 5.3(b) the measurement with a scale factor of four (corresponding to a perturbation magnitude of $\mp 16\%$)

has provided much more reliable results, whereas the measurement with scale factor (corresponding to a perturbation magnitude of $\mp 4\%$) one yielded noisy results. Thus, it has been decided to proceed further with the scaling factor of four.

The corresponding battery voltage- and current waveform magnitudes over the whole frequency bandwidth are also illustrated in Fig. 5.4. It can be seen that, the noise perturbation causes really small excitation, especially on the voltage. Therefore, a data acquisition system with high resolution is necessary. Please also note the switching disturbance in both current and voltage waveforms at 20 kHz.

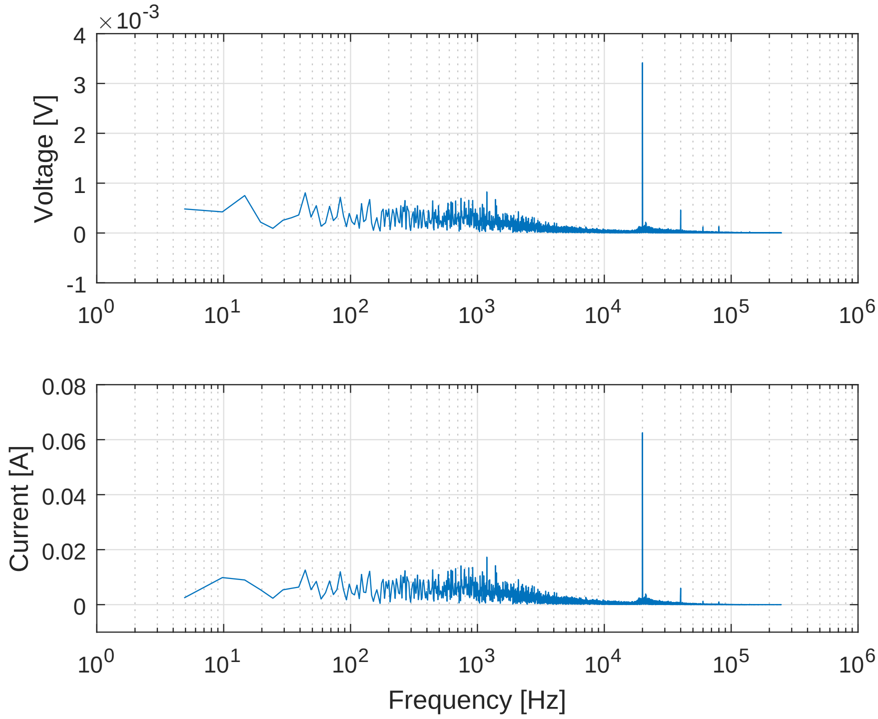

Figure 5.4 : Voltage and current waveforms during tests, where DC values are discarded.

Now that an appropriate perturbation magnitude has been selected, the tests for measuring the impedance of the battery may be performed.

5.2.2 Experiment 1: 50% SOC, open-loop operation

For assessing whether the closed loop controller of the boost converter is influencing the measurement, it is decided to test the battery under open-loop operation firstly. Fig. 5.5 illustrates the results of the test at 50% SOC under open-loop operation, presented in comparison with this reference measurement.

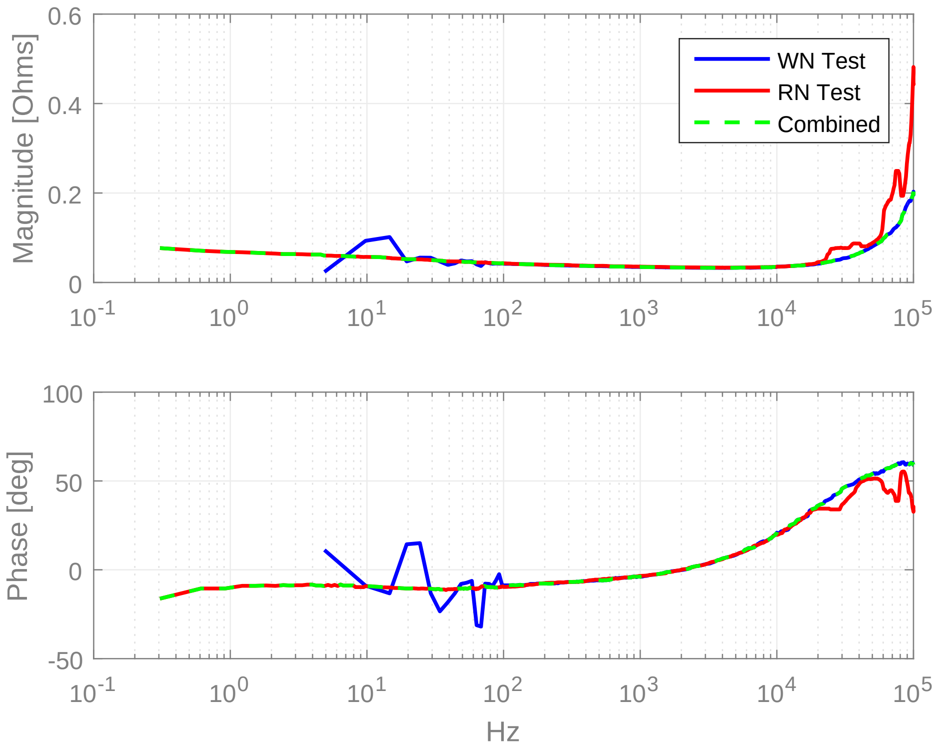

Figure 5.5 : Illustration of measurements at 50% SOC under open-loop operation for WN test (blue line), RN test (red line) and combination of both tests (green dashed line).

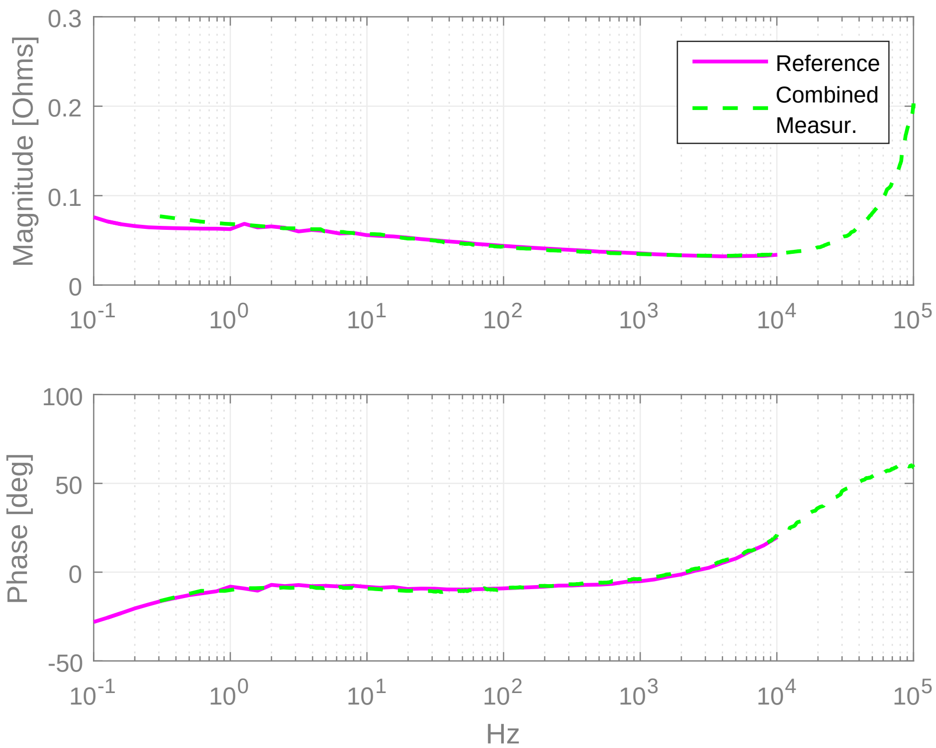

Figure 5.6 : Illustration of combined measurements (green dashed line) at 50% SOC under open-loop operation with comparison to reference measurements (pink line).

As it can be seen in Fig. 5.5 two tests are performed, one utilizing the white noise signal as the perturbation and the other using the blue noise signal. The results of both tests are then merged to obtain a wideband impedance spectra. The resulting measurement obtained by both tests are illustrated in comparison to the reference measurements in Fig. 5.6.

As elaborated earlier, the results are finally fitted to the equivalent electrical model. The model fitted curve, the battery impedance measurements and the reference measurements are then presented in comparison in Fig. 5.7.

Moreover, the model fitted results are also presented as a Nyquist Plot in Fig. 5.8 in order to assess the results from another point of view.

As it can be observed from both figures, the reference measurements and the battery impedance measurements under open-loop operation as proposed by this work show a high correlation. The only deviation is observed at the lower frequency end.

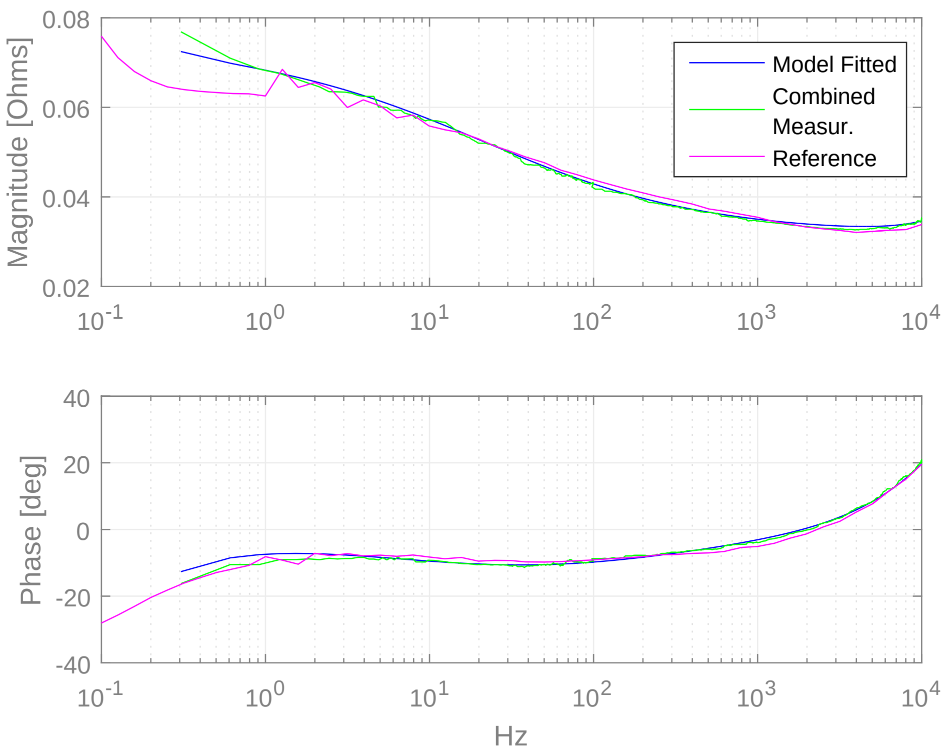

Figure 5.7 : Illustration of model fitted results (blue line) and combined measurements (green line) at 50% SOC under open-loop operation in comparison with reference measurement (pink line).

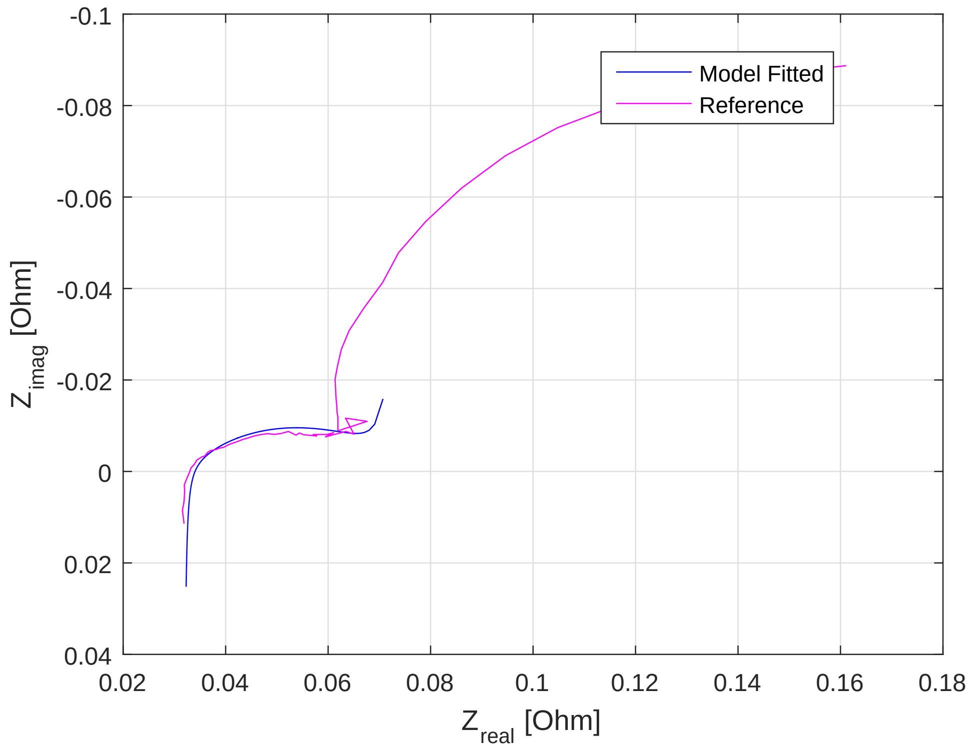

Figure 5.8 : Illustration Nyquist Plot for model fitted results at 50% SOC under open-loop operation with comparison to reference measurements.

5.2.3 Experiment 2: 50% SOC, closed-loop operation

Now that there is a good starting point for the open-loop operation results, the validity of the approach is to be confirmed under closed-loop operation too. The boost converter is set up to operate under current control, wherein the current is set to 0.75 Amperes.Moreover, the battery is reconditioned to be at 50% SOC again in order to be able to make a fair comparison. The results of the tests under closed-loop operation is presented in Fig. 5.9, where both the WN test, BN test and the combination of both tests are illustrated.

Fig. 5.10 provides a comparison of the reference measurement with the results obtained by the combination of WN and BN tests. Finally, the results are fitted to the equivalent battery model, which is illustrated in Fig. 5.11. Moreover, the model fitted results are also presented as a Nyquist Plot in Fig. 5.12, where the results from open-loop and closed-loop tests are compared with the reference measurements. As shown in open-loop tests, a high correlation of all the results are observed, whereas a small deviation from the reference measurements are observed for both the open-loop and the closed-loop tests.

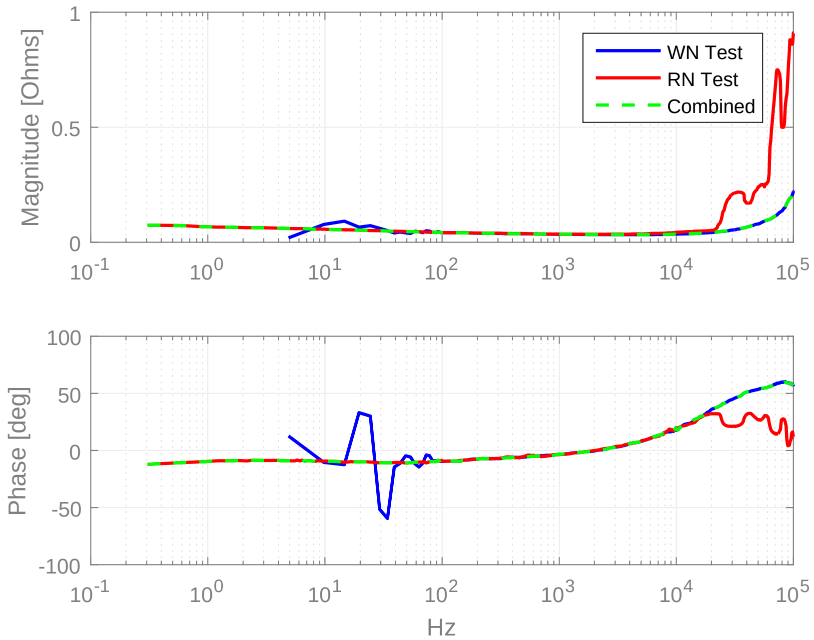

Figure 5.9 : Illustration of measurements at 50% SOC under closed-loop operation for WN test (blue line), RN test (red line) and combination of both tests (green dashed line).

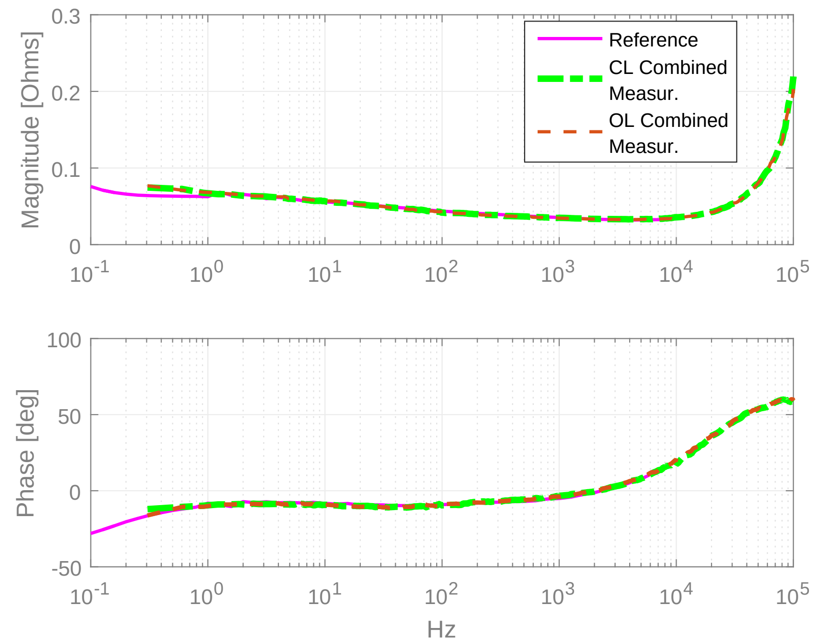

Figure 5.10 : Illustration of combined measurements at 50% SOC under closed-loop operation (green dashed line) and under open loop operation (red dashed line) with comparison to reference measurements (pink line).

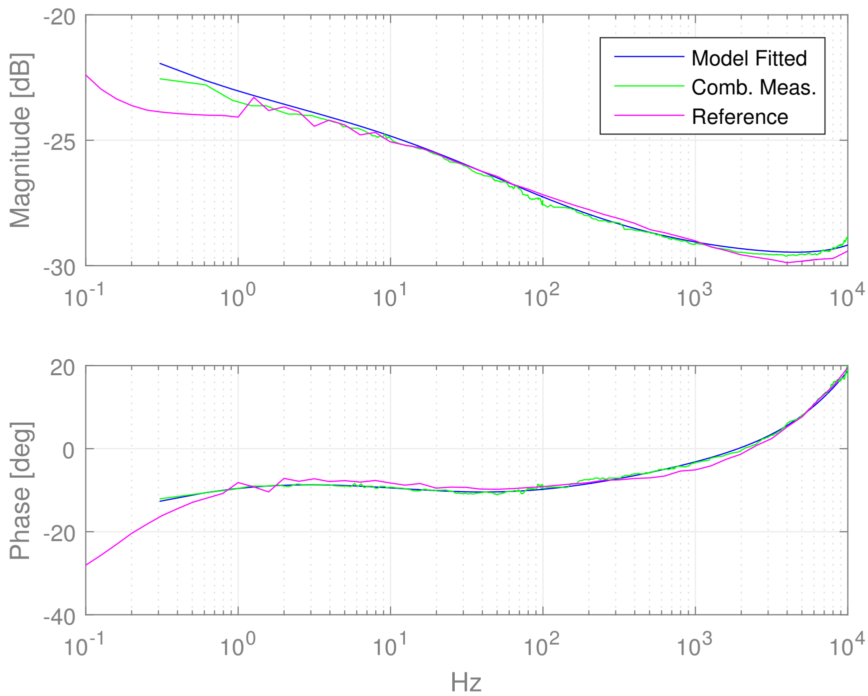

Figure 5.11 : Illustration of model fitted results (blue line) and combined measurements (green line) at 50% SOC under closed-loop operation in comparison with reference measurement (pink line).

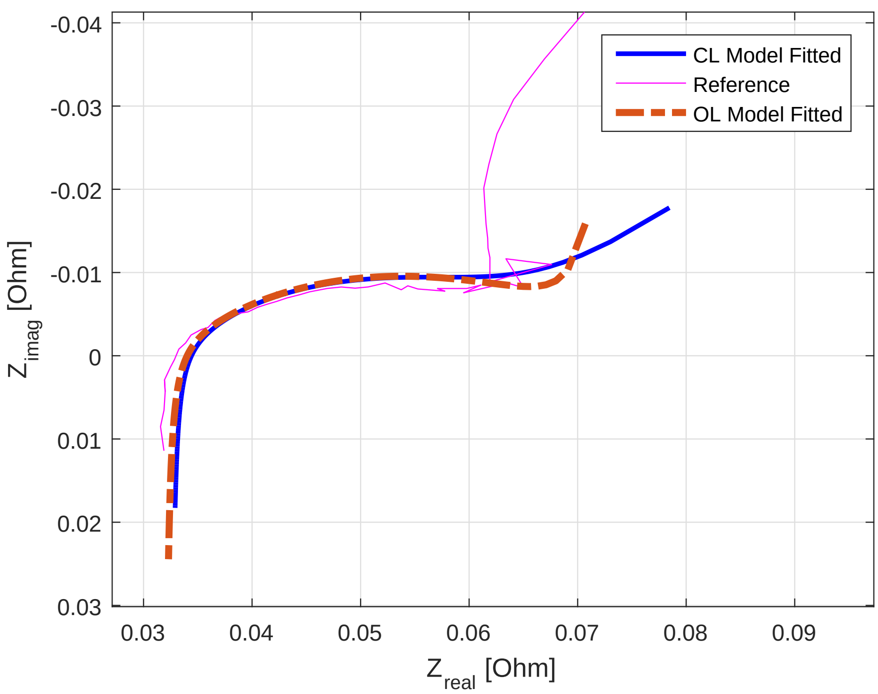

Figure 5.12 : Illustration Nyquist Plot for model fitted results at 50% SOC under open-loop operation (red dashed line) and under closed-loop operation (blue line) with compparison to reference measurement (pink line).

5.2.4 Experiment 3: 25% SOC, closed-loop operation

After confirming the validity of the approach under closed-loop operation of the converter, the proposed method will be tested for various SOC conditions as to prove the validity of the method even with different battery parameters. In this context, it is decided to perform EIS measurements at further SOC of 25% and 75%. The test results will be compared in the end to see the change of the impedance spectra of the battery.

Consequently, the battery is tested at 25% SOC and Fig. 5.13 illustrates the results of the test at 25% SOC under closed-loop operation. The results are then fitted to an equivalent model circuit, which is illustrated in Fig. 5.14. Finally, the model fitted results are also presented as a Nyquist Plot in Fig. 5.15.

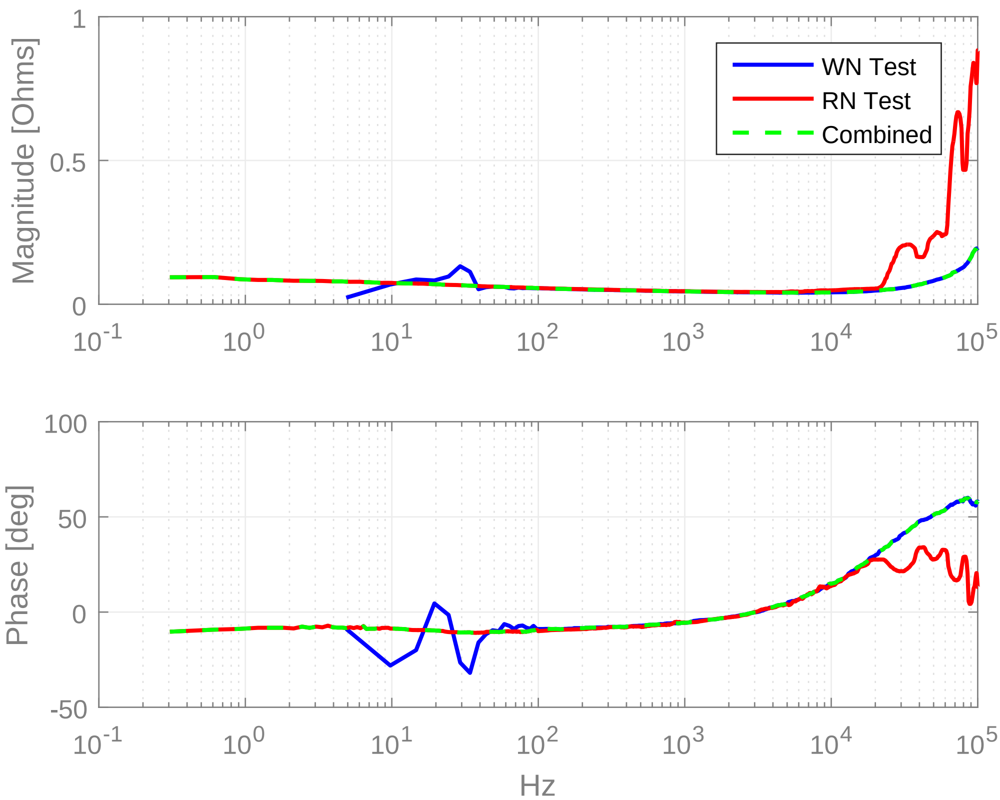

Figure 5.13 : Illustration of measurements at 25% SOC under closed-loop operation for WN test (blue line), RN test (red line) and combination of both tests (green dashed line).

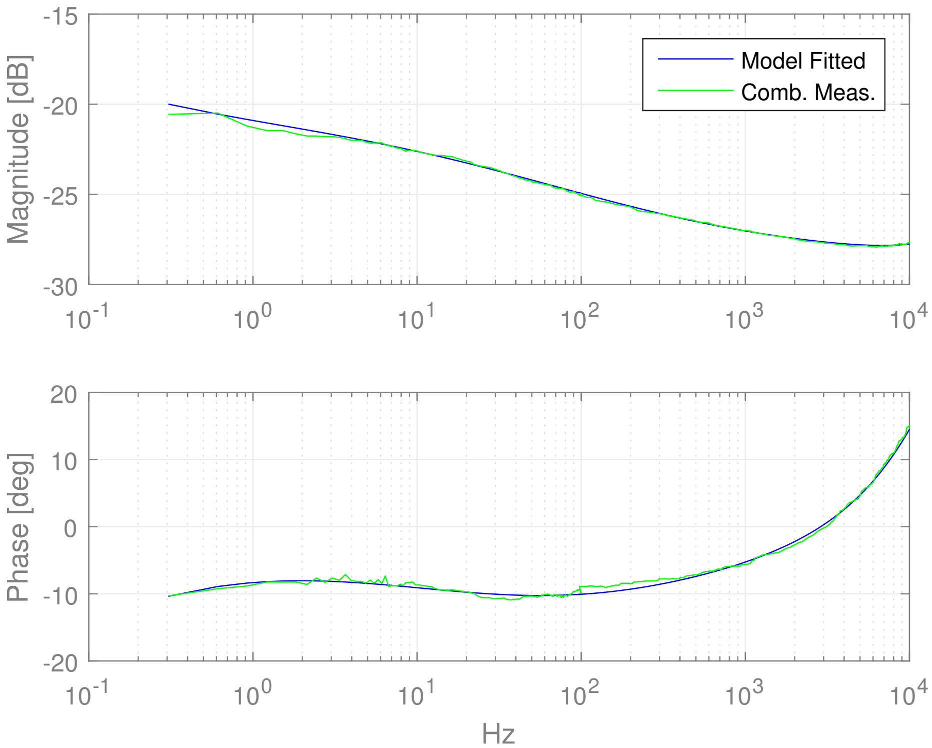

Figure 5.14 : Illustration of combined measurements (green line) and model fitted results (blue line) at 25% SOC under closed-loop operation.

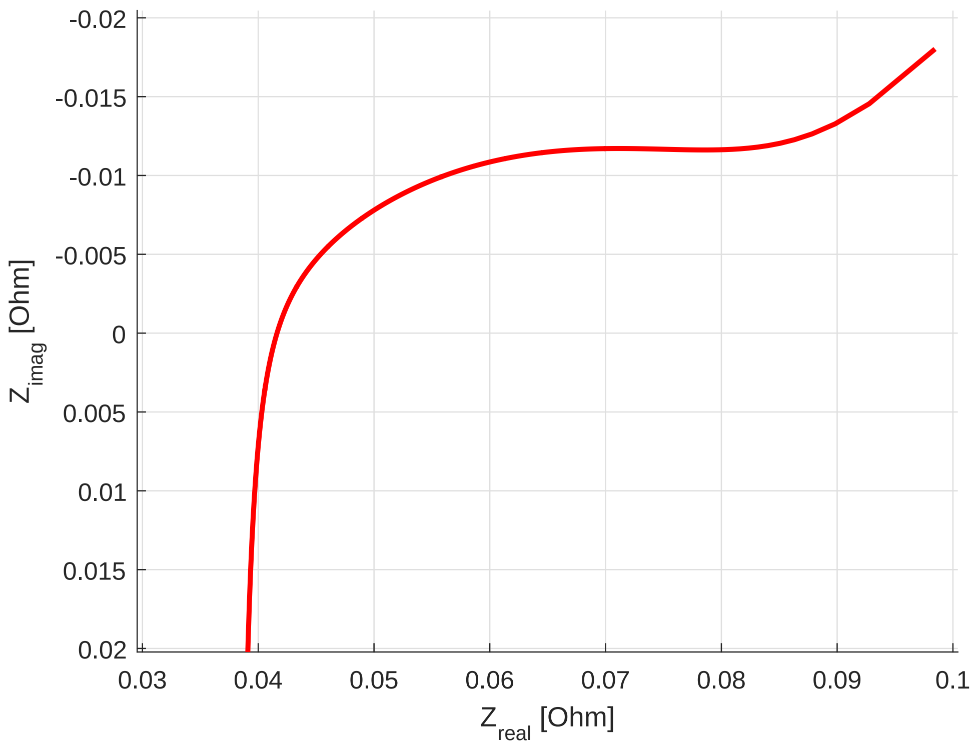

Figure 5.15 : Illustration Nyquist Plot for model fitted results at 25% SOC under closed-loop operation.

As it can be seen from the figures, a dramatic change in both the Bode and Nyquist Plots is observed in comparison with the impedance measurement results obtained for 50% SOC. Basically, the curve on the Nyquist plot seem to shift to the right-side, representing an increase in the real part of the impedance.

5.2.5 Experiment 4: 75% SOC, closed-loop operation

Finally, the battery is tested at 75% SOC. Fig. 5.16 illustrates the results of the test at 75% SOC under closed-loop operation. As usual, the results are then fitted to an equivalent model circuit, which is illustrated in Fig. 5.17. Finally, the model fitted results are also presented as a Nyquist Plot in Fig. 5.18.

As it can be seen from the figures, again a dramatic change in both the Bode and Nyquist Plots is observed in comparison with the impedance measurement results obtained for 50% SOC. However this time, contrary to the case of 25% SOC, the curve on the Nyquist plot seem to shift to the left-side, representing a decrease in the real part of the impedance.

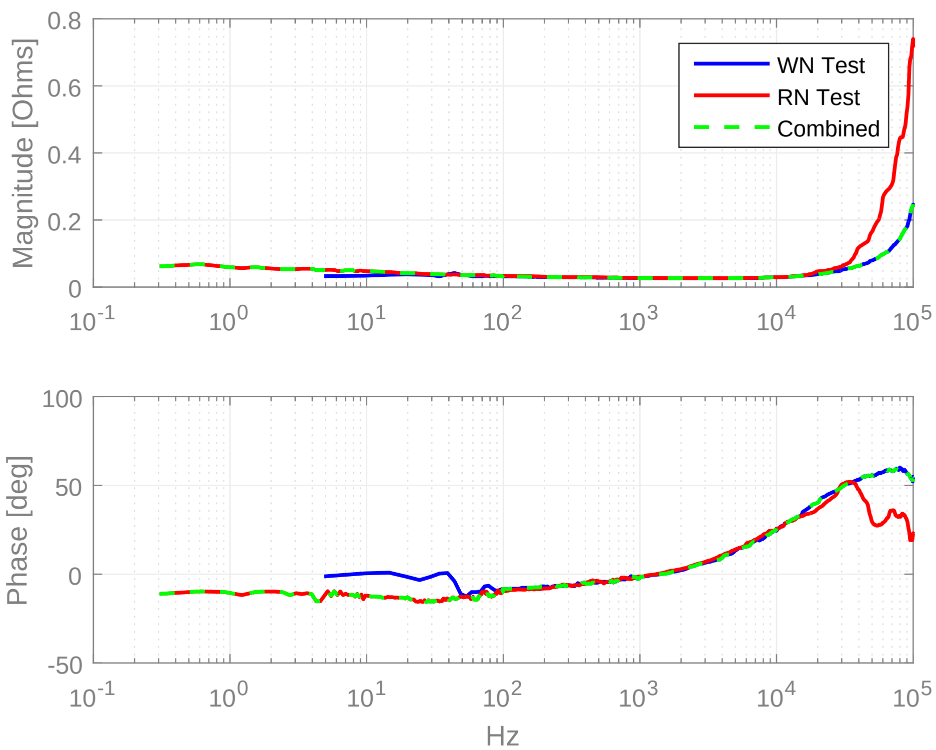

Figure 5.16 : Illustration of measurements at 75% SOC under closed-loop operation for WN test (blue line), RN test (red line) and combination of both tests (green dashed line).

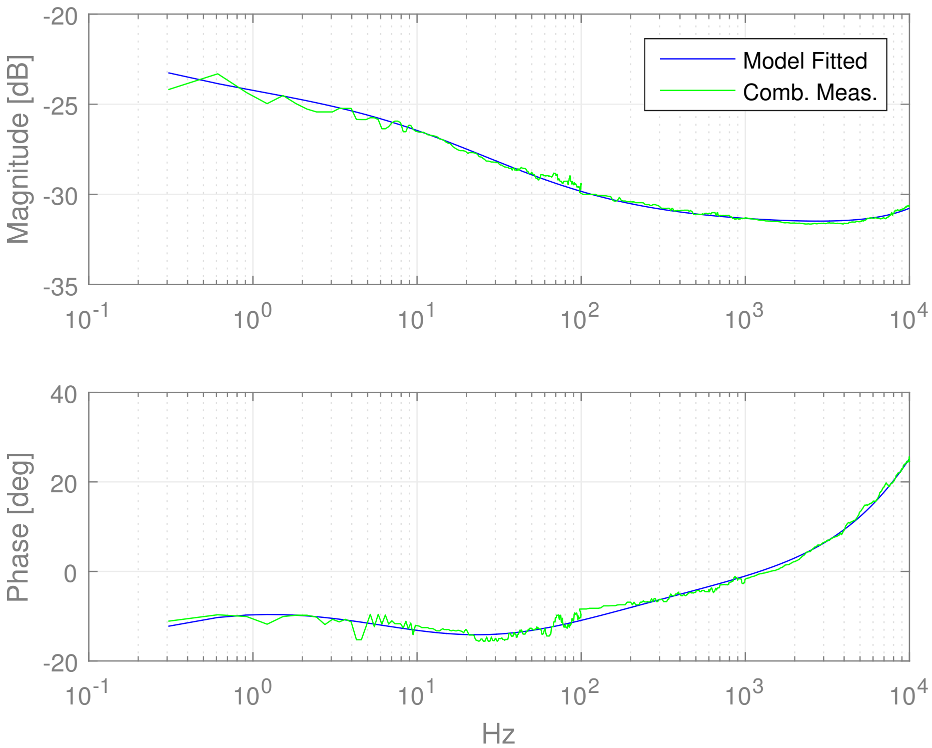

Figure 5.17 : Illustration of combined measurements (green line) and model fitted results (blue line) at 75% SOC under closed-loop operation.

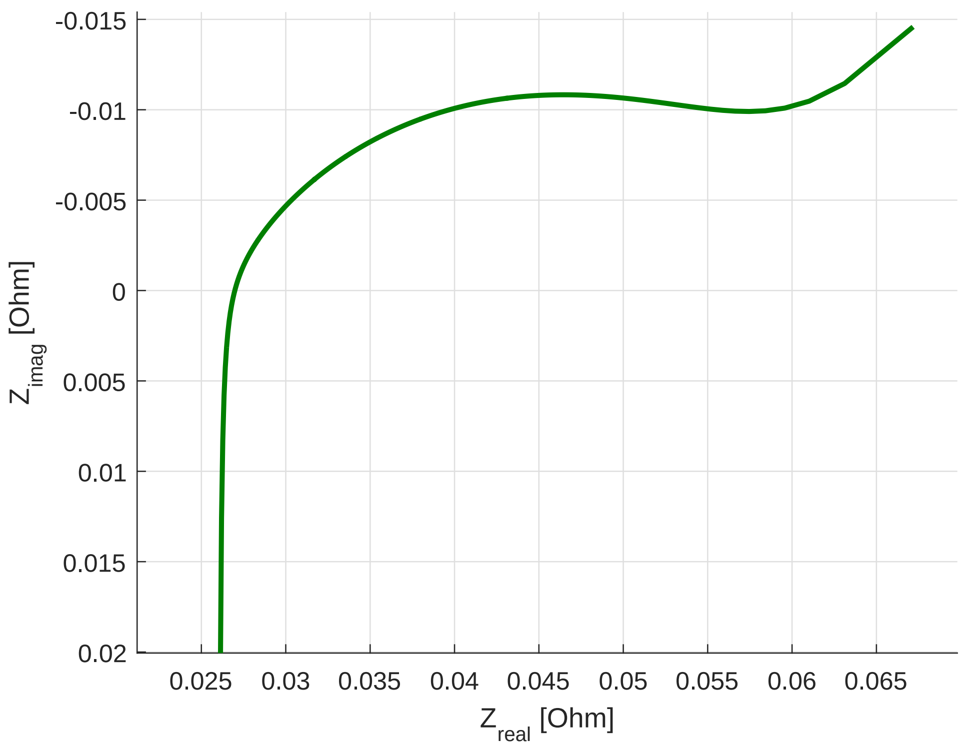

Figure 5.18 : Illustration Nyquist Plot for model fitted results at 75% SOC under closed-loop operation.

5.3 Concluding Remarks

The extracted parameters from each tests has been illustrated in form of Nyquist Plots in Fig. 5.19 for demonstrating the behaviour of the impedance by the change of SOC.

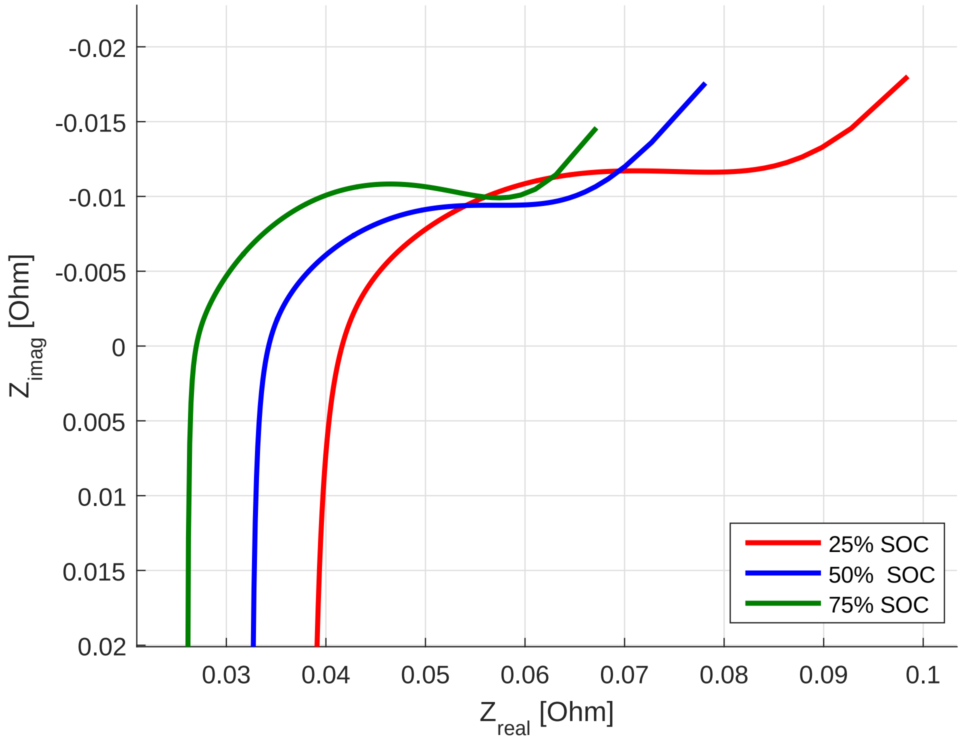

Figure 5.19 : Comparison of impedance measurements at 25%, 50% and 75% SOC.

As it can be clearly seen from the figure, the SOC affects the obtained Nyquist Plots of the battery. As also demonstrated in the literature [56], the increasing SOC causes the Nyquist plot to shift to the left-side, representing an decrease in the real part of the battery impedance.

Finally, Table 5.1 demonstrates the variations of the extracted parameters according to the previously presented battery equivalent model in response to the change of the SOC. As pointed out in the literature survey, the EIS results need a comprehensive interpretation of the results in order to derive a good relationship between a specific battery parameter and SOC. However, this thesis only aims propose an improved methodology for implementing the EIS capability to the DC-DC converters.

Table 5.1 : Extracted Parameters for different SOC values.

Parameter	25% SOC	50% SOC	75% SOC
L_e [$\mu Henry$]	1.9678e-7	1.9370e-7	2.0254e-7
R_e [Ω]	0.0372	0.0321	0.0259
R_1 [Ω]	0.0517	0.0318	0.0333
Q_1 [F]	1.5597	1.5948	1.5804
α_1	0.4770	0.5653	0.6552
χ [Ω/mm]	0.2619	0.0016	0.00028
L_{BTS} [mm]	3030.5	64.47	447.5171
r_{BTS} [$\Omega.mm$]	405.9	28.524	1049.5
q_{BTS} [F/mm]	329.3198	1.61	0.53
α_{BTS}	1.0507	1.0140	1.1765

As, SOC estimation based on EIS results are not within the scope of the thesis and thus the results will not be elaborated further.

6. CONCLUSIONS AND RECOMMENDATIONS

This work contributes to the current state of the art by offering an alternative method for the integration of online EIS measurement capabilities into the digitally controlled DC-DC converters. As EIS is considered to be the most powerful tool for the diagnosis of the batteries, this work relates to a crucial aspect of battery management systems by providing a very powerful diagnostic tool for the battery which can be utilized without interrupting the operation of the system.

The proposed methodology is firstly examined by computer simulations. Afterwards the methodology was demonstrated on an experimental setup comprising an FPGA controlled, boost converter based battery charger connected to a 12-V, 7-Ah Yuasa NP7-12 lead-acid battery. The battery was tested at 25%, 50% and 75% SOC values. The test results exhibit a strong correlation between the proposed method and the reference measurements that were taken by commercially available and high precision instruments.

Within the scope of the presented study, a few improvements regarding cross-correlation based EIS measurements, in particular regarding EIS of batteries, have been presented:

- It has been demonstrated that the moving average filter can be effectively used for removing unwanted dynamic effects, such as the varying open circuit voltage of the battery, during testing period: As the battery is operational during testing, the open circuit voltage is not fixed and thus the moving average filter performed on the battery voltage and current waveforms are essential for isolating the perturbation based waveforms.
- It has been proposed to perform two subtests with different noise types within one testing cycle: A red noise test in addition to white noise test has been found to be very effective for improving the measurement quality in low frequency band. Furthermore, this approach also enables to adjust the measurement resolution in the

low frequency range. As it is generally more preferred to have a smaller resolution in low frequency, this can be achieved by increasing the perturbation data length of the red noise test. For example in the experiment section of this work, the red noise data length is determined to be 2^{16} resulting in a resolutin of $\Delta f = 0.3052$ Hz, while the white noise test comprises a data set of 2^{12} length yielding a resolution of $\Delta f = 4.8818$ Hz.

- The perturbation data generation and preparation has been discussed. Additionally, it has been demonstrated how a proper perturbation magnitude can be chosen.
- Effective post-processing tools are discussed and demonstrated. In this regard, a fractional decade post-processing method has been suggested.
- Although the proposed technique is not a model based approach, meaning that the measured data does not have to be interpreted according to an equivalent electrical model, a model fitting application has been demonstrated which enables parameter extraction which is generally utilized for various estimation procedures.

The benefits of the proposed approach are:

- The method does not require frequency sweeping. In other words, instead of performing individual tests for each frequency, the cross-correlation based identification enables obtaining measurements containing a wide frequency range.
- Testing time is significantly lower than that of the techniques requiring separate tests for each frequency of interest.
- The proposed technique is applicable to online applications so that the battery to be tested may remain operational during the tests.
- No extra circuitry is needed in the power stage, as the approach is fully integrated into the DC-DC converters. Consequently the offered approach is a low cost application.
- The approach may be retrofitted to already existing systems.

On the other hand, there are also a few challenges that need to be taken into consideration for implementing the proposed approach:

- Although not considered a challenge specific to the proposed method, the proposed technique requires high resolution ADCs in order to be able to detect small magnitude, perturbation based voltage and current waveforms.

- The proposed technique is not able to analyse a single given frequency. The cross-correlation based identification technique always result in a measurement containing a certain range of frequency.

- The resolution of the results depend on the total sampled data points. Analyzing very low-frequencies (less than mHz range) may cause a lot of computational effort. This might be avoided by decreasing the sampling frequency with the cost of less precision at high-frequency impedance analysis.

- Analogous to most online applications, the proposed approach is not suitable for analysing very low frequencies, as the testing time would be too high. Higher testing times are not suitable for such applications because the state of batteries (such as SOC and temperature) may change during the testing period and in turn this would invalidate the measurements. Thus, online applications are not expected to reach μHz levels in contrast to off-line EIS devices, which maintain the states of the battery under test.

- The proposed method requires precise duty cycle control, as a perturbation has to be applied to duty cycle command at each switching cycle. This perturbation could be challenging to implement into some digital controllers. As widely utilized in similar works, an FPGA is suggested for this approach.

REFERENCES

[1] **Waag, W.**, **Käbitz, S. and Sauer, D.U.** (2013). Experimental investigation of the lithium-ion battery impedance characteristic at various conditions and aging states and its influence on the application, *Applied Energy*, *102*, 885 – 897, http://www.sciencedirect.com/science/article/pii/S030626191200671X, special Issue on Advances in sustainable biofuel production and use - {XIX} International Symposium on Alcohol Fuels - {ISAF}.

[2] **Christophersen, J.P.**, Battery State-of-Health Assessment Using a Near Real-time Impedance Measurement Technique Under No-load and Load Conditions.

[3] **Rodrigues, S.**, **Munichandraiah, N. and Shukla, A.** (2000). A review of state-of-charge indication of batteries by means of a.c. impedance measurements, *Journal of Power Sources*, *87*(1–2), 12 – 20.

[4] **Huet, F.** (1998). A review of impedance measurements for determination of the state-of-charge or state-of-health of secondary batteries, *Journal of Power Sources*, *70*(1), 59 – 69.

[5] **Mauracher, P. and Karden, E.** (1997). Dynamic modelling of lead/acid batteries using impedance spectroscopy for parameter identification, *Journal of Power Sources*, *67*(1), 69 – 84, http://www.sciencedirect.com/science/article/pii/S0378775397024981.

[6] **Hammouche, A.**, **Karden, E. and Doncker, R.W.D.** (2004). Monitoring state-of-charge of Ni–MH and Ni–Cd batteries using impedance spectroscopy, *Journal of Power Sources*, *127*(1–2), 105 – 111, http://www.sciencedirect.com/science/article/pii/S0378775303009443, eighth Ulmer Electrochemische Tage.

[7] **Blanke, H.**, **Bohlen, O.**, **Buller, S.**, **Doncker, R.W.D.**, **Fricke, B.**, **Hammouche, A.**, **Linzen, D.**, **Thele, M. and Sauer, D.U.** (2005). Impedance measurements on lead–acid batteries for state-of-charge, state-of-health and cranking capability prognosis in electric and hybrid electric vehicles, *Journal of Power Sources*, *144*(2), 418 – 425, http://www.sciencedirect.com/science/article/pii/S0378775304011140, selected papers from the Ninth European Lead Battery ConferenceNinth European Lead Battery Conference.

[8] **Jespersen, J.**, **Tønnesen, A.**, **Nørregaard, K.**, **Overgaard, L. and Elefsen, F.** (2009). Capacity Measurements of Li-Ion Batteries using AC Impedance Spectroscopy, *World Electric Vehicle Journal*, *3*(1), 127–133, http://www.mdpi.com/2032-6653/3/1/127.

[9] **Luo, Y.F.**, **Gong, C.S.A.**, **Chang, L.X. and Liu, Y.H.** (2013). AC impedance technique for dynamic and static state of charge analysis for Li-ion battery, *2013 IEEE International Symposium on Consumer Electronics (ISCE)*, pp.9–10.

[10] **Stroe, D.I.**, **Swierczynski, M.**, **Stan, A.I.**, **Knap, V.**, **Teodorescu, R. and Andreasen, S.J.** (2014). Diagnosis of lithium-ion batteries state-of-health based on electrochemical impedance spectroscopy technique, *2014 IEEE Energy Conversion Congress and Exposition (ECCE)*, pp.4576–4582.

[11] **Zhu, J.**, **Sun, Z.**, **Wei, X. and Dai, H.** (2015). A new lithium-ion battery internal temperature on-line estimate method based on electrochemical impedance spectroscopy measurement, *Journal of Power Sources*, *274*, 990 – 1004, `http://www.sciencedirect.com/science/article/pii/S0378775314018011`.

[12] **Densmore, A. and Hanif, M.** (2015). Determining battery SoC using Electrochemical Impedance Spectroscopy and the Extreme Learning Machine, *Future Energy Electronics Conference (IFEEC), 2015 IEEE 2nd International*, pp.1–7.

[13] **Miao, B.**, **Zane, R. and Maksimovic, D.** (2005). Practical on-line identification of power converter dynamic responses, *Twentieth Annual IEEE Applied Power Electronics Conference and Exposition, 2005. APEC 2005.*, volume 1, pp.57–62 Vol. 1.

[14] **Miao, B.**, **Zane, R. and Maksimovic, D.** (2005). System identification of power converters with digital control through cross-correlation methods, *Power Electronics, IEEE Transactions on*, *20*(5), 1093–1099.

[15] **Miao, B.**, **Zane, R. and Maksimović, D.** (2006). FPGA-Based Digital Network Analyzer for Digitally Controlled SMPS, *Computers in Power Electronics, 2006. COMPEL '06. IEEE Workshops on*.

[16] **Vilkko, M. and Roinila, T.** (2008). Designing Maximum Length Sequence Signal for Frequency Response Measurements of Switched Mode Converters, *NORPIE/2008, Nordic Workshop on Power and Industrial Electronics*.

[17] **Barkley, A. and Santi, E.** (2008). Improved online identification of switching converters using digital network analyzer techniques, *2008 IEEE Power Electronics Specialists Conference*, pp.891–896.

[18] **Shirazi, M.**, **Morroni, J.**, **Dolgov, A.**, **Zane, R. and Maksimovic, D.** (2008). Integration of Frequency Response Measurement Capabilities in Digital Controllers for DC-DC Converters, *Power Electronics, IEEE Transactions on*, *23*(5).

[19] **Jun-Yan Liu**, **Chun-Hung Yang and Chien-Hung Tsai** (2011). Correlation-based system identification of digitally controlled SMPS, *2011 IEEE Ninth International Conference on Power Electronics and Drive Systems*, pp.1149–1152.

[20] **Granda, M.**, **Fernandez, C.**, **Barrado, A. and Zumel, P.** (2021). Nonparametric Frequency Response Identification for Dc-Dc Converters Based on Spectral Analysis with Automatic Determination of the Perturbation Amplitude, *Sensors*, *21*(9), `https://www.mdpi.com/1424-8220/21/9/3234`.

[21] **Waligo, A. and Barendse, P.** (2016). A comparison of the different broadband impedance measurement techniques for lithium-ion batteries, *2016 IEEE Energy Conversion Congress and Exposition (ECCE)*, pp.1–7.

[22] **Howey, D.**, **Mitcheson, P.**, **Yufit, V.**, **Offer, G. and Brandon, N.** (2014). Online Measurement of Battery Impedance Using Motor Controller Excitation, *Vehicular Technology, IEEE Transactions on*, *63*(6), 2557–2566.

[23] **Kim, J.**, **Krüger, L. and Kowal, J.** (2020). On-line state-of-health estimation of Lithium-ion battery cells using frequency excitation, *Journal of Energy Storage*, *32*, 101841, `http://www.sciencedirect.com/science/article/pii/S2352152X20316789`.

[24] **Hossain, M.K. and Islam, S.M.R.** (2017). Battery Impedance Measurement Using Electrochemical Impedance Spectroscopy Board, *2017 2nd International Conference on Electrical Electronic Engineering (ICEEE)*, pp.1–4.

[25] **Gong, Z.**, **Liu, Z.**, **Wang, Y.**, **Gupta, K.**, **da Silva, C.**, **Liu, T.**, **Zheng, Z.H.**, **Zhang, W.P.**, **van Lammeren, J.P.M.**, **Bergveld, H.J.**, **Amon, C.H. and Trescases, O.** (2018). IC for online EIS in automotive batteries and hybrid architecture for high-current perturbation in low-impedance cells, *2018 IEEE Applied Power Electronics Conference and Exposition (APEC)*, pp.1922–1929.

[26] **Depernet, D.**, **Ba, O. and Berthon, A.** (2012). Online impedance spectroscopy of lead acid batteries for storage management of a standalone power plant, *Journal of Power Sources*, *219*, 65 – 74, `http://www.sciencedirect.com/science/article/pii/S0378775312011780`.

[27] **Faloye, O.M. and Barendse, P.** (2019). A Three Level DC-DC Converter for Battery Impedance Spectroscopy, *2019 IEEE Energy Conversion Congress and Exposition (ECCE)*, pp.2682–2689.

[28] **Bayati, M.**, **Abedi, M.**, **Gharehpetian, G.B. and Farahmandrad, M.** (2020). Sinusoidal-Ripple Current Control in Battery Charger of Electric Vehicles, *IEEE Transactions on Vehicular Technology*, *69*(7), 7201–7210.

[29] **Huang, W. and Qahouq, J.** (2014). An Online Battery Impedance Measurement Method Using DC-DC Power Converter Control, *Industrial Electronics, IEEE Transactions on*, *61*(11), 5987–5995.

[30] **Van-Tuan Doan**, **Van-Binh Hu**, **Hai-Nam Vu**, **Duc-Hung Tran and Woojin Choi** (2015). Intelligent charger with online battery diagnosis function, *9th International Conference on Power Electronics-ECCE Asia*, pp.1644–1649.

[31] **Islam, S.M.R. and Park, S.** (2020). Precise Online Electrochemical Impedance Spectroscopy Strategies for Li-Ion Batteries, *IEEE Transactions on Industry Applications*, *56*(2), 1661–1669.

[32] **Thanh-Tuan Nguyen**, **Van-Long Tran and Woojin Choi** (2014). Development of the intelligent charger with battery State-Of-Health estimation using online impedance spectroscopy, *2014 IEEE 23rd International Symposium on Industrial Electronics (ISIE)*, pp.454–458.

[33] **Lee, Y.D.**, **Park, S.Y. and Han, S.B.** (2015). Online Embedded Impedance Measurement Using High-Power Battery Charger, *Industry Applications, IEEE Transactions on*, *51*(1), 498–508.

[34] **Varnosfaderani, M.A. and Strickland, D.** (2016). Online impedance spectroscopy estimation of a battery, *2016 18th European Conference on Power Electronics and Applications (EPE'16 ECCE Europe)*, pp.1–10.

[35] **Yela, J.C.**, **Benshatti, A.**, **Link, T.**, **Rakiul Islam, S.M. and Park, S.Y.** (2020). Simple and Low-Cost Online AC Ripple Current Injection Methods for a Single-Cell Li-ion Battery, *2020 IEEE Energy Conversion Congress and Exposition (ECCE)*, pp.4418–4422.

[36] **Moore, S. and Barendse, P.** (2017). Online condition monitoring of lithium-ion batteries using impedance spectroscopy, *2017 IEEE Energy Conversion Congress and Exposition (ECCE)*, pp.5617–5624.

[37] **Díaz-González (Serra Húnter Fellow).**, **F.**, **Heredero-Peris, D. and Galceran-Arellano, S.** (2018). Design methodology for a dc–dc power conversion system with EIS capability for battery packs, *Simulation Modelling Practice and Theory*, *87*, 15 – 34, `http://www.sciencedirect.com/science/article/pii/S1569190X18300716`.

[38] **Yao, Q.**, **Lu, D. and Lei, G.** (2019). Battery Impedance Measurement Using Fast Square Current Perturbation, *2019 IEEE 4th International Future Energy Electronics Conference (IFEEC)*, pp.1–5.

[39] **Yao, Q.**, **Lu, D.D.C. and Lei, G.** (2021). Accurate Online Battery Impedance Measurement Method with Low Output Voltage Ripples on Power Converters, *Energies*, *14*(4), `https://www.mdpi.com/1996-1073/14/4/1064`.

[40] **Yokoshima, T.**, **Mukoyama, D.**, **Nara, H.**, **Maeda, S.**, **Nakazawa, K.**, **Momma, T. and Osaka, T.** (2017). Impedance Measurements of Kilowatt-Class Lithium Ion Battery Modules/Cubicles in Energy Storage Systems by Square-Current Electrochemical Impedance Spectroscopy, *Electrochimica Acta*, *246*, 800 – 811, `http://www.sciencedirect.com/science/article/pii/S0013468617310721`.

[41] **Koch, R.**, **Kuhn, R.**, **Zilberman, I. and Jossen, A.** (2014). Electrochemical impedance spectroscopy for online battery monitoring - power electronics control, *2014 16th European Conference on Power Electronics and Applications*, pp.1–10.

[42] **Qahouq, J.A.A. and Xia, Z.** (2017). Single-Perturbation-Cycle Online Battery Impedance Spectrum Measurement Method With Closed-Loop Control of Power Converter, *IEEE Transactions on Industrial Electronics*, *64*(9), 7019–7029.

[43] **Xia, Z. and Qahouq, J.A.A.** (2017). Method for online battery AC impedance spectrum measurement using dc-dc power converter duty-cycle control, *2017 IEEE Applied Power Electronics Conference and Exposition (APEC)*, pp.1999–2003.

[44] **Kersten, A.**, **Kuder, M.**, **Han, W.**, **Thiringer, T.**, **Lesnicar, A.**, **Weyh, T. and Eckerle, R.** (2020). Online and On-Board Battery Impedance Estimation of Battery Cells, Modules or Packs in a Reconfigurable Battery System or Multilevel Inverter, *IECON 2020 The 46th Annual Conference of the IEEE Industrial Electronics Society*, pp.1884–1891.

[45] **La, P.H. and Choi, S.J.** (2021). Integrated On-line EIS Measurement Scheme Utilizing Flying Capacitor Equalizer for Series Battery String, *2021 IEEE Applied Power Electronics Conference and Exposition (APEC)*, pp.975–980.

[46] **Koseoglou, M.**, **Tsioumas, E.**, **Papagiannis, D.**, **Jabbour, N. and Mademlis, C.** (2021). A Novel On-Board Electrochemical Impedance Spectroscopy System for Real-Time Battery Impedance Estimation, *IEEE Transactions on Power Electronics*, *36*(9), 10776–10787.

[47] **Sihvo, J.**, **Stroe, D.**, **Messo, T. and Roinila, T.** (2020). Fast Approach for Battery Impedance Identification Using Pseudo-Random Sequence Signals, *IEEE Transactions on Power Electronics*, *35*(3), 2548–2557.

[48] **Xia, Z. and Abu Qahouq, J.A.** (2020). High Frequency Online Battery Impedance Measurement Method Using Voltage and Current Ripples Generated by DC-DC Converter, *2020 IEEE Applied Power Electronics Conference and Exposition (APEC)*, pp.1333–1338.

[49] **Gücin, T.N. and Ovacık, L.** (2016). An impedance analyzer application using cross-correlation method, *2016 IEEE International Conference on Renewable Energy Research and Applications (ICRERA)*, pp.265–269.

[50] **Barkley, A. and Santi, E.** (2009). Online Monitoring of Network Impedances Using Digital Network Analyzer Techniques, *Applied Power Electronics Conference and Exposition, 2009. APEC 2009. Twenty-Fourth Annual IEEE*, pp.440–446.

[51] **Gücin, T.N. and Ovacik, L.** (2020). Online Impedance Measurement of Batteries Using the Cross-Correlation Technique, *IEEE Transactions on Power Electronics*, *35*(4), 4365–4375.

[52] **Kido, K.** (2007). *Digital Fourier Analysis: Advanced Techniques*, Springer.

[53] **Oppenheim, A.V. and Schafer, R.W.** (1999). *Discrete-Time Signal Processing*, Prentice Hall.

[54] **Barkley, A.B.**, (2010), Online Identification, Monitoring, and Control of a DC/DC Converter System Using Digital Network Analyzer Techniques.

[55] **Ehlers, J.**, (2019), Signal Analysis Concepts, `http://www.technicalanalysis.org.uk/moving-averages/Ehle.pdf`.

[56] **Aksakal, C. and Sisman, A.** (2018). On the Compatibility of Electric Equivalent Circuit Models for Enhanced Flooded Lead Acid Batteries Based on Electrochemical Impedance Spectroscopy, *Energies*, *11*(1).

[57] URL-1, <https://www.gamry.com/application-notes/EIS/use-of-transmission-lines-for-eis/>, [Online; accessed on 01-July-2018].

[58] **Bisquert, J.** (2000). Influence of the boundaries in the impedance of porous film electrodes, *Phys. Chem. Chem. Phys.*, *2*, 4185–4192, `http://dx.doi.org/10.1039/B001708F`.

[59] **Erickson, R.W. and Maksimovic, D.** (2001). *Fundamentals of Power Electronics*, Springer, 2ed edition.

[60] **Boukamp, B.A.** (1995). A Linear Kronig-Kramers Transform Test for Immittance Data Validation, *Journal of The Electrochemical Society*, *142*, 1885 – 1894.

[61] **Schönleber, M.**, **Goyal, R. and Ivers-Tiffée, E.**, (2014), Lin-KK Tool, `https://www.iam.kit.edu/wet/english/Lin-KK.php`.

APPENDICES

APPENDIX A.1: Main Program

```
library IEEE;
use IEEE.STD_LOGIC_1164.ALL;
use IEEE.NUMERIC_STD.ALL;

entity main is
Port (
BTNC: in std_logic :='0';
CLK100MHZ: in std_logic :='0';
SW: in unsigned (15 downto 0); -- sw15-7 (9bit) --> M ||
 ↪  sw6-4 (3bit) --> fsw ayarı || sw3-0 (4bit) --> fp
 ↪  ayarı
LED: out unsigned (15 downto 0);
JA1: inout std_logic :='0';
JA2: inout std_logic :='0';
JA3: inout std_logic :='0';
JA4: inout std_logic :='0';
JA7: inout std_logic :='0';
JA8: inout std_logic :='0';
JA9: inout std_logic :='0';
JA10: inout std_logic :='0';
duty_ss: in std_logic_vector (31 downto 0);
perturb_scale: inout std_logic_vector (31 downto 0);
main_data_length: in integer range 0 to 1000000;
main_read_address: out std_logic_vector (15 downto 0);
main_wn_data: in std_logic_vector (7 downto 0);
main_bn_data: in std_logic_vector (7 downto 0);
main_pn_data: in std_logic_vector (7 downto 0);
main_rn_data: in std_logic_vector (7 downto 0)
);
end main;

architecture yapisal of main is
signal s_prescale_rate: unsigned (26 downto 0);
signal s_prescale_rate2: unsigned (26 downto 0);
signal s_CLK_prescaled: std_logic := '0';
signal s_CLK_prescaled2: std_logic := '0';
signal s_enable_count: std_logic;
signal s_start: unsigned (26 downto 0);
signal s_stop: unsigned (26 downto 0);
signal s_deadtime: unsigned (26 downto 0);
signal s_count_te: unsigned (26 downto 0);
signal s_cnt_type_te : unsigned (1 downto 0);
signal s_signal: std_logic;

component perturb
```

```vhdl
Port (
def_CLK100MHZ: in std_logic;
def_CLK_prescaled: in std_logic;
def_CLK_prescaled_perturb: in std_logic :='0';
def_sw: in unsigned (15 downto 0);
test_start: in std_logic;
def_signal: out std_logic;
def_start: inout unsigned (26 downto 0);
def_stop: inout unsigned (26 downto 0);
def_deadtime: inout unsigned (26 downto 0);
def_debug: inout std_logic :='0';
def_debug2: inout std_logic :='0';
def_pre: inout unsigned (26 downto 0);
def_pre_perturb: inout unsigned (26 downto 0);
def_duty_ss: in std_logic_vector (31 downto 0);
def_perturb_scale: inout std_logic_vector (31 downto 0);
data_length: in integer range 0 to 1000000;
read_address: out std_logic_vector (15 downto 0);
wn_data: in std_logic_vector (7 downto 0);
bn_data: in std_logic_vector (7 downto 0);
pn_data: in std_logic_vector (7 downto 0);
rn_data: in std_logic_vector (7 downto 0)
);
end component perturb;

component prescaler
port(
prscl_CLK100MHZ: in std_logic;
prscl_prescale_rate: in unsigned (26 downto 0);
prscl_CLK_prescaled: inout std_logic
);
end component prescaler;

component counter is
generic (cntr_type: in unsigned (1 downto 0));
port(
enable: in std_logic;
cntr_CLK: in std_logic;
cntr_CLK_prescaled: in std_logic :='0';
cntr_stop: in unsigned (26 downto 0);
cntr_type_out: out unsigned (1 downto 0);
cntr_count: inout unsigned (26 downto 0)
);
end component counter;

component pwm_module is
port(
pwm_CLK: in std_logic :='0';
```

```
pwm_start: in unsigned (26 downto 0);
pwm_stop: in unsigned (26 downto 0);
pwm_deadtime: in unsigned (26 downto 0);
pwm_count: in unsigned (26 downto 0);
pwm_pre: in unsigned (26 downto 0);
pwm_cntr_type: in unsigned (1 downto 0);
pwm_pwm_out: out std_logic;
pwm_pwm_out_comp: out std_logic
);
end component pwm_module;

begin

LED <= SW;
s_enable_count <= '1';
JA3 <= s_CLK_prescaled;
JA7 <= s_CLK_prescaled2;
JA8 <= s_signal;

Pertur: perturb port map (
def_CLK100MHZ => CLK100MHZ,
def_CLK_prescaled => s_CLK_prescaled,
def_CLK_prescaled_perturb => s_CLK_prescaled2,
def_sw => SW,
test_start => BTNC,
def_signal => s_signal,--test_request in perturb @ JA8
def_pre => s_prescale_rate,
def_pre_perturb => s_prescale_rate2,
def_start => s_start,
def_stop => s_stop,
def_debug => JA4,
def_debug2 => JA9,
def_deadtime => s_deadtime,
def_duty_ss => duty_ss,
def_perturb_scale => perturb_scale,
data_length => main_data_length,
read_address => main_read_address,
wn_data => main_wn_data,
bn_data => main_bn_data,
pn_data => main_pn_data,
rn_data => main_rn_data
);

PRSCL: prescaler port map (
prscl_CLK100MHZ => CLK100MHZ,
prscl_prescale_rate => s_prescale_rate,
prscl_CLK_prescaled => s_CLK_prescaled
);
```

```
PRSCL2: prescaler port map (
prscl_CLK100MHZ => CLK100MHZ,
prscl_prescale_rate => s_prescale_rate2,
prscl_CLK_prescaled => s_CLK_prescaled2
);

CNTR_te: counter   generic map (cntr_type => "00")
port map (
enable => s_enable_count,
cntr_CLK => CLK100MHZ,
cntr_CLK_prescaled => s_CLK_prescaled,
cntr_stop => s_prescale_rate,
cntr_type_out => s_cnt_type_te,
cntr_count => s_count_te
);

PWM_GEN_te: pwm_module port map (
pwm_CLK => CLK100MHZ,
pwm_start => s_start,
pwm_stop => s_stop,
pwm_deadtime => s_deadtime,
pwm_count => s_count_te,
pwm_pre => s_prescale_rate,
pwm_cntr_type => s_cnt_type_te,
pwm_pwm_out => JA1,
pwm_pwm_out_comp => JA2
);

end yapisal;
```

APPENDIX A.2: Subprogram for Applying the Perturbation

```vhdl
library IEEE;
use IEEE.STD_LOGIC_1164.ALL;
use IEEE.NUMERIC_STD.ALL;

entity perturb is
Port (
def_CLK100MHZ: in std_logic := '0';
def_CLK_prescaled: in std_logic :='0';
def_CLK_prescaled_perturb: in std_logic :='0';
def_sw: in unsigned (15 downto 0);
test_start: in std_logic :='0';
def_signal: out std_logic := '0';
def_start: inout unsigned (26 downto 0);
def_stop: inout unsigned (26 downto 0);
def_deadtime: inout unsigned (26 downto 0);
def_debug: inout std_logic :='0';
def_debug2: inout std_logic :='0';
def_pre: inout unsigned (26 downto 0);
def_pre_perturb: inout unsigned (26 downto 0);
def_duty_ss: in std_logic_vector (31 downto 0);
def_perturb_scale: inout std_logic_vector (31 downto 0);
data_length: in integer range 0 to 1000000;
read_address: out std_logic_vector (15 downto 0);
wn_data: in std_logic_vector (7 downto 0);
bn_data: in std_logic_vector (7 downto 0);
pn_data: in std_logic_vector (7 downto 0);
rn_data: in std_logic_vector (7 downto 0)
);
end perturb;

architecture davranissal of perturb is

shared variable random_integer_array: integer range -255 to 255 := 0;
signal button_delay: unsigned (26 downto 0) := "000000000000100111000100000";
signal button_count: unsigned (26 downto 0) := "000000000000000000000000000";
signal random_temp: integer range -2000 to 2000 :=0;
signal s_pre: unsigned (26 downto 0) := "000000000000000001111101000";
signal s_pre_perturb: unsigned (26 downto 0) := "000000000000000001111101000";
signal s_deadtime: unsigned (26 downto 0) :="000000000000000000000000000";
signal s_start: unsigned (26 downto 0) :="000000000000000000000000000";
```

```
signal s_stop: unsigned (26 downto 0);--
 ↪  :="000000000000000000111110100";
signal s_stop_temp: integer range -100000 to 100000 :=0;
signal test_request: std_logic := '0';
signal test_request_temp: std_logic := '0';
shared variable test_request_hold: std_logic_vector(2
 ↪  downto 0):= "000";
shared variable i: integer range 0 to 1000000 := 0;
shared variable k: integer range 0 to 10000 := 0;
signal s_duty_ss: integer range 0 to 10000 := 500;
signal M: integer range 0 to 1000; -- repeating  M times

begin
test_request_temp <= test_request;
def_start <= s_start;
def_deadtime <= s_deadtime;
def_pre <= s_pre;
def_pre_perturb <= s_pre_perturb;
M <= 1 + to_integer(def_sw(13 downto 7));
s_duty_ss <= to_integer(unsigned(def_duty_ss));
button_delay <= "000000000000100111000100000";

test_req_delay: process(def_CLK_prescaled)
begin
if rising_edge(def_CLK_prescaled) then
test_request_hold(2) := test_request_hold(1);
test_request_hold(1) := test_request_hold(0);
def_signal <= test_request_hold(1);
test_request_hold(0) := test_request_temp;
end if;
end process test_req_delay;

button_delay_process: process(def_CLK_prescaled)
begin
if (rising_edge(def_CLK_prescaled)) then
if (test_start = '1') and (button_count < button_delay)
 ↪  and (test_request = '0') then
button_count <= button_count + 1;
elsif (button_count >= button_delay) and (test_request =
 ↪  '0') then
button_count <= (others => '0');
end if;
end if;
end process button_delay_process;

test_request_signal:
 ↪  process(def_CLK_prescaled_perturb,button_count,button_delay)
begin
```

```
if (rising_edge(def_CLK_prescaled_perturb)) and
 ↪  (button_count = button_delay) then
if  (k <= M - 1) and (i < (data_length - 1)) then
test_request <= '1';
elsif (i = (data_length - 1)) and (k = M - 1) then
test_request <= '0';
end if;
end if;
end process test_request_signal;

duty_perturb: process(def_CLK_prescaled_perturb)
begin
if (rising_edge(def_CLK_prescaled_perturb)) then
case def_sw(15 downto 14) is -- 00 white noise, 11 red
 ↪  noise
when "00" =>  random_integer_array :=
 ↪  to_integer(signed(wn_data));
when "01" =>  random_integer_array :=
 ↪  to_integer(signed(bn_data));
when "10" =>  random_integer_array :=
 ↪  to_integer(signed(pn_data));
when "11" =>  random_integer_array :=
 ↪  to_integer(signed(rn_data));
when others => random_integer_array :=
 ↪  to_integer(signed(wn_data));
end case;
if (test_request = '1') then
random_temp <= random_integer_array;
read_address <= std_logic_vector(to_unsigned(i,16));
def_debug2 <= '1';
elsif (test_request = '0') then
read_address <= (others => '0');
random_temp <= 0;
def_debug2 <= '0';
end if;
end if;
end process duty_perturb;

i_count: process(def_CLK_prescaled_perturb)
begin
if (rising_edge(def_CLK_prescaled_perturb)) then
if (test_request = '1') and (i < (data_length - 1)) then
i := i + 1;
elsif (i = (data_length - 1) ) then
i := 0;
end if;
end if;
end process i_count;
```

```
k_count: process(def_CLK_prescaled_perturb)
begin
if (falling_edge(def_CLK_prescaled_perturb)) then
if (k < (M - 1)) and (test_request = '1') and (i =
 ↪  (data_length - 1) ) then
k := k + 1;
elsif (k = (M - 1)) and (i = (data_length - 1) ) then
k := 0;
elsif (test_request = '0') then
k := 0;
end if;
end if;
end process k_count;

update_stop: process(def_CLK100MHZ)
begin
if (rising_edge(def_CLK100MHZ)) then
s_stop_temp <= (to_integer(unsigned(def_perturb_scale(5
 ↪  downto 0)))*random_temp*(to_integer(s_pre)) +
 ↪  s_duty_ss*(to_integer(s_pre)))/1000;
def_stop <= to_unsigned(s_stop_temp,27);
if (random_temp /= 0) then
def_debug <= '1'; --BURADA
elsif (random_temp = 0) then
def_debug <= '0'; --BURADA
end if;
end if;
end process update_stop;

update_prescale_rate:
 ↪  process(def_CLK_prescaled_perturb,test_request)
begin
if (rising_edge(def_CLK_prescaled_perturb)) and
 ↪  (test_request = '0') then
if (to_integer(def_sw(6 downto 4)) > 0) then
s_pre <= to_unsigned(1000*(to_integer(def_sw(6 downto
 ↪  4))),27);
end if;
if (to_integer(def_sw(6 downto 4)) > 0) and
 ↪  (to_integer(def_sw(3 downto 0)) > 0) then
s_pre_perturb <= to_unsigned(1000*(to_integer(def_sw(6
 ↪  downto 4)))*to_integer(def_sw(3 downto 0)),27);
end if;
end if;
end process update_prescale_rate;

end davranissal;
```

APPENDIX A.3: Prescaler Subprogram for Dividing the Clock

```
library IEEE;
use IEEE.STD_LOGIC_1164.ALL;
use IEEE.NUMERIC_STD.ALL;

entity prescaler is
port(
prscl_CLK100MHZ: in std_logic;
prscl_prescale_rate: in unsigned (26 downto 0);
prscl_CLK_prescaled: inout std_logic :='1'
);
end prescaler;

architecture davranissal of prescaler is

signal s_prscl_prescale_rate: unsigned (26 downto 0) := "000000000000000000000000001";
shared variable prscl_count: unsigned (26 downto 0) :="000000000000000000000000000";

begin

prescaler_proc: process(prscl_CLK100MHZ)
begin
if (rising_edge(prscl_CLK100MHZ)) then
prscl_count := prscl_count + 1;
if (prscl_count >= s_prscl_prescale_rate / "10") then
prscl_CLK_prescaled <= not prscl_CLK_prescaled;
prscl_count := "000000000000000000000000000";
end if;
end if;
end process prescaler_proc;

end davranissal;
```

APPENDIX A.4: Counter Subprogram

```
library IEEE;
use IEEE.STD_LOGIC_1164.ALL;
use ieee.numeric_std.all;

entity counter is
generic (cntr_type: in unsigned (1 downto 0));
port(
enable: in std_logic :='0';
cntr_CLK: in std_logic :='0';
cntr_CLK_prescaled: in std_logic :='0';
cntr_stop: in unsigned (26 downto 0);
cntr_type_out: out unsigned (1 downto 0);
cntr_count: inout unsigned (26 downto 0)
 ↪  :="000000000000000000000000001"
);
end counter;

architecture davranissal of counter is

shared variable cntr_main_count: unsigned (26 downto 0)
 ↪  :="000000000000000000000000000";
signal reset: std_logic :='0';

begin

counter: process(cntr_CLK,enable)
begin
if (enable = '1') then
if (rising_edge(cntr_CLK)) then
if (cntr_main_count < cntr_stop ) then
cntr_main_count := cntr_main_count + 1;
if (cntr_main_count >= cntr_stop ) then
cntr_main_count := "000000000000000000000000000";
end if;
end if;
end if;
end if;

case cntr_type is
when "00" =>  cntr_count <= cntr_main_count; -- trailing
 ↪  edge modulator
when "01" =>  cntr_count <= cntr_stop - cntr_main_count;
 ↪  -- falling edge modulator
when "10" => cntr_count <= cntr_main_count; -- triangle
 ↪  modulator
if (cntr_main_count <= cntr_stop / "10") then
cntr_count <= cntr_main_count + cntr_main_count;
```

```
elsif (cntr_main_count > cntr_stop / "10") then
cntr_count <= (cntr_stop - cntr_main_count)+(cntr_stop -
 ↪ cntr_main_count);
end if;
when others => cntr_count <= cntr_main_count; -- trailing
 ↪ edge modulator
end case;
end process;

counter_reset: process(cntr_CLK,cntr_CLK_prescaled)
begin
reset <= '0';
if (rising_edge(cntr_CLK_prescaled)) then
reset <= '1';
end if;
end process counter_reset;

cntr_type_out <= cntr_type;
end davranissal;
```

APPENDIX A.5: PWM Generator Subprogram

```
library IEEE;
use IEEE.STD_LOGIC_1164.ALL;
use IEEE.NUMERIC_STD.ALL;

entity pwm_module is
port(
pwm_CLK: in std_logic :='0';
pwm_start: in unsigned (26 downto 0);
pwm_stop: in unsigned (26 downto 0);
pwm_deadtime: in unsigned (26 downto 0);
pwm_count: in unsigned (26 downto 0);
pwm_pre: in unsigned (26 downto 0);
pwm_cntr_type: in unsigned (1 downto 0);
pwm_pwm_out: out std_logic;
pwm_pwm_out_comp: out std_logic
);
end pwm_module;

architecture davranis of pwm_module is
begin
pwm_module_proc: process(pwm_CLK)
begin
if (rising_edge(pwm_CLK)) then
if (pwm_cntr_type = "00") or (pwm_cntr_type = "01") then
if (pwm_count >= pwm_start + pwm_deadtime) and (pwm_count
 ↪  <= pwm_stop - pwm_deadtime) then
pwm_pwm_out <= '1';
else
pwm_pwm_out <= '0';
end if;
elsif (pwm_cntr_type = "10") then
if (pwm_count >= pwm_start) and (pwm_count <= pwm_stop -
 ↪  pwm_deadtime) then
pwm_pwm_out <= '1';
else
pwm_pwm_out <= '0';
end if;
end if;
end if;
end process pwm_module_proc;

pwm_module_comp_proc: process(pwm_CLK)
begin
if (falling_edge(pwm_CLK)) then
if (pwm_cntr_type = "00") or (pwm_cntr_type = "01") then
if (pwm_count >= pwm_stop + pwm_deadtime) and (pwm_count
 ↪  <= pwm_pre - pwm_deadtime) then
```

```
pwm_pwm_out_comp <= '1';
else
pwm_pwm_out_comp <= '0';
end if;
elsif (pwm_cntr_type = "10") then
if (pwm_count >= pwm_stop + pwm_deadtime) and (pwm_count
 ↪  <= pwm_pre) then
pwm_pwm_out_comp <= '1';
else
pwm_pwm_out_comp <= '0';
end if;
end if;
end if;
end process pwm_module_comp_proc;
end davranis;
```

APPENDIX B.1

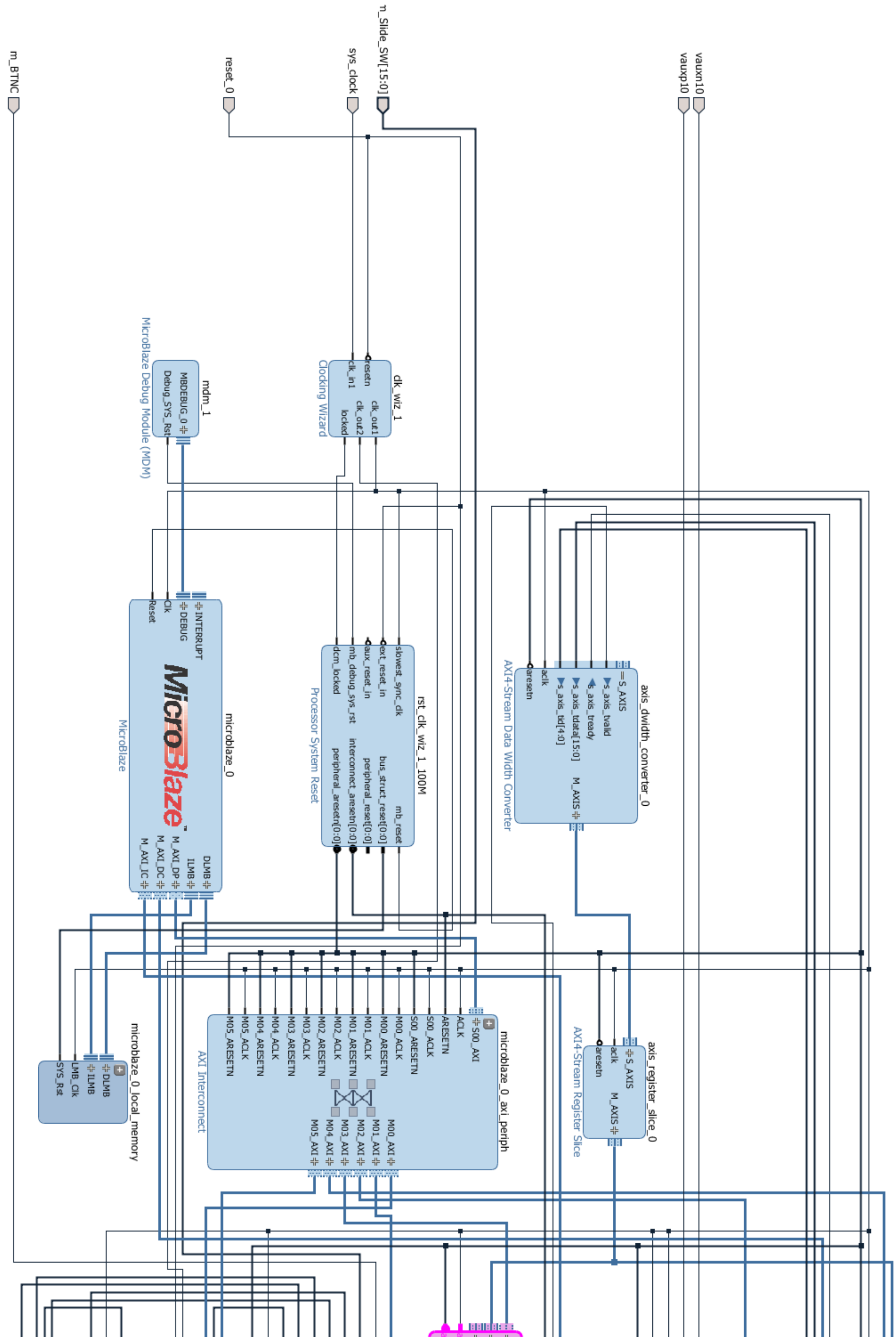

Figure B.1 : Complete overview of the implemented block design on the FPGA.

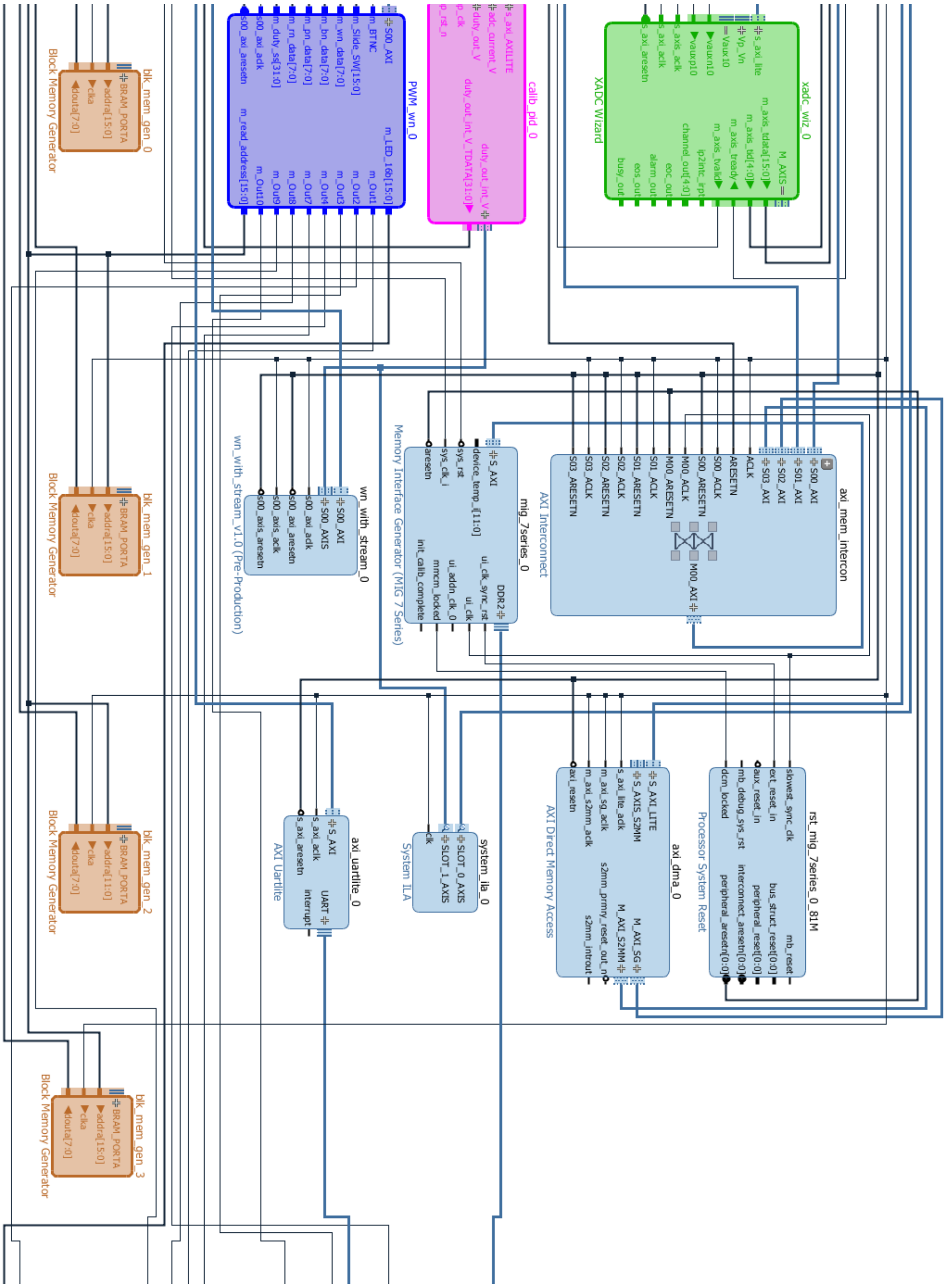

Figure B.2 : Complete overview of the implemented block design on the FPGA.

APPENDIX C.1: Matlab Script for Data Acquisition From NI cDAQ

```
clc;
clear;

s = daq.createSession('ni');
addAnalogInputChannel(s,'cDAQ1Mod1', 0, 'Voltage'); %w1
 ↪  -> perturbated duty cycle info
addAnalogInputChannel(s,'cDAQ1Mod1', 1, 'Voltage'); %w2
 ↪  -> current info
addAnalogInputChannel(s,'cDAQ1Mod1', 2, 'Voltage'); %w3
 ↪  -> test start stop signal
addAnalogInputChannel(s,'cDAQ1Mod1', 3, 'Voltage'); %w4
 ↪  -> voltage info
s.Rate = 500000;
s.DurationInSeconds = 10;
s

[data,time] = s.startForeground;
figure
plot(time,data);
xlabel('Time (secs)');
ylabel('Voltage')

w1 = transpose(data(:,1));
w2 = transpose(data(:,2));
w3 = transpose(data(:,3));
w4 = transpose(data(:,4));
fsampling = s.Rate;

enable = 0
if enable > 0
lh = addlistener(s,'DataAvailable', @(src,event)
 ↪  plot(event.TimeStamps, event.Data));
s.startBackground();
s.wait()
delete(lh)
s.IsNotifyWhenDataAvailableExceedsAuto = true;
lh = addlistener(s,'DataAvailable', @stopWhenExceedOneV);
type('stopWhenExceedOneV.m')
s.IsContinuous = true;
s.startBackground()
while s.IsRunning
pause(0.5)
fprintf('While loop: Scans acquired = %d\n',
 ↪  s.ScansAcquired)
end
fprintf('Acquisition has terminated with %d scans
 ↪  acquired\n', s.ScansAcquired);
```

```
delete(lh)
displayEndOfDemoMessage(mfilename)
end
```

APPENDIX C.2: Matlab Script for Preprocessing the Experimental Data

```
d_sample = 0;
d_sample_factor = 1; %do not change
if d_sample > 0
d_sample_factor = 10;
w10 = w1; w20 = w2; w30 = w3; w40 = w4;
w1 = downsample(w1,d_sample_factor);
w2 = downsample(w2,d_sample_factor);
w3 = downsample(w3,d_sample_factor);
w4 = downsample(w4,d_sample_factor);
end

size_data=length(w1);
n = 1:1:size_data;

figure
plot(n,w1,'y',n,w2,'b',n,w3,'m',n,w4,'g');
xlabel('Samples');
ylabel('Voltages');

start_point =
 ↪ ceil(cursor_info1.DataIndex/d_sample_factor);
finish_point =
 ↪ ceil(cursor_info2.DataIndex/d_sample_factor);

w1_test = w1(:,start_point:1:finish_point); legnth1 =
 ↪ length(w1_test);
w1_test(legnth1+1:2*legnth1) = 0;
w2_test = w2(:,start_point:1:2*finish_point-start_point);
w3_test = w3(:,start_point:1:2*finish_point-start_point);
w4_test = w4(:,start_point:1:2*finish_point-start_point);

window_size = 100;
w2_movavg0 = tsmovavg(transpose(w2),'s',window_size,1);
w2_movavg1 = tsmovavg(transpose(w2),'s',window_size/2,1);
 ↪ w2_movavg0 = w2_movavg0 - (w2_movavg0-w2_movavg1);
w2_movavg =
 ↪ w2_movavg0(start_point:1:2*finish_point-start_point,:);
w4_movavg0 = tsmovavg(transpose(w4),'s',window_size,1);
w4_movavg1 = tsmovavg(transpose(w4),'s',window_size/2,1);
 ↪ w4_movavg0 = w4_movavg0 - (w4_movavg0-w4_movavg1);
w4_movavg =
 ↪ w4_movavg0(start_point:1:2*finish_point-start_point,:);
vmean_mov =
 ↪ linspace(w4(start_point),w4(finish_point),(finish_point
 ↪ - start_point +1));
```

```
imean_mov =
 ↪  linspace(w2(start_point),w2(finish_point),(finish_point
 ↪  - start_point +1));

size_data = length(w1_test);
n_test = 1:1:size_data;
n_test_actual = 1:1:(finish_point - start_point);

d1 = dutycycle(w1_test(:,1:(finish_point-start_point)),
        n_test_actual,'Polarity','positive');
d1(length(d1)+1:2*length(d1)) = 0;
sized1 = length(d1);
d2 = 0.5*(ones(1,sized1)); %!!!
d1_perturb = d1 - ones(1,sized1)*mean(d2);
length(d1_perturb)

w1 = transpose(w1);
w2 = transpose(w2);
w3 = transpose(w3);
w4 = transpose(w4);
w1_test = transpose(w1_test);
w2_test = transpose(w2_test);
w3_test = transpose(w3_test);
w4_test = transpose(w4_test);
d1 = transpose(d1);
d1_perturb = transpose(d1_perturb);
length_d1 = length(d1_perturb)
vmean_mov = transpose(vmean_mov);
imean_mov = transpose(imean_mov);

show = 0
if show >= 1
        figure
        plot(n_test,w1_test,'y', n_test,w2_test,'b',
         ↪  n_test, w3_test, 'm', n_test, w4_test,'g');
        xlabel('Samples');
        ylabel('Voltages');
end

show = 0
if show >= 1
        figure
        subplot(2,1,1)
        plot(n_test, w4_test, 'b', n_test, w4_filtered,
         ↪  'r');
        xlabel('Samples');
        ylabel('Voltage');
        subplot(2,1,2)
```

```
        plot(n_test, w2_test, 'b', n_test, w2_filtered,
         ↪  'r');
        xlabel('Samples');
        ylabel('Current');
end

show = 0;
if show>=1
        figure
        subplot(2,1,1)
        plot(n_test, w2_test/4.7,'b', n_test,
         ↪  w2_movavg/4.7,'m', n_test, imean_mov/4.7,'r')
        subplot(2,1,2)
        plot(n_test,2*w4_test, 'b',n_test, 2*w4_movavg,
         ↪  'm', n_test, 2*vmean_mov, 'r')
        xlabel('Samples');
        ylabel('Voltages');
end
```

APPENDIX C.3: Matlab Script for Transfer Function Calculation

```
%SETTINGS
fperturb = 20e3; fsw = 20e3; fs = fsampling;

smoothing_window_size = 0;
freq_limit_number = 400;
method = 1;

alpha = 0;
fract_smooth = 1;
pad_factor = 0;

Rsense = 8;
Rparasitic = 0;

resample_required = 0;
size_data1 = length(d1_perturb);
period_count = size_data1;
size_data_original = length(w2_test);
size_data = size_data_original;


%%DUTY CYCLE PERTURBATION DEGERININ ZAMANA GORE YAYILMASI
total_sample = size_data;
data_per_period = size_data/period_count;
data_per_period = round(data_per_period);
i=1;
first = 1;
last = 1;

while i<period_count
        last = i*data_per_period;
        d1_perturb_time(first:last+1,1) = d1_perturb(i);
        first = last+1;
        i=i+1;
end

d1_perturb_time(first:size_data) = d1_perturb(i);
unew = d1_perturb_time;
if resample_required>=1;
        vnew = w2_test_resample;
        else
        vnew = w4_test;
        inew = w2_test;
end

%1st METHOD
```

```
if method == 1
        vmean = mean(w4(1:start_point));
         ↪ imean = mean(w2(1:start_point));
        vnew_p = vnew - ones(length(vnew),1)*vmean;
         ↪ inew_p = inew - ones(length(inew),1)*imean;
        inew_p = inew_p/Rsense;
elseif method == 2

%2nd METHOD
        vnew_p = vnew - w4_movavg;
        inew_p = inew - w2_movavg; inew_p =
         ↪ inew_p/Rsense;

elseif method == 3
        vnew_p = vnew - vmean_mov;
        inew_p = inew - imean_mov; inew_p =
         ↪ inew_p/Rsense;
elseif method == 4
        vnew_p = w4_filtered;                    %
         ↪ w4_filtered; %vnew - w4_filtered;
        inew_p = w2_filtered/Rsense;             %
         ↪ w2_filtered/Rsense; %(vnew -
         ↪ w2_filtered)/Rsense;
end;

Ruu = xcorr(unew,unew,total_sample);
Ruv = xcorr(unew,vnew_p,total_sample);
Rui = xcorr(unew,inew_p,total_sample);

win = gausswin(2*total_sample+1,alpha);
pad_size = round(pad_factor*length(Ruv));
Ruv_p = padarray(Ruv.*win,[pad_size 0],0,'both');
Rui_p = padarray(Rui.*win,[pad_size 0],0,'both');
Ruu_p = padarray(Ruu.*win,[pad_size 0],0,'both');

vd = fft(Ruv_p); vd = vd(1:(length(vd)+1)/2);
id = fft(Rui_p); id = id(1:(length(id)+1)/2);
uu = fft(Ruu_p); uu = uu(1:(length(uu)+1)/2);


clearvars f m p mag_tf phase_tf Q Z m_fract p_fract Gzoh
 ↪  Gzoh2;
f = (fs/1)*linspace(0,1,length(vnew_p));
w_rad = f*2*pi;
Z = (fft(vnew_p)./fft(inew_p));

clearvars f;
f = (fs/1)*linspace(0,1,length(vnew_p));
```

```
Z = Z - Rparasitic;

m = abs(Z); p = (angle(Z));
imp_real = real(Z);
imp_imag = imag(Z);


if (fract_smooth >= 1) && (smoothing_window_size <= 0)
        fract_dec_smooth_old();
end

test_data = Exp2;
k = length(test_data);
i = 1;
while i<=k
        f_iet = test_data(3,:);
        eq_model = test_data(4,i);
        if  eq_model == 1
                Ls = test_data(1,i);
                Rs = test_data(2,i);
                measurement = tf([Ls Rs],[1]);
                w = 2*pi*test_data(3,i);
                [mag,phase] = bode(measurement,w);
                output(1,i) = mag; %magnitude data
                output(2,i) = phase; %phase data
                output(3,i) = test_data(3,i); %freq
                elseif eq_model == 2
                Cs = test_data(1,i);
                Rs = test_data(2,i);
                measurement = tf([Cs*Rs 1],[Cs 0]);
                w = 2*pi*test_data(3,i);
                [mag,phase] = bode(measurement,w);
                output(1,i) = mag; %magnitude data
                output(2,i) = phase; %phase data
                output(3,i) = test_data(3,i); %freq
        end;
        i=i+1;
end;

%Analytical Calculation
enable = 1;
if enable > 0
        Z_analytic = tf([C*L*R1 (L+C*R1*R2)
         ↪ (R1+R2)],[C*R1 1]);
        w = 2*pi*f;
        [mag,phase] = bode(Z_analytic,w);
        sizemag=size(mag);
        i=1;
```

```
        clearvars mag_tf phase_tf;
        while i<=sizemag(3)
                mag_tf(i) = mag(1,1,i);
                phase_tf(i) = phase(1,1,i);
                i = i+1;
        end
end;

figure
subplot(2,1,1)
semilogx(f,mag2db(m), 'b', f_iet, mag2db(output(1,:)),
 ↪  'r.', f, mag2db(mag_tf), 'k')
grid on
set(gca, 'XColor', [0.5 0.5 0.5])
set(gca, 'YColor', [0.5 0.5 0.5])
ylabel('Magnitude [Ohms]')
subplot(2,1,2)
semilogx(f, p*180/pi, 'b', f, (phase_tf), 'k', f_iet,
 ↪  (output(2,:)), 'r.')
ylabel('Phase [deg]')
xlabel('Hz');
grid on
set(gca, 'XColor', [0.5 0.5 0.5])
set(gca, 'YColor', [0.5 0.5 0.5])

show = 1;
if show > 0
        x=1:1:length(Ruu);
        figure
        subplot(3,1,1)
        plot(x,Ruu);
        title('Ruu')
        grid on

        subplot(3,1,2)
        plot(x,Ruv);
        title('Ruv')
        grid on

        subplot(3,1,3)
        plot(x,Rui);
        title('Rui')
        grid on
end;

%REAL IMAGINAR AXIS PLOT(NYQUIST)
show = 1;
if show > 0
```

```
        figure
        plot(Z_bat_exp_real, Z_bat_exp_imag, 'r',
         ↪  imp_real(2:freq_limit_number),
         ↪  imp_imag(2:freq_limit_number), 'b')
        set(gca,'Ydir','reverse')
        ylabel('Z_{imag} [Ohm]')
        xlabel('Z_{real} [Ohm]')
        grid on

        figure
        set(gca,'Ydir','reverse')
        plot3(imp_real(2:freq_limit_number),
         ↪  imp_imag(2:freq_limit_number),
         ↪  f(2:freq_limit_number), 'b')
        grid on
end
```

APPENDIX C.4: Matlab Script *fract_dec_smooth_old.m* for Postprocessing the Transfer Function

```
clearvars window_size n_dec fract_index m_fract p_fract
 ↪  m_mov_ave p_mov_ave;
delta_f = f(2,1); %checking resolution
start_decade = floor(log10(delta_f));
stop_decade = floor(log10(fs/2));
n_dec = start_decade:1:stop_decade;

k = 1;
while k <= length(n_dec)
        fract_index(k) = ceil(10^n_dec(k)/delta_f);
        k = k+1;
end

i = 1;
while i <= length(n_dec)
        if i == length(n_dec)
                End = length(m);
        else
                End = fract_index(i+1);
        end
        data_per_dec(i) = End - fract_index(i);
        window_size(i) = ceil(data_per_dec(i)/100);
        i = i +1;
end

med_filt_size = (n_dec + 1).^2;
j = 1;
while j <= length(n_dec)
        if j == length(n_dec);
                fract_stop = length(m);
                else
                fract_stop = fract_index(j+1);
        end
        Z_mov_ave(:,j) =
         ↪  tsmovavg(Z2,'s',window_size(j),1);
        m = abs(Z_mov_ave); p = unwrap(angle(Z_mov_ave));
        m_mov_ave = medfilt1(m,med_filt_size(j));
        p_mov_ave = medfilt1(p,med_filt_size(j));
        m_fract(fract_index(j):fract_stop,1) =
         ↪  m_mov_ave(fract_index(j):fract_stop,j);
        p_fract(fract_index(j):fract_stop,1) =
         ↪  p_mov_ave(fract_index(j):fract_stop,j);
        j = j+1;
end
```

```
m = (m_fract); p = (p_fract);
```

CURRICULUM VITAE

Name Surname: Taha Nurettin GÜCİN

EDUCATION:

- **M.Sc.:** 2013, Istanbul Technical University, Energy Institute, Energy Science and Technology Master Program
- **B.Sc.:** 2010, Istanbul Technical University, Faculty of Electrical and Electronics Engineering, Electrical Engineering Department

PROFESSIONAL EXPERIENCE AND REWARDS:

- **Power Supply Engineer** 2017 - 2019
  Elettra-Sincrotrone Trieste, Trieste - ITALY
  Power Supplies Laboratory
- **Research and Teaching Assistant** 2010 - 2017
  Energy Systems Engineering Department, Yalova - TURKEY
  University of Yalova
- **Research and Teaching Assistant** 2014 - 2015
  Electrical Engineering Department
  Istanbul Technical University, Istanbul - TURKEY

PUBLICATIONS, PRESENTATIONS AND PATENTS ON THE THESIS:

- **Gücin, T. N.** and Ovacik, L., 2020. Online Impedance Measurement of Batteries Using the Cross-Correlation Technique, *IEEE Transactions on Power Electronics*, 35(4), 4365-4375.
- **Gücin, T. N.** and Ovacik, L., 2016. An impedance analyzer application using cross-correlation method. *2016 IEEE International Conference on Renewable Energy Research and Applications (ICRERA)*, November 20 - 23, 2016, Birmingham, United Kingdom.